TECHNISCHE UNIVERSITÄT MÜNCHEN

Lehrstuhl für Physik funktionaler Schichtsysteme, E10

Magnetic investigations on correlated electrons in a pseudo-spin-system and ferromagnetic / nanomechanical hybrid systems

Tjark Windisch

Vollständiger Abdruck der von der Fakultät für Physik der Technischen Universität München zur Erlangung des akademischen Grades eines Doktors rer. nat.
genehmigten Dissertation.

Vorsitzender: Univ.-Prof. Dr. R. Metzler
Prüfer der Dissertation:
1. Univ.-Prof. Dr. D. Grundler
2. Univ.-Prof. Dr. A. Holleitner

Die Dissertation wurde am 25.11.2010 bei der Technischen Universität München eingereicht und durch die Fakultät für Physik am 14.12.2010 angenommen.

Abstract

In the course of this work a fiber optical cantilever magnetometer with a 4 axis piezo based positioning system was designed and set up. The positioning system is based on the slip-stick principal and included movement in xyz and angle α direction. We performed simulations to understand the reflectivity evolution while scanning the sample with respect to the glass fiber of our detection setup.

To measure the magnetization of AlAs quantum wells we used a capacitive read out cantilever magnetometer. These AlAs quantum wells exhibit a twofold valley degeneracy. We performed intensive studies on the angular dependence of the magnetization with respect to the external magnetic field which revealed a strong electron-electron interaction and a lifting of the valley degeneracy even for angles of $\alpha \to 0$ and therefore an intrinsic crossing of the energy levels. In addition we performed temperature dependent studies which revealed strongly enhanced energy gaps and a temperature dependence that does not even qualitatively match to the expectations including commonly assumed many body effects.

In the second part of this work we investigated on the mechanical and magnetic properties of nanomechanical bridges. These bridges with a width of 120 nm a length of 2 μm and a thickness of roughly 150 nm were prepared by focused ion beam etching into the inner conductor of a coplanar wave guide. We performed GHz spectroscopy measurements in the time and frequency regime. We were able to measure the ultra high resonance frequency of the nanobridge in the order of 0.5 GHz. The excitation power dependent measurements indicate a mechanical resonance oscillation. In contrast to our expectations the magnetic field dependent measurements did not reveal the mechanism by which the

mechanical oscillation is excited but we were able to exclude commonly assumed mechanisms.

Contents

List of Figures

Chapter 1

Introduction

The mechanical, electronic, and magnetic properties of multilayered materials has long been a field of research. Especially the interactions between these areas provided important developments. Recently research is focussed on interaction on a nanoscopic scale. In this case not only applications are the goal of the researchers but also a fundamental understanding of these interactions is reachable.

In this work measurements on two different types of samples are presented that present different sides of a combination of nanomechanics and magnetism. Firstly, we present a mechanical system that is used to detect the magnetic properties of an AlAs quantum well. This micromechanical cantilever magnetometer was improved by designing a piezo based nanopositioning system for enhanced sensitivity. Secondly, we present measurements to determine the mechanical and magnetic properties of nanomechanical bridges in the inner conductor of a coplanar waveguide. Especially the coupling between mechanical motion and magnetic excitation is investigated. In the following we motivate both parts of this work separately.

AlAs quantum wells

The electronic and magnetic properties of semiconductor heterostructure are an intriguing field of physics. Starting with the discovery of the quantum Hall effect [vK80] and the fractional quantum Hall effect [Tsu82] in two-dimensional electron systems the ground state energy level sequence of the electrons has always been a main interest of research. While the quantum Hall effect was first observed in 2DES in silicon based MOSFETs [1] the fractional quantum Hall effect was discovered in high mobility samples on AlGaAs and GaAs compounds. Following these discoveries most experiments use low-temperature magneto transport measurements. Unfortunately, magneto-transport measurements share an important flaw with optical measurements methods like FIR or Raman spectroscopy. All of these measurement techniques excite the electrons. Thus, an excited state is measured and not the undisturbed ground state. A direct relation of the electronic ground state is given for thermodynamic quantities. Investigations include magnetocapacitance, specific heat, compressibility, and magnetization.

In this work we use the magnetization to gain information on the electronic structure of AlAs quantum wells. In recent experiments AlAs quantum well showed a variety of novel and intriguing physics [Vak04, Sha06, Shk05]. Due to the additional valley degree of freedom this system is a valid candidate for future applications in information technology. To manipulate and store information on the basis of pseudo spins reliable it is important to fully understand the electronic ground state. Due to the highly complex nature of the electronic ground state of AlAs quantum wells intensive simulations has to be performed to extract the electronic ground state. This is not within the scope of this thesis.

Magnetomechanical Transducer

In addition to the afore mentioned field of semiconductor electronic states the field of nanotransducer receives rising interest. These devices are designed to transform mechanical, optical, magnetic and chemical

[1] Metal Oxide Semiconductor Field Effect Transistor

signals into input and output ports of information processing units. In the information technology transducers are used to manipulate and store information. Traditionally this is done by manipulation of magnetic materials. Especially the dynamics of the magnetization of nanoscopic ferromagnetic materials are of great interest from a fundamental and an application point of view. In this case the magnetic information is transduced into electrical signals.

To gain fundamental understandings of the transducing of signals nanomechanical bridges covered by ferromagnetic material are used. These systems provide the opportunity that two instead of one transducing effect takes place at once. By choosing this system we are able to investigate the interactions of both systems, mechanical and ferromagnetic, to a wider extent.

This work is structured as follows: In chap. 2 we present the fundamental physics of electrons in AlAs quantum wells with a focus on the magnetic properties of the electrons in external magnetic fields. We show the basic concepts of spin dynamics in ferromagnetic thin films and present some characteristics of mechanical oscillations. In chap. 3 we discuss the setup designed in the course of this work in detail. Additionally we show a capacitive readout technique for cantilever magnetometry. In the second part of this chapter we present the setup to perform GHz spectroscopy both in the frequency and in the time domain. In chap. 4 the relevant preparation processes are discussed. The measurements are divided into two chapters. In chap. 5 measurements in AlAs quantum wells are presented while the measurements on nanomechanical bridges are shown in chap. 6. The work closes with an outlook on possibly subsequent experiments in chap. 7.

Chapter 2

Theoretical basics

In this chapter the fundamental theoretical concepts necessary to interpret the experimental results obtained in this work will be presented. This chapter is divided into two main sections. In sec. 2.1 we start with the fundamental properties of quasi two-dimensional electron systems (2DES) in external magnetic fields. The thermodynamic properties of 2DES is discussed in order to explain the magnetization measurements in semiconductor heterostructures. In addition to the well known de Haas-van Alphen (dHvA) effect in perpendicular magnetic fields the influence of an in-plane magnetic field component is treated theoretically. We recall the Lifshitz-Kosevich approach to the temperature dependence of the dHvA oscillation amplitudes and introduce a semi-qualitative picture to account for many-body effects.

In order to discuss the experimental results on nanomechanical bridges presented in chap. 6 the basic concept of spin-dynamics are introduced in sec. 2.2. In addition possible coupling mechanisms of microwaves to nanomechanical bridges are discussed.

2.1 2DES in perpendicular magnetic fields

In this section we present the fundamental physics that are important to understand the experimental data we obtained in the course of this work. We start with the basic concepts of 2DESs in a perpendicular magnetic field. The basic model of Landau levels in a perpendicular magnetic field will be expanded to the case of an additional magnetic field component parallel to the 2DES.

Noninteracting electron systems in an external magnetic field are described by the Hamiltonian

$$\hat{H} = \frac{\left(\hat{p} + e\vec{A}\right)^2}{2m^*} + V(\vec{r}), \tag{2.1}$$

with the momentum operator $\hat{p} = -i\hbar\nabla_{\vec{r}}$, the vector potential $\vec{A}$, and the external potential $V(\vec{r})$. We assume $V(\vec{r}) = 0$ in the following, i.e., we neglect the influence of the sample boundaries of a real system. The external magnetic field is determined by the vector potential via:

$$\nabla \cdot \vec{A} = 0, \quad \nabla \times \vec{A} = \vec{B}. \tag{2.2}$$

We choose the magnetic field $\vec{B} = B\vec{e_z}$ to point along the z-axis and we get the vector potential in the Landau gauge to be $\vec{A} = xB_z\vec{e_y}$. As we constrict to two-dimensional systems the Schrödinger equation becomes

$$\left[\frac{\partial^2}{\partial x^2} + \left(\frac{\partial}{\partial y} + \frac{ieB_z}{\hbar}x\right)^2 + \frac{2m^*}{\hbar}E\right]\Phi(x,y) = 0. \tag{2.3}$$

A solution is

$$\Phi(x,y) = \phi(x)e^{ik_y y}. \tag{2.4}$$

Inserting eq. (2.4) in the Schrödinger eq. (2.3) we get

$$\left[-\frac{\hbar^2}{2m^*}\frac{\partial^2}{\partial x^2} + \frac{m^*\omega_c^2}{2}(x - x_0)^2\right]\phi(x) = E_{xy}\phi(x) \tag{2.5}$$

with the cyclotron frequency

$$\omega_c = \frac{eB}{m^*}. \tag{2.6}$$

In this case $x_0 = -\hbar k_y/m^*\omega_c$ is the center coordinate of a cylclotron orbit. The eigenfunctions are

$$\phi_j(x) = (2^j j!\sqrt{\pi}x_0)^{-1/2} \exp\left[-\frac{1}{2}\left(\frac{x}{x_0}\right)^2\right] H_j(x/x_0), \tag{2.7}$$

H_j are the Hermite-polynomials. The energy eigenvalues are the eigenvalues of the harmonic oscillator with frequency ω_c:

$$E_j = E_{0,z} + \left(j + \frac{1}{2}\right)\hbar\omega_c. \tag{2.8}$$

In both cases it is $j = 0, 1, 2, \ldots$. We incorporated here the energy of the lowest subband in out-of-plane direction $E_{0,z}$ for consistency. In real 2DES the confinement potential in z-direction leads to multiple subbands. We assume for now only the lowest subband is occupied and no influence of higher subbands are taken into account. This is correct for infinite thin 2DES. The influence in finite thickness is discussed below in subsection 2.1.1.

The energy levels are called Landau levels and are shown in fig. 2.1(a). The magnetic field dispersion is high lighted in fig. 2.1(b)

The energy eigenvalues are independent of k_y and therefore degenerate. The degeneracy of a Landau level per unit area is

$$N_L = \frac{eB}{h} \cdot g_s \cdot g_v. \tag{2.9}$$

In the case of spin degeneracy it is $g_s = 2$ and g_v is a degeneracy factor counting the number of occupied conduction band valleys. It is $g_v = 2$ for AlAs quantum wells investigated in this work and $g_v = 1$ for GaAs.

The filling factor ν is defined as the ratio between carrier density n_s and the level degeneracy N_L

$$\nu = \frac{n_s}{eB/h} \tag{2.10}$$

The condition of an integer filling factor ν is fulfilled when all Landau levels are either empty or fully filled.

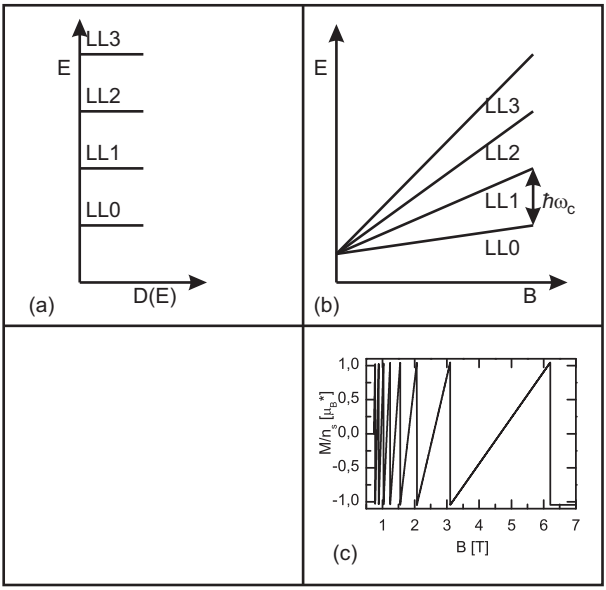

Figure 2.1: (a) Density of states (DOS) versus level energy for a 2DES in a perpendicular magnetic field. The δ-shaped Landau levels are shown. (b) The evolution of the Landau levels with the magnetic field B. The distance between two subsequent Landau levels is given by $\hbar\omega_c$. (c) Ideal magnetization of a 2DES with carrier density $n_s = 3 \times 10^{15}$ m^{-2}. The sawtooth like dHvA oscillations at integer filling factors can be seen.

Due to the Landau quantization the density of states (DOS) is a set of discrete levels

$$D(E) = N_L \sum_{j=0}^{\infty} \delta(E - E_j - E_{0,z}). \tag{2.11}$$

For the case of $B \to 0$ the DOS transforms smoothly to the constant value of a two dimensional electron system

$$D(E)_{B=0} = \frac{m^*}{\pi\hbar^2} \qquad \text{for } E \geq E_{z,0} \tag{2.12}$$

$$0 \qquad \text{for } E < E_{z,0}. \tag{2.13}$$

Magnetization

For low temperatures the Landau quantization leads to oscillations in thermodynamic quantities. In the case of the magnetization

$$M = -\frac{\partial F}{\partial B}|_{N,T} \tag{2.14}$$

this effect is called de Haas-van Alphen effect. In the limit of zero temperature eq. 2.14 simplifies to $M = -(\partial U/\partial B)_N$ because it is $F = U - TS$ (F is free energy, U is inner energy, T is temperature, N is the particle number, and S is the entropy).

The inner energy of the 2DES is obtained by summing up all states below the Fermi energy E_F:

$$U = \int_0^{E_F} E \cdot D(E) dE. \tag{2.15}$$

Inserting the expression for the DOS eq. (2.11) yields:

$$U = n_s E_{z,0} + \sum_{j=0}^{n-1} \left(j + \frac{1}{2}\right) \hbar\omega_c \cdot N_L + \left(n + \frac{1}{2}\right) \hbar\omega_c \cdot (n_s - nN_L)\,. \tag{2.16}$$

The first term reflects the lowest subband energy in z direction, the second term is the energy from all fully occupied energy levels. The

third term takes into account the partially filled in where the Fermi energy resides. For simplicity we assume from now on $E_{z,0} = 0$ unless otherwise noted. If we neglect the spin and valley splitting we can calculate the magnetization to:

$$M = -\mu_B^* \left[\left(n + \frac{1}{2} \right) n_s - N_L (n + n^2) \right] \tag{2.17}$$

with the effective Bohr magneton $\mu_B^* = eh/2m_e^* = 1.38 \cdot 10^{-22}$ J/T in GaAs. This is shown in fig. 2.1(c). At integer filling factors the magnetization has an infinitely sharp jump of $\Delta M = -2\mu_B^*$. These jumps like the filling factors are periodic in $1/B$ with a period of

$$\Delta \left(\frac{1}{B} \right) = \frac{2e}{h n_s}. \tag{2.18}$$

The thermodynamic quantities are directly related to each other via Maxwell's relations. For M and the chemical potential χ this is

$$\frac{\partial M}{\partial \chi}|_B = \frac{\partial N}{\partial B}|_\chi. \tag{2.19}$$

In the case of a 2DES with δ- or boxed-shaped Landau levels N depends linearly on B, since $N_L = g_s g_v eB/h$. Therewith the eq. (2.19) can be simplified [Wie97] to

$$\frac{\Delta M}{N} = \frac{\Delta \chi}{B}. \tag{2.20}$$

In a system where the broadening is small and the temperature is low compared to the energy gap between the levels the jump in the chemical potential is from one energy level to the next one. In this case the jump in the chemical potential $\Delta\chi$ equals the distance of the energy levels ΔE. Therefore we use the equation

$$\Delta E = \frac{\Delta M}{N} B \tag{2.21}$$

to calculate the energy gaps from the magnetization jump.

Spin and Valley Splitting

In general the spin degeneracy can be lifted due to the Zeeman splitting. Taking the Zeeman term into account the energy spectrum is

$$E_{j,s} = \left(j + \frac{1}{2}\right)\hbar\omega_c + sg_s\mu_B B, \tag{2.22}$$

with $\mu_B) = eh/2m_e$ is the Bohr magneton and $s = \pm 1/2$ is the spin quantum number. In AlAs the Lande factor g has the band-structure vallue $g_s = 2$. However, it is known that the spin splitting can be enhanced with respect to its band-structure value under certain circumstances. We will discuss this in more detail in sec. 2.1.

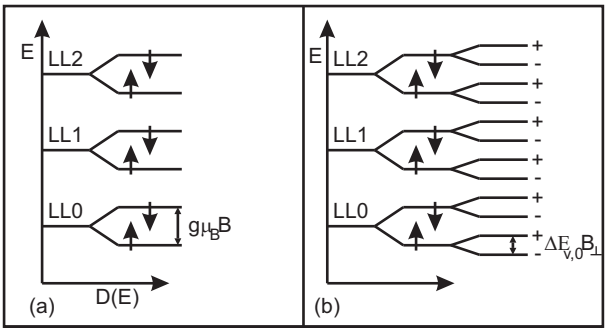

Figure 2.2: (a) The spin degeneracy of the Landau levels is lifted. The energy levels are still degenerate with respect to the valley quantum number. (b) Spin and valley degeneracy is lifted.

In the course of this work we investigate a AlAs quantum well system with a valley degeneracy factor of $g_v = 2$. The degeneracy is lifted in a external magnetic field. Therefore we theoretically treat systems where the valley degeneracy is lifted.

Starting from a single particle picture there is no reason for the valley degeneracy to be lifted. But experimental results showed a unexpected lifting of the valley degeneracy in different systems. We start

with a phenomenological approach to the valley splitting by identifying the valley index with an iso-spin quantum number v:

$$E_{j,s,v} = \left(j + \frac{1}{2}\right)\hbar\omega_c + sg_s\mu_B B + \frac{1}{2}vE_{v,0}B_\perp. \tag{2.23}$$

Here it is $v = \pm 1$ the iso-spin projection and the phenomenological valley splitting energy $\Delta E_{v,0}$. It was found that the valley splitting is also subject to enhancement by exchange interaction. Thus we take a closer look on the exchange interaction in 2DES in the next paragraph.

From single-particle to many-body picture

From many experiments it is known that the spin splitting can be enhanced with respect to its bandstructure value. The is attributed to exchange interaction [Jan69]. Electrons with the same spin are spatially more separated compared to those with different spin because of the Pauli principle. Electrons have lower potential energy if they are farther apart due to their Coulomb potential and are therefore energetically favored. Thus the energetic difference between spin-up and spin-down states is enhanced if the population of both levels is unbalanced.

Due to this effect it is necessary to take into account the actual polarization of levels in order to construct an energy level sequence. This is especially important if we compare the energy level sequence at different filling factors.

Calculations of the exchange interaction in the Hartree-Fock approximation have been performed by Ando and Uemura [And74]. Further investigations [Mac86, Man95] revealed an expression for the effective spin splitting

$$E_{N\downarrow} - E_{N\uparrow} = |g|\mu_B B + E_c \sum_j X_{N,j}(\nu_{j\uparrow} - \nu_{j\downarrow}) \tag{2.24}$$

where $\nu_{j\sigma}$ is the partial filling of the level $j\sigma$ and $E_c = \frac{e^2}{4\pi\epsilon\epsilon_0 l_B}$ is the Coulomb exchange interaction energy. The $X_{N,j}$ are coefficients from integrating matrix elements of the Fourier transform of the Coulomb potential. Because the spin occupation imbalance varies for different

filling factors, due to eq. (2.24) the spin splitting oscillates with respect to the filling factor or rather the external magnetic field B. At filling factors with high spin occupation imbalance the spin spitting is high. This is, e.g. the case for filling factor one. At other filling factors the spin occupation imbalance in zero, e.g. filling factor 4. This was firstly observed experimentally by Englert [Eng82].

We do not attempt to model the magnetization properties in a Hartree-Fock approximation. In this work a simplified model is used to incorporate the oscillations of the spin splitting. By neglecting the overlap terms of exchange between electrons in different Landau levels we get [Nic88]

$$E_{ex} = E_{ex,0} \left(N_{\uparrow} - N_{\downarrow} \right), \tag{2.25}$$

with the relative populations $N_{\uparrow}, N_{\downarrow}$ of spin states of the Nth Landau level. The spin splitting becomes

$$\Delta E_s = g\mu_B B + E_{ex,0} \left(N_{\uparrow} - N_{\downarrow} \right). \tag{2.26}$$

This is still a phenomenological approach to account for oscillating spin splitting. The polarization dependent part is often rewritten in the terms of an exchange enhanced Landé factor g^* that parameterizes the enhanced energy gap. The enhanced Landé factor strongly depends on the magnetic field. Because the polarization state depends on the filling factor the enhanced Landé factor depends only on the perpendicular magnetic field $g^*\mu_B B_{\perp} = g\mu_B B + E_{ex} B_{\perp}$, where $g - g^*$ only depends on $B_{\perp}$.

Although the exact origin of the splitting of the two occupied in-plane valleys in AlAs quantum wells is still unclear, the same process is expected to take effect as well [And82]. We therefore assume the valley splitting to be enhanced in the same manner as the spin splitting

$$\Delta E_v = E_{v,0} B_{\perp} + E_{ex,0,v} \left(N_{+} - N_{-} \right), \tag{2.27}$$

with the bare value of the valley splitting $E_{v,0}$ and the relative valley occupation $N_{+} - N_{-}$.

Similar to the exchange enhanced Landé factor it is possible to rewrite the last part to a magnetic field dependent splitting value $E^*_{v,0} B_{\perp} = E_{v,0} B_{\perp} + E_{ex,0,v} \left(N_{+} - N_{-} \right)$. with $E_{ex,0,v} \left(N_{+} - N_{-} \right)$ depends on $(B_{\perp})$.

2.1.1 In-plane magnetic fields

We study in this thesis 2DES in tilted magnetic fields with high tilt angles between the 2DES normal nd the magnetic field direction of up to $\alpha = 80°$. Thus it is important to understand the influence of strong in-plane magnetic field components on the energy spectrum.

If the magnetic field is applied perpendicular to the 2DES, then the electronic states condense into Landau levels on top of the 2DES subband states $E_{i,z}$. These Landau levels are highly degenerate as described in subsection. 2.1. In this case the electronic and magnetic quantization are not coupled [And82]. If the magnetic field is tilted with respect to the 2DES the electronic and magnetic quantization start to couple. While the cyclotron frequency $\omega_c = eB_\perp/m^*$ and the level degeneracy $N_L = eB_\perp/h$ depend only on the perpendicular field component $B_\perp = |B| \sin\alpha$, the electron eigenenergies become explicitly dependent on $B_\perp$ and $B_{||} = |B| \cos\alpha$.

To get an analytical solution for arbitrary angles we assume the confinement potential in growth direction to be parabolic [Ihm92]. Although this is known to be not the case for the samples used in the course of the thesis, our main interest is to get a qualitative picture of the coupling of the two lowest subbands. The assumption allows for analytical solutions for arbitrary tilt angles [Maa84, Mer87].

For convenience we define the xyz coordinate frame to be $\vec{e_z}||\vec{n}$ and $\vec{e_x} \perp \vec{n}$, where $\vec{n}$ denotes the surface normal of the 2DES. The tilted magnetic field $\vec{B} = (B_x, 0, B_z)$ is defined by the gauge $\vec{A} = (0, B_z x - B_x z, 0)$ and with a confinement in growth direction $V(z) = (m^*/2)\omega_e^2 z^2$ the Hamiltonian becomes [Zha97]

$$\hat{H} = \frac{\hat{p_x}^2}{2m^*} + \frac{\left(\hat{p_y} - eB_z x + eB_x z\right)^2}{2m^*} + \frac{\hat{p_z}^2}{2m^*} + \frac{1}{2} m^* \omega_e^2 z^2. \tag{2.28}$$

This can be simplified because $\left[\hat{H}, \hat{p_y}\right] = 0$. We get

$$\hat{H} = \frac{\hat{p_x}^2}{2m^*} + \frac{\hbar^2 k_y^2}{2m^*} + \frac{\hat{p_z}^2}{2m^*} + \frac{m^*\omega_e^2}{2} z^2 + \frac{m^*\omega_z^2}{2} x^2 + \frac{m^*\omega_x^2}{2} z^2 - m\omega_x\omega_z xz - \hbar k_y \omega_z x + \hbar k_y \omega_x z, \tag{2.29}$$

with $\omega_z = eB_z/m^*$ and $\omega_x = eB_x/m^*$. This can be simplified further by a rotation of the coordinates x and z. We substitute $x = X\cos\theta - Z\sin\theta$ and $z = X\sin\theta + Z\cos\theta$ to get

$$\hat{H} = \frac{\hat{p_X}^2}{2m^*} + \frac{m^*}{2}\left(\omega_Z^2 + \omega_e^2\sin^2\theta\right)(X - X_0)^2 +$$

$$\frac{\hat{p_Z}^2}{2m^*} + \frac{m^*}{2}\left(\omega_X^2 + \omega_e^2\cos^2\theta\right)(Z - Z_0)^2 \tag{2.30}$$

with $\omega_Z = \omega_z\cos\theta - \omega_x\sin\theta$ and $\omega_X = \omega_x\cos\theta + \omega_z\sin\theta$. The angle of rotation is given by

$$\tan 2\theta = \frac{\sin 2\alpha}{\cos 2\alpha - \omega_e^2\cos^2\alpha/\omega_z^2} \tag{2.31}$$

, and the guiding center coordinates are

$$X_0 = \frac{\hbar k_y}{m^*\omega_Z\left(1 + \frac{\omega_e^2}{\omega_Z^2}\sin^2\theta\right)} \tag{2.32}$$

and

$$Z_0 = \frac{\hbar k_y}{m^*\omega_Z\left(1 + \frac{\omega_e^2}{\omega_X^2}\cos^2\theta\right)}. \tag{2.33}$$

This corresponds to two separate harmonic oscillators with the eigenenergies

$$E_{i,j} = h\omega_1\left(i + \frac{1}{2}\right) + h\omega_2\left(j + \frac{1}{2}\right) \tag{2.34}$$

with $\omega_1 = \sqrt{\omega_Z^2 + \omega_e^2\sin^2\theta}$ and $\omega_2 = \sqrt{\omega_X^2 + \omega_e^2\sin^2\theta}$. The wave function is

$$|ijk_y\langle = e^{ik_y y}\phi_i(X - X_0)\phi_j(Z - Z_0). \tag{2.35}$$

Starting with these new eigenenergies we can calculate the perpendicular magnetization at $T = 0$ by partially differentiating the systems inner energy U with respect to $B_\perp$

$$M_\perp = -\frac{\partial U}{\partial B_\perp} \tag{2.36}$$

We get the total energy U by summing up all populated single particle states.

The main effect that originates from in-plane magnetic field is that the oscillation amplitudes exhibit a characteristic field dependence. Especially the oscillation amplitudes decreases as a function of high in-plane magnetic fields. This decrease is monotone with increasing external magnetic field.

2.1.2 Level broadening

In real 2DES the energy levels are not ideal δ-shaped but broadened. This broadening is due to disorder. Another important effect is due to finite temperature. Although this effect does not affect the actual broadening but the occupation probability of the energy levels we treat both by determining a specific reduction factor. Because both effects are treated by introducing a reduction factor for the oscillation amplitudes the temperature effect is often referred to as temperature dependent broadening.

broadening due to disorder

The broadening due to disorder is addressed by assuming a finite scattering time τ which results in broadened Landau levels following a Lorentz shape. Each δ-peak at energy E' is replaced by

$$g(E-E') = \frac{2}{\pi\Gamma}\frac{1}{1+\left(\frac{2(E-E')}{\Gamma}\right)} \tag{2.37}$$

where Γ is the full width at half maximum of the Lorentz peak. The parameter Γ is called intrinsic broadening in the course of this thesis.

Such a broadening results in a specific magnetic field dependence of the oscillation amplitudes even in perfectly perpendicular magnetic field

$$\Delta M(B) = aR_D(B)e^{-\frac{b}{B}} \tag{2.38}$$

with the fitting parameter a and b as well as the reduction factor

$$R_T(B) = e^{\frac{\pi\Gamma}{2\mu^*_B B}}. \tag{2.39}$$

In the limit $T \to 0$ and $B_{||} \to 0$ it is possible the extract the broadening parameter Γ from the fitting parameters

$$\Delta M(B_\perp \to \infty) = a, \tag{2.40}$$

$$\Gamma = b\frac{2\mu^*_B}{\pi}. \tag{2.41}$$

The reduction factor R_T is only valid for the first Fourier component of the dHvA oscillations.

Temperature dependance

The Fermi distribution describes the probability of a electronic state at energy E to be occupied

$$f(E, E_F, T) = \left(1 + \exp\left[\frac{E - E_F}{k_B T}\right]\right)^{-1} \tag{2.42}$$

with the Fermi energy E_F, and the Boltzmann constant k_B.

Following Shoeberg [Sho84] the effect of such a distribution on the "ideal" magnetization can be obtained by a convolution of the magnetization with the negative derivative of the Fermi distribution if the Fermi energy E_F is constant. We get

$$M = \int_{-\infty}^{\infty} M_0(E)\left(\frac{-\partial}{\partial E} f(E, E_F, T)\right) d\left(\frac{E}{T}\right). \tag{2.43}$$

It is possible to decompose the oscillatory part of the magnetization by a Fourier analysis into a sum of harmonic functions. The convolution of each Fourier term with the distribution fuction is equivalent to a multiplication of the amplitude of the harmonic term with the Fourier transformation of the distribution function

$$\frac{-\partial}{\partial E} f(E, E_F, T) = \left(2k_B T\left[1 + \cosh\left(\frac{E - E_F}{k_B T}\right)\right]\right)^{-1}. \tag{2.44}$$

The Fourier transformation of this function with respect to the variable $2\pi p k_B T/\hbar\omega_c$ is

$$F\left(\frac{-\partial f}{\partial E}\right) = \frac{x}{\sinh x}\ , \text{ with } x = \frac{2\pi^2 p k_B T}{\hbar\omega_c}. \tag{2.45}$$

Here is p the number of the Fourier component. This leads to a reduction of the pth Fourier component of the magnetic oscillations.

Because of the periodic nature of the dHvA effect it is valid to take only the first Fourier into account. Therefore the temperature dependence of dHvA oscillation follows

$$\Delta M = \Delta M_0 \frac{x}{\sinh x}, \quad x = \frac{2\pi^2 k_B T}{\hbar\omega_c} \tag{2.46}$$

with $\omega_c = eB/m^*$.

The reduction factor due to temperature

$$R_T = \frac{x}{\sinh x} \tag{2.47}$$

is multiplied with the intrinsic broadening parameter R_D.

In the case of an oscillating Fermi energy like in our actual measurements this is not strictly correct. However, to analyze our measured data we used this formulation as a first order approximation of the temperature dependence.

2.1.3 real 2DES in tilted magnetic fields

The magnetization of a real 2DES in tilted magnetic fields is expected to be influenced by all previously presented effects. We start with the Landau quantization and add the spin and valley splitting to get the actual energy levels. We also include the dynamic enhancement of the spin and valley splitting due to polarization in spin and valley quantum number. We get

$$E_{j,s,v} = \hbar\omega_c \left(j + \frac{1}{2}\right) + \frac{1}{2}\left(sg\mu_B^* B + E_{ex,0}(N_\uparrow - N_\downarrow)\right) +$$

$$\frac{1}{2}\left(vE_{v,0}B_{\perp} + E_{ex,0,v}(N_{+} - N_{-})\right). \tag{2.48}$$

The ideal magnetization amplitude $\Delta M_{ideal}/N = \Delta E/B$ is reduced by the intrinsic broadening and due to temperature. Additionally we have to account for the in-plane magnetic field resulting in an additional reduction factor $R_{||}$ with a characteristic B field dependence that gets more stronger at larger tilt angles. For the actual measured magnetization amplitude we get

$$\Delta M_{meas}/N = (\Delta E/B)R_D R_T R_{||}. \tag{2.49}$$

Coincidence method

By changing the angle between the 2DES and an constant external magnetic field both magnetic field components change their value. However, it is often instructive to keep the perpendicular component constant while increasing the in-plane component. This way the total magnetic field increases while the perpendicular component stays constant. The result for the energy spectrum is that the spin splitting increases whereas all other splittings stay constant. This leads to the so called "coincidence method".

By tilting the angle the energy levels start to move energetically up or down, depending on their spin quantum number. At specific angles these moving energy levels with different Landau quantum number cross each other. At this angles the energy gap of some of the filling factors is zero. This leads to a vanishing of the magnetization oscillation, i.e., $\Delta M = 0$. A schematic example of the coincidence method is shown in fig. 2.3. The ratio of $B/B_{\perp}$ depends on the angle α. The coincidence points are marked by vertical dashed lines. At these angles the energy gaps at certain filling factors are $\Delta E = 0$.

The combined energy spectrum in eq. (2.48) includes only one term depending on the total magnetic field B. Thus the energy difference at a given filling factor can be written as follows

$$\Delta E = \Delta S g \mu_B B + \gamma B_{\perp} \tag{2.50}$$

where γ includes all terms that depends only on the perpendicular component of the external magnetic field.

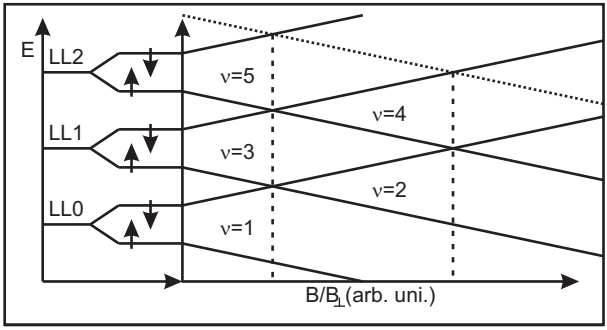

Figure 2.3: A schematic plot of the coincidence method. If B increases the spin splitting increases as well. At specific values of $B/B_\perp$ some of the energy levels cross. At these so-called coincidence points or angles (marked by vertical dashed lines) the energy gaps at certain filling factors vanish.

In the case of a pure spin gap the second term simplifies to

$$\Delta E = \Delta S g \mu_B B + \gamma E_C. \tag{2.51}$$

This is a generalization of the energy associated with a spin-flip in a 2DES. The first term is the Zeeman spin splitting energy ΔE_Z, which is assumed to be the only part which depends on the total field B. This relation should hold for the case of an 2DES that is infinitely thin. In this case the in-plane magnetic field component couples to the system only via the Zeeman energy. The perpendicular magnetic component governs the orbital dynamics. The second term is associated with the electron-electron interaction and depends on $B_\perp$ via the Coulomb energy E_C. It leads to an exchange enhancement of the spin splitting. This term also includes a possible difference in the valley splitting of the lower and upper spin branch, which also depends only on $B_\perp$.

Thus for every given filling factor the evolution with the angle α, i.e., the ratio between B_{total} and $B_\perp$ should exhibit the same slope.

Because g is a material parameter and μ_B is a constant both are not

expected to change during a measurement and B_{total} is determined at a given filling factor only by the angle α the only parameter to explain a irregular slope is the value of the spin S. A value $S \neq 1$ is associated with a excitation of multiple spins at once[Sch95]. In this case the parameter S describes the so called "skyrmion size" the number of spin that participate in the collective excitation.

2.2 Spin dynamics in ferromagnetic thin films

In this section we give a brief overview over the fundamental concepts of spin dynamics in ferromagnetic thin films. However, the main focus of this work is on the mechanical properties of nanomechanical bridges. For a more detailed treatment on spin dynamics see [Gie05, Neu08, Dür09].

We start from a semi-classical treatment of the magnetization. We assume that the magnetization M of the sample is spatialy uniform and can thus be described by a single vector $\vec{M} = \frac{d\vec{m}}{dV}$, with the magnetic moment $\vec{m}$ and the sample volume V. This assumption is valid for high magnetic fields and large samples.

The orbital magnetic moment m of an electron with the angular momentum $\vec{L}$ is

$$\vec{m} = \frac{q_e}{2m_e}\vec{L} \tag{2.52}$$

and the spin angular momentum S possesses the magnetic moment

$$\vec{m} = \gamma\vec{S} \tag{2.53}$$

with the gyromagnetic ratio γ.

The total angular momentum $\vec{J}$ is gained by the general addition rules and its rate of change $d\vec{J}/dt$ is proportional to the acting torque $\vec{m} \times \vec{B}_{int}$. Here, B_{int} is the internal magnetic field. Note, that the internal magnetic induction $\vec{B} = \mu_0\vec{H}_{int}$ may be significantly different from the externally applied magnetic induction $\vec{B}_{ex}$ depending on sample shape, material, and other influences.

The equation of motion for a magnetic moment is

$$\frac{d\vec{m}}{dt} = \gamma \frac{d\vec{J}}{dt} = \gamma \vec{m} \times \vec{B}_{int}. \tag{2.54}$$

Commonly this is written with the magnetization $\vec{M} = \sum_i \vec{m}_i / V$ as the sum over all magnetic moments per unit volume as

$$\frac{d\vec{M}}{dt} = -|\gamma| \mu_0 (\vec{M} \times \vec{H}_{int}). \tag{2.55}$$

Equation 2.55 describes a precession of the magnetization $\vec{M}$ around the direction of the magnetic field $\vec{H}_{int}$ with a constant magnitude of the magnetization. This can be see in fig. 2.4(a). Because this equation does not contain any damping the precession will continue indefinitely.

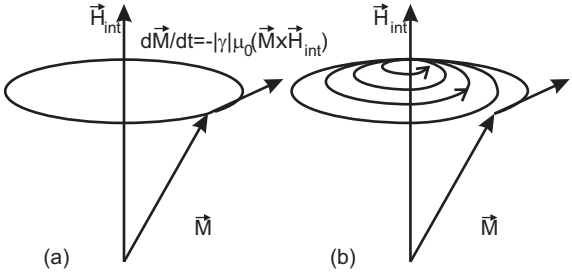

Figure 2.4: Precession of a macrospin $\vec{M}$ in an internal magnetic field $\vec{H}_{int}$ (a) undamped motion (b) motion with phenomenological damping taken into account

A phenomenological damping term has been included in [Gil55]. This lead to the so called Landau-Lifshitz-Gilbert equation

$$\frac{d\vec{M}}{dt} = -|\gamma| \mu_0 (\vec{M} \times \vec{H}_{int}) - \frac{\gamma a}{(1+a^2) M_s} \left(\vec{M} \times \frac{d\vec{M}}{dt} \right), \tag{2.56}$$

with the damping parameter a. In this case the magnetization vector spirals down to the equilibrium state which can be seen in fig. 2.4(b).

Ferromagnetic resonance

For a thin ferromagnetic film with an static in-plane magnetic field H the dynamic susceptibility $\chi(\omega)$ can be derived. With an additional oscillating external magnetic field H_{ex} that is in-plane, perpendicular to $\vec{H}_{int}$, and oscillating with frequency ω the susceptibility is given by [Cou04]

$$Re(\chi(\omega)) = \frac{\omega_B \omega_M(\omega_0^2 - \omega^2)}{(\omega_0^2 - \omega^2)^2 - \alpha^2\omega^2(\omega_H + \omega_B)^2}, \tag{2.57}$$

$$Im(\chi(\omega)) = \frac{\alpha\omega\omega_M(\omega_B^2 + \omega_0^2 - \omega^2)}{(\omega_0^2 - \omega^2)^2 - \alpha^2\omega^2(\omega_H + \omega_B)^2}. \tag{2.58}$$

The following definitions have been used: $\omega_B = \omega_M + \omega_H$, $\omega_0 = \sqrt{\omega_H\omega_B}$, $\omega_H = \gamma\mu_0 H$, and $\omega_M = \gamma\mu_0 M_{sat}$. Here, M_{sat} is the saturation magnetization.

The internal field can be written as $\vec{H}_{int} = \vec{H}_{ex} - \hat{N}\vec{M}$ if only demagnetization effects are taken into account via a diagonalized demagnetization tensor $\hat{N}$. Then, the resonance frequency is given by the Kittel formula [Kit48]

$$\omega_r = -|\gamma|\mu_0\sqrt{(H_{ext} + (N_y - N_x)M)(H_{ext} + (N_z - N_x)M)}. \tag{2.59}$$

The uniform precession of the magnetic moments at the frequency ω_r is called ferromagnetic resonance (FMR). This frequency is typically in the GHz regime.

2.3 Mechanical oscillations of doubly clamped beams

In this section the fundamental mechanical properties of doubly clamped beam are presented. We focus on calculating the eigenfrequencies. For excitations with high powers we introduce nonlinearities following the model of Duffing [Duf18]. Additionally we introduce two possible mechanism that couple microwaves to mechanical bridges.

Resonance frequency

In the following we discuss the equation of motion of a doubly clamped beam of length L, width w, and thickness t, oriented along the x axis, that is driven into flexural resonance with displacement along the y axis. The dynamic behavior of a flexural beam is most easily treated using the Euler - Bernoulli theory, which applies to beams with aspect ratios $L/t \gg 1$ [Tim74]. For an isotropic material, the transverse displacement $Y(x,t)$ of the beam centerline along the y direction, obeys the differential equation

$$\rho A \frac{\partial^2 Y}{\partial t^2}(x,t) = -\frac{\partial^2}{\partial x^2}\left(EI\frac{\partial^2 Y}{\partial x^2}(x,t)\right) \tag{2.60}$$

where ρ is the material density, $A = wt$ is the cross sectional area, E is Young's modulus, an I is the bending moment of inertia. The boundary conditions are $Y(0) = Y(L) = 0$ and $Y'(0) = Y'(L) = 0$ due to the clamped ends at $x = 0$ and $x = L$.

The solutions separate into

$$Y_n(x,t)) = Y_n(x)\exp(-i\omega_n t)), \tag{2.61}$$

with the spatial term

$$Y_n(x) = C_{1,n}(\cos(q_n x) - \cosh(q_n x)) + C_{2,n}(\sin(q_n x - \sinh(q_n x))). \tag{2.62}$$

The eigenvectors q_n satisfy $\cos(q_n L)\cosh(q_n L) = 1$. The first three eigenvectors are numerically calculated to be:

$$\begin{aligned} q_1 L &= 4.73 \\ q_2 L &= 7.85 \\ q_3 L &= 11.00. \end{aligned}$$

The angular frequencies are then given by

$$\omega_n = 2\pi f = \sqrt{\frac{EI}{\rho A}}q_n^2. \tag{2.63}$$

Resonances for high power excitations

To discuss the effects of high power excitations we follow the approach of Duffing [Duf18] to account for nonlinearities in the potential of an oscillator.

In the case of mechanical oscillations this is incorporated by adding a nonlinear elasticity term to the equation of motion. This results in the equation of motion of the so called Duffing oscillator

$$\ddot{x} + \delta\dot{x} + \beta x + \alpha x^3 = \gamma \cos \omega t. \tag{2.64}$$

In the case of $\alpha = 0$ eq. (2.64) reduces to the equation of motion of a forced and damped harmonic oscillator. For $\alpha > 0$ the spring is hardened by high power excitations.

Equation (2.64) can be solved following [Hol76] by assuming only weak periodic forcing, a weak nonlinearity, and weak damping. We rewrite eq. (2.64) with $\beta = \omega_0^2$ and obtain

$$\ddot{x} + \omega_0^2 x = -\delta\dot{x} - \alpha x^3 + \gamma \cos \omega t. \tag{2.65}$$

While all parameters on the right hand side of the equation are small due to our assumptions we find almost sinusoidal solutions of frequency $\omega_{sol} \simeq \omega_0$.

Using the van der Pol transformation [vdP34]

$$u = x \cos \omega t - \frac{\dot{x}}{\omega} \sin \omega t \tag{2.66}$$

$$v = -x \sin \omega t - \frac{\dot{x}}{\omega} \cos \omega t \tag{2.67}$$

eq. (2.65) can be written as a two dimensional equation system

$$\dot{u} = \frac{\sin \omega t}{\omega}[-\Omega(u \cos \omega t - v \sin \omega t) - \omega\delta(u \sin \omega t + v \cos \omega t) + \alpha(u \cos \omega t - v \sin \omega t)^3 - \gamma \cos \omega t]$$

$$\dot{v} = \frac{\cos \omega t}{\omega}[-\Omega(u \cos \omega t - v \sin \omega t) - \omega\delta(u \sin \omega t + v \cos \omega t) + \alpha(u \cos \omega t - v \sin \omega t)^3 - \gamma \cos \omega t]$$

with $\Omega = \omega^2 - \omega_0^2$. After using the method of averaging over $2\pi/\omega$ introduced by Krylov and Bogoliubov [Bog34] this simplifies to

$$\dot{u} = \frac{1}{2\omega}\left[-\omega\delta u + \Omega v - \frac{3}{4}\alpha(u^2+v^2)v\right], \tag{2.68}$$

$$\dot{v} = \frac{1}{2\omega}\left[-\omega\delta v + \Omega u - \frac{3}{4}\alpha(u^2+v^2)u - \gamma\right]. \tag{2.69}$$

Transformation into to polar coordinates $r = \sqrt{u^2+v^2}$ and $\theta = \arctan v/u$ yields

$$\dot{r} = \frac{1}{2\omega}(-\omega\delta r - \gamma\sin\theta), \tag{2.70}$$

$$r\dot{\theta} = \frac{1}{2\omega}\left(-\Omega r + \frac{3}{4}\alpha r^3 - \gamma\cos\theta\right). \tag{2.71}$$

Periodic solutions with frequency ω, amplitude A, and phase θ of the Duffing equation (2.64) are constant equilibrium points with A and θ of this equation system. It was shown by Holmes [Hol76] that the amplitude follows the equation

$$9\alpha^2A^6 + 24\alpha\Omega A^4 + 16(\Omega^2 + (2\delta\omega)^2)A^2 - 16\gamma^2 = 0, \tag{2.72}$$

after normalizing to $\omega_0^2 = 1$.

This equation can be solved numerically to determine the amplitude response for a given set of parameters δ, α, γ, and ω. In fig. 2.5 the amplitude of a Duffing oscillator for increasing excitation force is shown in the vicinity of the resonance frequency ω_0 of the harmonic oscillator.

Although a doubly clamped beam is not strictly a one dimensional harmonic oscillator the effects of nonlinearities in the potential are expected to be the same. This was shown by recently [Bra07, Kac09].

2.3.1 Microwave coupling to mechanical bridges

We limit the discussion of coupling mechanism to the two mechanisms that are typically used to excite oscillations of micro- and nanoscopic

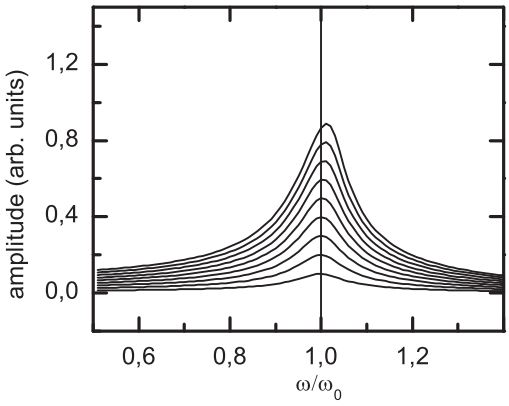

Figure 2.5: Amplitude of a Duffing oscillator versus normalized frequency for increasing excitation forces. Here ω_c is the resonance frequency of the corresponding harmonic oscillator.

mechanical devices. The magnetomotive coupling is based on the exciting gigahertz wave and the Lorentz force in an external magnetic field. It does not depend on the properties of the ferromagnetic material. The second coupling mechanism is based on the magnetostriction effect of the magnetic material. For a review of actuation techniques with a focus on NEMS see [Eki05]

magnetomotive coupling

If a nanobridge is also the conductor for the microwave, then a periodic current at the microwave frequency is running through the bridge. In an external magnetic field B each electron that carries the current is subject to the Lorentz force

$$F_L = e(\vec{v} \times \vec{B}) \tag{2.73}$$

with the velocity v of the electron and the electron charge e. This force transfers to the conductor. Thus we get the Lorentz force acting on a

conductor to be

$$F_L = l(\vec{I} \times \vec{B}) \tag{2.74}$$

with the length l of the conductor in the magnetic field. If the current $I(t) = I_0 \cos(\omega t)$ is alternating with frequency ω and we assume the magnetic field to be perpendicular to the conductor we get a periodic force

$$F_L(t) = lBI_0 \cos(\omega t) \tag{2.75}$$

acting on the conductor. This force acts as driving force for the doubly clamped beam.

magnetostriction coupling

The effect of magnetostriction describes the change of the shape of a ferromagnetic specimen induced by changes of the magnetization M. The elongation δl of a ferromagnetic material depends monotonically but not linearly on the magnetization M in the same direction. The effect can be use to deflect microscopic ferromagnetic cantilevers. In our group we recently used this effect to investigate interactions between surface acoustic waves (SAW) and spin dynamics [Hub09].

In a state when the magnetization is saturated, i.e. $M = M_{sat}$, and then tilted by tilting the external magnetic field by θ from the initial direction the elongation follows the form

$$\frac{\delta l}{l} = \frac{3}{2}\Lambda_0(\cos^2\theta - \frac{1}{3}). \tag{2.76}$$

Here, Λ_0 is the maximum elongation [Chi09]. Thus, in the saturation state the elongation is proportional to the component of the magnetization in each direction.

$$\frac{\delta l_x}{l_x} = \frac{3}{2}\Lambda_{sat}({M_x}^2 - \frac{1}{3}) \tag{2.77}$$

If the actual magnetization is below 50% of the saturation magnetization is was found theoretically [Chi09] and experimentally [Web25] that the elongation is almost zero.

Chapter 3

Experimental techniques

In this chapter the different measurement techniques used in the course of this work are presented. The chapter is divided into two main sections. In sec. 3.1.2 cantilever magnetometry is introduced. We used cantilever magnetometers to measure the magnetization of two-dimensional AlAs quantum wells. First, we introduce a newly designed cantilever setup with optical readout technique and 4-axis piezo based sample positioning system. Second, we discuss a cantilever magnetometer with a capacitive read out technique.

In sec. 3.2 two techniques for gigahertz spectroscopy are presented. We used a setup with a vector network analyzer (VNA) for frequency domain measurements and a time domain reflectometer (TDR) for time domain measurements to investigate the properties of nanomechanical bridges located in the inner conductor of a coplanar waveguide.

3.1 Cantilever magnetometer

Measuring the magnetization of 2DESs is a challenging task. The expected signal strength per electron is on the order of the effective Bohr magneton $\mu_B^* = \frac{e\hbar}{2m_e^*} = 1.97 \cdot 10^{-23}$ J/T [Ada85] in AlAs. With a

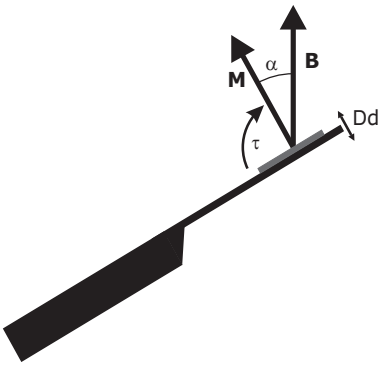

Figure 3.1: Schematic side view of a micromechanical cantilever magnetometer. The cantilever normal is tilted by an angle α with respect to the external magnetic field B. The torque $\vec{\tau} = \vec{M} \times \vec{B}$ is acting on the cantilever resulting in a deflection Δd of the cantilever.

typical electron sheet density of the order of 10^9 mm^{-2} the required sensitivity is about 10^{-14} J/T for a 1 mm^2 sample area.

Recent experiments focus on measuring the torque $\vec{\tau} = \vec{M} \times \vec{B}$ acting on an anisotropic magnetic moment $\vec{M}$ in a homogeneous external magnetic field $\vec{B}$ [Eis85a, Eis85b, Tem88, Pot96]. The first to observe the sawtooth shape as predicted for the de Haas-van Alphen effect in a 2DES were Wiegers *et at.* reported on samples with improved quality and a setup with improved sensitivity [Wie97] as compared to the earlyer experiments.

Various torsional magnetometer designs were used and perpetually improved by a number of groups [Sch02a, Zhu03]. For the measurements done in the course of this work we used another approach to torque magnetometry which is the micromechanical cantilever magnetometer (MCM) [Nau98, Har99, Har01, Höp01, Sti01, Sch00, Sch02b]. The MCMs used in this work were fabricated from AlGaAs/GaAs heterostructures similar to the ones used in [Spr07, Ruh08, Wil04].

The torque acting on the MCM is determined by measuring the

deflection Δd of the cantilever. In fig. 3.1 a schematic side view of cantilever as used in this work is shown.

The torque $\vec{\tau} = \vec{M} \times \vec{B}$ is only non zero when $\vec{M}$ is anisotropic and can be written as $\tau = MB \sin\alpha$ where α is the angle between $\vec{M}$ and $\vec{B}$. Because in a 2DES the orbital motion of the electrons is restricted to a 2D plane in the sample, the resulting orbital magnetism is expected to be parallel to the surface normal $\vec{n}$ of the sample. To achieve a torque the surface normal has to be tilted with respect to the external magnetic field $\vec{B}$ since $\vec{M} || \vec{n}$. For a known angle α the magnetization can then be calculated from the measured torque using

$$|\vec{M}| = \frac{\tau}{B \sin\alpha}. \tag{3.1}$$

Note, that we are only able to measure the component of $\vec{M}$ that is perpendicular to the magnetic field $\vec{B}$. If we know the angle between $\vec{M}$ and $\vec{B}$ we are able to calculate the total value of $\vec{M}$.

3.1.1 Optical Readout

To detect the deflection of the cantilever a fibre optical read out technique is used. The cleaved edge of a glass-fibre and the surface of the cantilever are forming a Fabry-Pérot resonator. This is shown in fig. 3.2(a). For a given wavelength and constant reflection parameters R_1 and R_2 of the resonator mirrors the reflected intensity R depends only on the distance d. The reflection of an ideal Fabry-Pérot resonator [Vau89, Hol49, Flü56] is not sufficient to describe the actual reflection pattern in our system. A detailed discussion about different models to incorporate loss factors is presented in [Bor08]. In particular taking into account an angle between both resonator planes like discussed by K. Chin[Chi07] is necessary and results in an important improvement of compared to simpler models [Mul91].

In fig. 3.2(b) the reflectivity R versus the distance d is shown in the model we used. In this case the reflectivity of the glassfibre is $r_1 = 0.04$ and the reflectivity of the surface is $r_2 = 0.3$. We took ten reflections into account and assumed a misalignment of 1.5°

We adjust the reflected intensity via the distance d to a point where

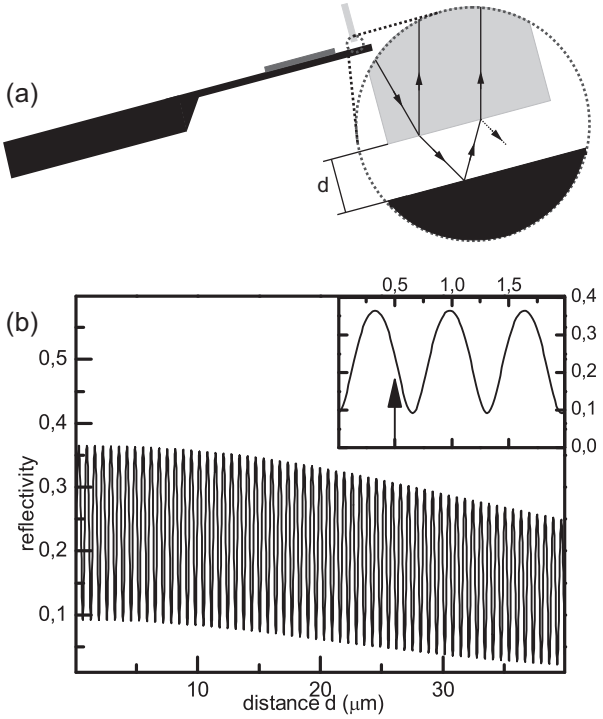

Figure 3.2: (a) Schematic side view of the optical read out technique. The cleaved edge of the fibre and the surface of the cantilever are forming a Fabry-Pérot resonator. The reflected intensity varies with the distance d. (b) Reflected intensity versus distance d. Inset shows detail close to $d = 0$. Exemplarily a working point is marked by an arrow.

the slope of the interference pattern is steepest. This so called working point is marked by an arrow in the inset in fig. 3.2(b). Here the sensitivity to distance changes Δd is highest.

The deflection is measured by keeping the reflected intensity constant. For this a controller applies a voltage to a stack of piezo electric plates to which the glass fibre is glued. The setup is shown schematically in fig. 3.3. The voltage applied to the piezo stack keeps the working point and thus the distance constant. For additional information on the feedback system see [Spr07, Bor08].

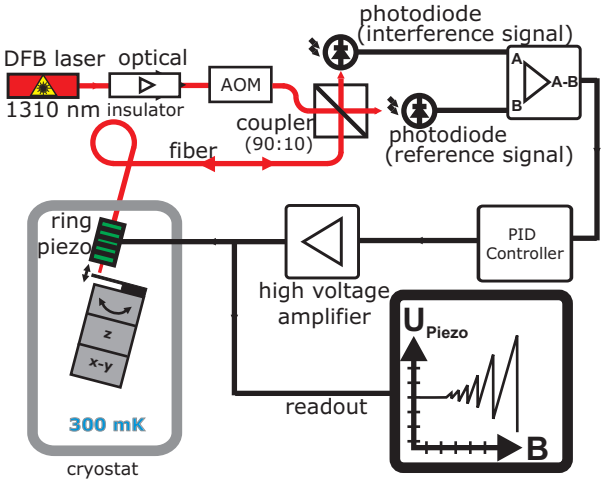

Figure 3.3: Setup for optical read out technique. By applying a voltage to the ring piezo stack until the reflected light intensity equals the set point.

The reflected intensity is amplified and used as input to the controller with the intensity value of the working point as set point. The controller applies a voltage via a high voltage amplifier to the piezo stack if the reflected intensity differs from the given set point. The voltage is applied until the set point is reached and therefore the distance is the same again. We measure the voltage applied to the piezo stack to calculate the deflection of the cantilever.

The exact length change of the piezo stack for a given voltage change depends strongly on the temperature and is only specified to be voltage independent for low temperatures in the order of 4 K [Pic07]. We use a technique to determine the expansion coefficient *in situ*. Therefore we manually adjust the interference signal to the set point by applying a voltage to the fibre piezo stack. We than increase the voltage further until we reach the next working point in the periodic interference pattern. The distance between these two points is known to be $\Delta d = \lambda/2$.

The optical read out technique can also be used to measure the deflection of nanomechanical bridges. In this case the constant distance mode is not useful because of the high frequencies of the bridges. Instead a resonant measurement technique[All98, Har00] can be used. For small deflections the reflected intensity is dependents linearly on the deflection. The frequency even of small amplitudes of oscillations can be measured by a frequency counter. For amplitudes $\ll \lambda/4$ the reflected intensity is directly proportional to the amplitude. In the course of this work we focus on static deflection measurements.

Piezo positioning system

Especially to measure nanomechanical bridges it is necessary to incorporate an *in situ* positioning system with sub-micron resolution. Not only it is necessary to adjust the sample to the exact lateral position of the 9 μm diameter fibre core but also the exact angle between fibre and surface is important. Therefore a piezo based sample positioning system in xyz and α direction was designed in the course of this work.

A schematic cross-section of the designed setup is shown in fig. 3.4. At the lower end the xy positioning system is located. On top is the z positioning system. Both were designed and constructed in the course of this work. The positioning systems are piezo-mechanical stepper actuators based on the slip-stick principle [Poh87] that was used successfully for scanning probe microscopy [Lyd88, All98, Mey05].

In our system the piezo-stacks are glued to a solid titanium base plate on the one side. The object that should be moved is mechanically

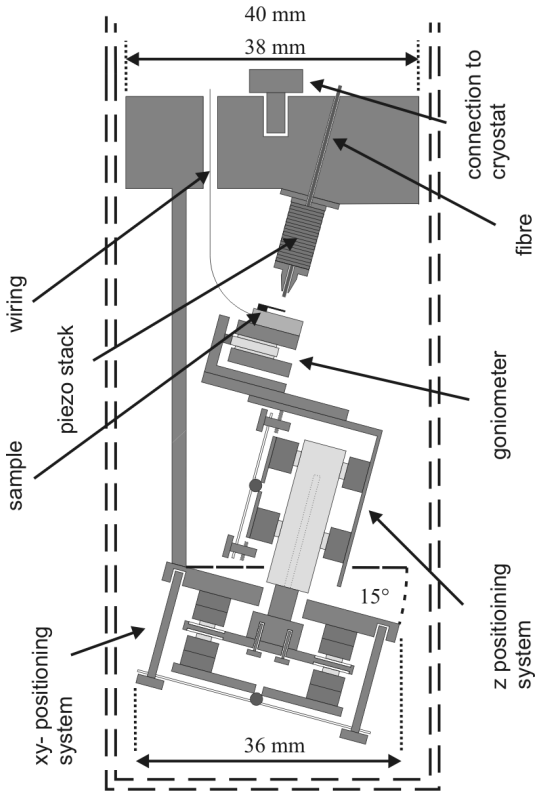

Figure 3.4: A schematic view of the designed sample positioning system. The dashed lines indicate the available space in the ^{3}He cryostat. The positioning system consists of a xy- piezo walker at the lower end. On top of the xy-walker the z-walker is located and above the goniometer to adjust the tilt angle α. The whole positioning system is tilted 15° with respect to the external magnetic field.

pressed to the other side of the piezo-stack using a molybdenum spring plate hinged on a small ruby sphere. If sawtooth-like voltage pulses are applied to the piezo-stacks the pressed connection either sticks to the stacks or slips depending on the slope of the voltage change and the inertia of the movable part.

If the voltage is increased slowly the object to move sticks to the piezo stacks and thus moves slowly in the expected direction. If the voltage drops fast back to zero the inertia keeps the object on its place. In this case it slips while the piezo stacks are moving to the starting position. A crucial parameter is the sticking friction coefficient. It can be adjusted by changing the contact pressure of the piezo-stacks to the object manually. In the following we discuss the different fundamental parts of the sample positioning system in detail.

z-walker

The z-walker consists of six shear piezo-stacks. These are pressed to a sapphire prism with triangular cross-section by a molybdenum spring plate. This can be seen in fig. 3.5(a). The contact pressure is adjusted by 4 screws and to ensure a uniform contact pressure a ruby sphere is incorporated to act as an articulation. To improve the sliding properties on top of each piezo stack a plate of amorphous Al_2O_3 is placed.

One step of the z-walker is between 100 nm and 250 nm at room temperature. It increases with increasing voltage and temperature but it also depends on the contact pressure and the amount of piezo plates per stack. The whole travel path is up to 6 mm and is used for the coarse approach between the sample and the glass fibre. The fine tuning of the distance is performed with the ring piezo to which the glass fibre is glued.

xy-walker

The xy walker is based on the same principle as the z walker. A schematic view can be seen in fig. 3.5(b). Due to the limited space in the ^{3}He cryostat a combined x and y walker was designed. Instead

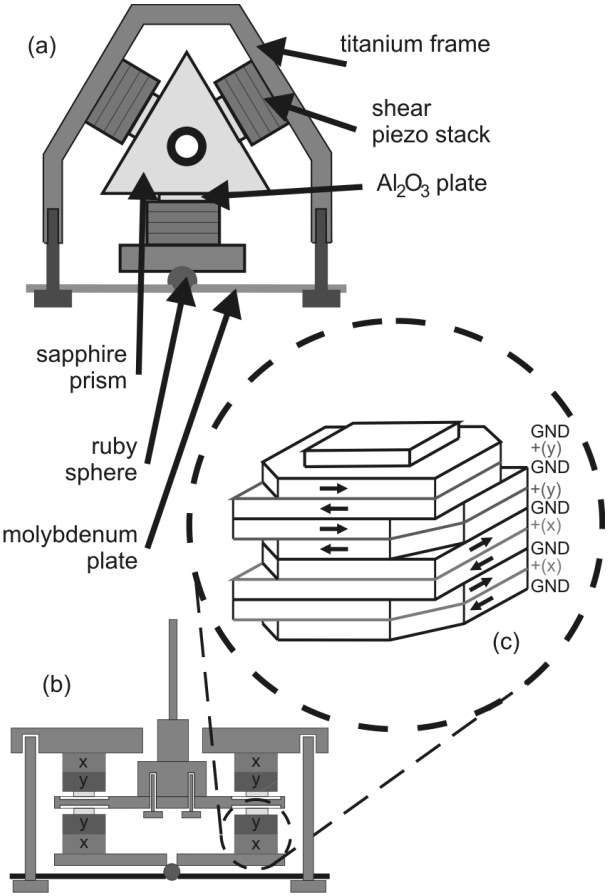

Figure 3.5: (a) A schematic cross-sectional view of the designed piezo walker in z direction. (b) View of the xy walker. (c) Design of a piezo stack for the xy walker.

of placing two separate linear piezo walkers like the z-walker on top of each other a single "2-in-1" device was designed. To archive this a single plate is positioned between six piezo-stacks. Each stack comprised of eight piezo plates. Four of the piezo plates are rotated by 90° with respect to the others as can be seen in fig. 3.5(c). The $+x$ and the $+y$ voltage can be applied separately allowing for a biaxial slip-stick operation.

The xy-walker is used for lateral positioning of the sample under the glass fibre which is particulary necessary to measure nanomechanical devices. Because of differences in the coefficient of thermal expansion of the used materials the exact positioning has to be performed after the cool down to liquid He temperatures.

Due to the "2-in-1" solution the movement in both directions is not guided. Thus a small drift perpendicular to the expected movement direction is inevitable. In addition a rotation of the moving plate around the z axis can occur if the piezo stacks do not all have the same performance. Therefore only small distances should be moved *in situ*.

For *in situ* positioning it is rather important to gain information on the actual position of the fibre core with respect to the sample. For this we measure the reflected intensity while scanning the surface of a sample. An example is shown in fig. 3.6(a). We prepared a double cross structure of 300 nm deep trenches in a GaAs substrate. The surface of the sample was roughened by wet etching before the trenches were prepared to ensure the same reflectivity in the trench and on the surface. A line scan across the sample is shown in fig. 3.6(b). The measurements were made at room temperature in the constant distance mode described above. The piezo voltage is plotted versus the number of walker steps.

The line scan does not show the expected shape of two consecutive trenches. Instead it shows an linear increase with four steplike structures. We attribute the overall increase to a small misalignment of roughly 1° between the glass fibre and the sample surface. The four decreasing steps of different heights can be associated with the trenches. The relative distances between the slope positions correspond roughly to the relative distances of the two trenches.

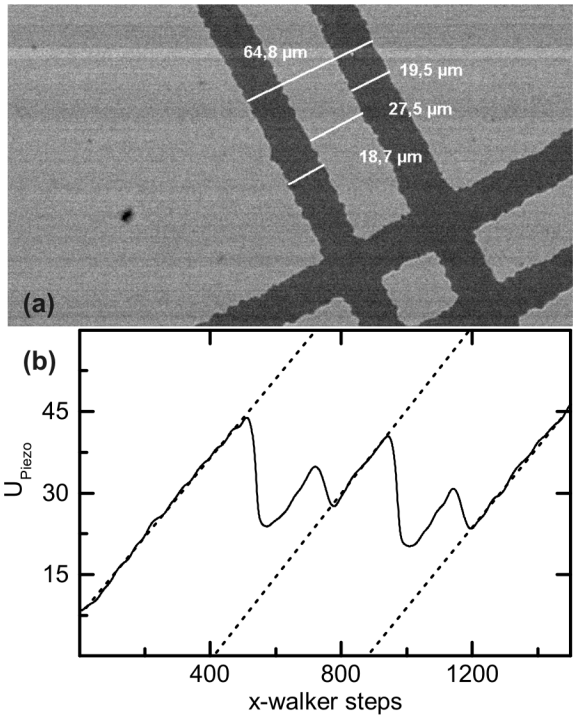

Figure 3.6: (a) GaAs sample with a 300 nm deep etched double cross structure.(b) Line scan across the sample in (a). We show the piezo voltage necessary to keep the reflection constant. Dotted lines denote same surfaces but at different fringes corresponding to the periodicity in the interference pattern. The voltage between the dotted lines equals $\lambda/2$. Both taken from [Bor08].

In [Bor08] the phenomena was analyzed in detail and explained by the interference pattern of a Fabry-Pérot resonator when the surface of the substrate consists of two planes with different distances to the surface of the fibre. This is schematically shown in the upper part of fig. 3.7 for two relevant scenarios. We go beyond the analysis in [Bor08] and expand the model to different materials with different reflectivity and an additional misalignment between the glass fibre and the surface. Thereby we are able to predict the reflection signatures of actual surface features of samples used for future measurements.

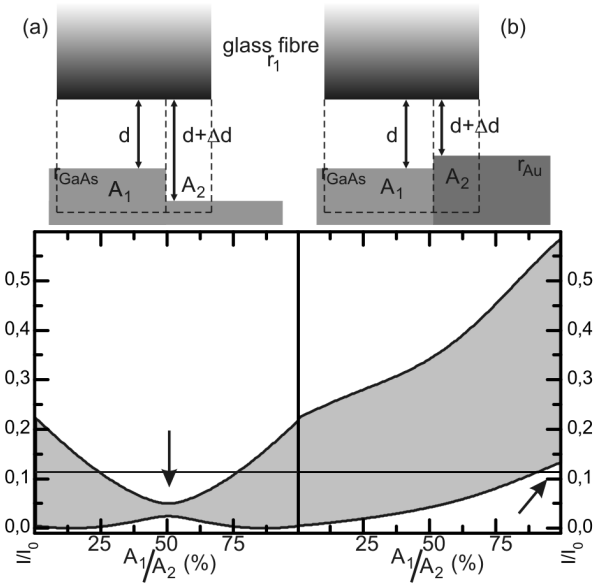

Figure 3.7: Simulation of reflection while scanning across the edge of a evaporated gold circuite. The maximum, minimum, and the average of the interference pattern is shown versus the area ratio A_1/A_2. We assumed the following reflectivity: (a) $r_{GaAs} = 0.08$, $r_{glassfibre} = 0.04$, depth of the trench $\Delta d = 300$ nm. (b) $r_{GaAs} = 0.08$, $r_{Au} = 0.35$, $r_{glassfibre} = 0.04$, thickness of the gold layer $\Delta d = 21$ nm.

To simulate the overall reflectivity R of the resonator we assume only the first reflection of the beam needs to be taken into account. This is a valid assumption if both side of the resonator have a low reflectivity. Additionally we assume an ideal Fabry-Pérot resonator, i.e., neglecting losses at the boundary of the resonator. With the wavevector $k = 2\pi/\lambda$ we get:

$$\begin{aligned} R(x) &= (1-x)(r_1 + t^2 r_{2a} \exp(i(2dk + \pi))) \\ &\quad + x(r_1 + t^2 r_{2b} \exp(i(2dk\pi + 2\Delta dk))). \end{aligned}$$

In this case $x = A_1/A_2$ is the fraction of the areas with different distance to the fibre. In the simulation we varied the distance d for increasing x to get the maximum and minimum of the interference pattern. In fig. 3.7(a) both extremal values are shown for the trenches we showed in fig. 3.6. In this case the distance $\Delta d = 300$ nm and the reflectivities are equal for both areas $r_{2a} = r_{2b} = 0.08$. The horizontal solid line in fig. 3.7(a) indicates the working point on the GaAs surface. The maximum interference intensity goes down till it crosses the solid line indicating the working point. Afterwards it goes up. For all value of x where the maximum is below the solid line working point can not be reached by varying the distance d.

In fig. 3.7(b) the simulation is shown for a distance $\Delta d = 21$ nm and the reflectivities corresponds to GaAs ($r_{2a} = 0.08$) and gold $r_{2b} = 0.35$. We extracted the values of the reflectivity of gold by comparing our measurements with corresponding simulations. The minimum and the maximum of the interference pattern both increase with increasing x. At some point the minimum crosses the working point again indicated by the horizontal solid line.

If the working point is not within the shaded area the constant distance mode is not working. Two points where this happens are marked by arrows in fig. 3.7(a) and (b), respectively. The controller applies a voltage to the tube but the reflected intensity can not be matched to the preset working point regardless which voltage is applied.

There are conditions that result in situations where the preset working point is out of reach. The first is the distance Δd between both layers. If the distance is $\Delta d = (2n+1)\lambda/4$ the reflected beams of both layers interfere destructively regardless of the distance d. In this case

the maximum of the interference pattern drops down.

The second condition is the ratio between the reflectivity of both layers ($r_{GaAs}/r_{Au} = 0.08/0.35$). In this case the minimum interference intensity of gold is higher than the working point at GaAs.

Incorporating a misalignment between surface and glass fibre does not change this result. It reduces the total reflection of the resonator depend on the distance between both resonator planes. Because the changes in distance for layer to layer or only small $\Delta d/d \ll 1$ the reduction factor can be assumed to be constant.

The simulations predict a problem if we use gold layers to mark positions on samples. The problem exists if the markers have a significantly different reflectivity than the rest of the sample surface, or if the thickness of the marker is in the range of 300 ± 100 nm.

To circumvent the problems it is necessary to either not scan the sample surface in the constant distance mode or to use different markers. A possible marker could be an etched trench with a depth of 50 nm for example. However, the necessary conducting circuits on the cantilever surface would still lead to problems as described above.

goniometer

We used a commercially available piezo goniometer from attocube systems. The angular range of the device is $\pm 3.6°$. It is also based on the slip-stick technique. The goniometer does not just change the angle but is moving on a circle with the center of rotation 40 mm above the goniometer. Thus an angular movement is always connected to a lateral movement in x-direction.

The goniometer enables us to adjust the angle between the glass fibre and the sample *in situ*. An angular misalignment results in a significant reduction of the interference amplitude and thus results in a decrease of sensitivity. A misalignment of 5° almost reduces the interference amplitude to zero [Bor08].

Unfortunately the piezo positioning system did not work as expected under the extreme experimental conditions. In particular the xy-walker

did not work reliably at temperatures below 70 K. Thus the measurements on AlAs quantum wells shown in chapter 5 were taken with a capacitive read out technique presented below. The measurements on nanomechanical bridges in chapter.6 are limited to gigahertz spectroscopy.

3.1.2 Capacitive Readout

The fundamental principle of operation for capacitive and optical cantilever magnetometers are the same. The difference lies solely in the detection of the deflection of the cantilever.

For capacitive read out the cantilever design is slightly different. Instead of a reflective gold area on top of the cantilever the backside of the sensor is metallized. The metallized backside of the cantilever and a fixed metallic counter electrode on the substrate are forming a plate capacitor with the capacitance

$$C_0 = \frac{\epsilon_0 A}{d}, \tag{3.2}$$

with the area of the metalization A and the distance d between the cantilever backside and the counter electrode as shown in fig.3.8.

A deflection Δd of the cantilever can be measured as a change in the capacitance. If the deflection is small, i.e., $\Delta d \ll d$ this is given by

$$C(d+\Delta d) = \frac{\epsilon_0 A}{d+\Delta d} = \frac{\epsilon_0 A}{d}\left(1+\frac{\Delta d}{d}\right)^{-1} \tag{3.3}$$

$$= C_0 - \Delta C + O(\Delta d^2) \tag{3.4}$$

A torque acting on the cantilever results in a deflection. Within the small-angle approximation the corresponding change in the capacitance depends linearly on the torque

$$\tau = K\Delta C, \tag{3.5}$$

with a calibration constant K characteristic for each particular sensor.

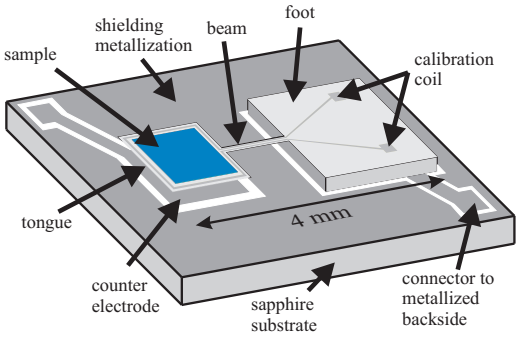

Figure 3.8: 3D schematic view of a cantilever with capacitive read out.

Experimental Setup

The measurements presented in chap. 5 were performed in a vacuum loading ^{3}He-cryostat with a superconducting coil at the Technical University Munich. The magnet coil provides a magnetic field up the 14.5 Tesla. The MCM is mounted on a Swedish rotator [Wil09] providing the possibility to rotate the whole MCM with respect to the external magnetic field.

The capacitance between the backside of the cantilever and the counter electrode is measured with a three-terminal method based on an ultra-sensitive capacitance bridge. The MCM is connected via coaxial cables providing accurate shielding. The capacitance data C were taken while continuously sweeping the magnetic field.

Roughly three measurements per second were taken. To achieve a high density of measurement points the sweep rate of the magnetic field was selected to be low (≤ 0.1 T/min). A blue light emitting diode (LED) was incorporated in close proximity to the MCM to perform illumination procedures using the persistent photoeffect.

Calibration

To determine the absolute value of the dHvA oscillation amplitudes, the sensor is calibrated by applying a known force to the cantilever. From the resulting capacitance change ΔC the calibration constant K can be calculated.

A dc-voltage U is applied between the metallic backside of the cantilever and the metallic ground plate. This causes an attractive electrostatic force

$$F = -\frac{\partial W}{\partial d} = -\frac{\partial}{\partial d}\left(\frac{1}{2}CU^2\right) = -\frac{\partial}{\partial d}\left(\frac{\epsilon_0 A}{2d}U^2\right) = \frac{\epsilon_0 A}{2d^2}U^2. \quad (3.6)$$

The voltage we apply is small so we assume the angle γ between the force F and the cantilever surface with length L is always 90°. Thus we get the corresponding torque

$$\tau = \frac{2}{3}FL = \frac{CL}{3d}U^2. \quad (3.7)$$

The prefactor of 2/3 arises from the difference in cantilever deflection via a torque or via a force. For details see [Wil04].

Measuring the change in the capacitance as a function of the applied voltage yields a quadratic function

$$\Delta C = k_u U^2, \quad (3.8)$$

with the fit parameter k_u. This parameter is used to calculate the calibration constant

$$K = \frac{LC_0}{3dk_u}, \quad (3.9)$$

under the assumption of $\Delta C \ll C_0$.

In the experiments, we determined a calibration constant K for every angle α separately, and checked that the conditions $\Delta C \ll C_0$ and $\gamma \simeq 90°$ are always fulfilled.

Data processing

To derive the magnetization from the raw capacitance data we use the following procedure: We subtract the capacitance at $B = 0$ from the

measurement signal and get the magnetization by multiplying with the calibration constant and dividing by $B \sin \alpha$

$$M = K \frac{C - C(B = 0)}{B \sin \alpha} \tag{3.10}$$

Afterwards we extract the oscillatory part of the magnetization by subtracting a smooth background signal. For this a polynomial of 4th to 6th order is fitted to the experimental data and then subtracted. This is done for each magnet field sweep separately. The resulting oscillatory part of the magnetization is averaged over a field window of 0.01 T to reduce the noise level. We averaged multiple magnet field sweeps if available to improve the signal-to-noise ratio further.

3.2 Gigahertz spectroscopy

In this section the two setups for broadband spectroscopy are described. Firstly we show the setup to measure in the frequency regime performed with a vector network analyzer (VNA). Secondly the setup for time domain measurement with a fast digital sampling oscilloscope (DSO) and time domain reflectometer (TDR) module is shown. The design and the preparation of the CPWs is shown in chap. 4.2.

Most gigahertz spectroscopy measurements performed in this work used a special liquid helium cryostat with a superconducting coil for transverse magnetic fields up to $B = 2.5$ T. Although we also performed measurements with a slightly different room-temperature setup we focus here on the cryostat setup. For additional information on the room-temperature setup see [Dür09, Neu08].

For the excitation and detection of nanomechanical bridges a broadband GHz spectrometer was used. The setup used inductive detection. The exciting microwave is transported to the sample by a micron-size CPW. The dynamic response of the sample is picked up inductively by the same CPW and delivered to the detector. A schematic view of the setup is shown in fig. 3.9(a).

3.2.1 Cryostat setup

To get access to high out-off-plane magnetic fields a special liquid helium cryostat was used. A photograph of the system shown in fig. 3.9(b). The cryogenic microwave probe station includes a superconducting magnet providing out-of-plane magnetic fields up to ±2.5 T.

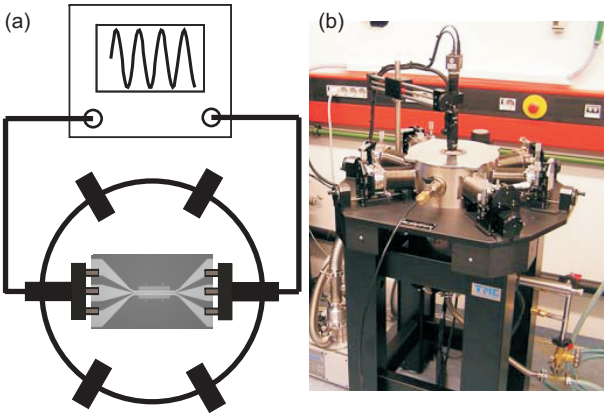

Figure 3.9: A schematic view of the GHz liquid helium cryostat.

The probe station provides six micro positioning arms. Each of these can be moved individually along the $x - y - z$ axis. A limited tilting around their respective x axis is also possible. The sample stage can be tilted around the z axis by ±5°. We mounted microwave probe tips to two of the arms to contact each side of the coplanar waveguide we used for our measurements.

3.2.2 Frequency domain setup

For experiments in the frequency domain a vector network analyzer (VNA) is used for excitation and detection of microwaves. The VNA emits a transverse electromagnetic microwave with a frequency be-

tween 10 MHz and 26.5 GHz and detects the scattering parameters (S-parameters) of the sample. The parameters are defined by

$$\hat{S}_{11}(\omega) = \frac{\hat{V}_{refl}(\omega)}{V_0(\omega)}$$

$$\hat{S}_{12}(\omega) = \frac{\hat{V}_{trans}(\omega)}{V_0(\omega)} \tag{3.11}$$

with the incident voltage V_0, the reflected voltage V_{refl}, and the transmitted voltage V_{trans}. All voltages are complex and so are the scattering parameters. The measurement is performed from both sides separately. Thus we get all possible scattering parameters S_{11}, S_{12}, S_{22}, and S_{21}.

The concept of S-parameters is more common in the field of electrical engineering to describe complicated networks. From a physical point of view the incoming microwave excites dynamics (magnetic or mechanical). If no resonance condition is met in the sample only a small part of the microwave is reflected because of the specially designed CPWs. The excitation of magnetization dynamics results in a second microwave emitted by the magnetic material due the moving magnetic moments. Both microwaves superpose.

If the sample is in resonance, the amplitude of the second microwave is large and 180° out-of-phase with the exciting microwave. This leads to a absorption dip in the transmission parameters. The same picture is valid for mechanical resonances of nanomechanical bridges in the inner conductor of the CPW. The oscillating bridge induces a microwave in the conductor that counteracts the incident microwave.

To extract the small changes in the S parameters due to FMR or mechanical resonances we subtract the spectrum with the highest available external field. Thereby we subtract all effects in the spectrum which originate from the setup and CPW.

3.2.3 Time domain setup

To investigate the properties of nanomechanical bridges in the time domain we used a digital sampling oscilloscope (DSO) with a time

domain reflectometry (TDR) module. The TDR module emits a 500 mV step pulse with a rise time of 11.7 ps. This voltage step corresponds to a current step in the inner conductor of the CPW.

The detectors of the DSO are triggered by the step pulse such that the jitter is only 800 ps. By this means one can measure stroboscopically with a high time resolution. Note that due to the stroboscopic measurement it is only possible to measure repeatable effects that are induced by every induced pulse. Typically we average over several hundred measurements. Therefore stochastic processes are averaged out in our measurements. The average is necessary to increase the signal-to-noise ratio that is low in our measurements compared to a real-time oscilloscope.

Considering the Fourier transform of the step pulse and the bandwidth of the DSO it is possible to excite dynamics up to $v = \frac{1}{\tau} = 30$ GHz. While the VNA excites always continuously the TDR gives only a short excitation pulse. The following movement is a free movement.

We present measurements on nanomechanical bridges taken with both setups in chap. 6.

Chapter 4

Preparative methods

In this chapter we present the preparative methods used in this work. In sec. 4.1 we show the sample processing of the AlAs quantum well that is necessaryprocess to place the sample on a cantilever magnetometer in flip chip technique.

In sec. 4.2 the preparation of coplanar waveguides (CPWs) is shown. We focus on the preparation of nanomechanical bridges in the inner conductor of CPWs. A Focused Ion Beam (FIB) setup is used to prepare the nanomechanical bridges.

4.1 Aluminum arsenide quantum wells

Since the invention of modulation doping of semiconductor heterostructures the evolving low dimensional electron systems at the interface between AlGaAs and GaAs are subject to intensive research. Recently, in particular electron systems in AlAs quantum wells have shown novel and intriguing physics [Sha06, Vak04, Shk05]. The conduction band minima of the indirect semiconductor AlAs are at the X-points of the Brillouin-zone (BZ). The Fermi surfaces exhibit an elliptical shape as can be seen in fig. 4.1. Because only half of each of the six valleys is

located in the first BZ a threefold valley degeneracy results.

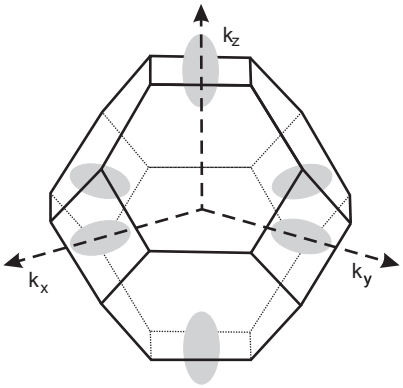

Figure 4.1: Schematic view of the first Brillouin zone of AlAs. The three valleys (6 half valleys at each X-point) are shown in grey.

The electrons in the valleys exhibit a, compared to GaAs ($m^* = 0.067m_e$), significantly larger and strongly anisotropic effective mass. The longitudinal mass is $m_l = 1.1m_e$ and the transversal mass is $m_t = 0.2m_e$ [Ada85]. The relevant mass for magnetization measurements is the cyclotron mass $m_c = \sqrt{m_l m_t} = 0.47m_e$.

The quantum well used in the work is grown using molecular beam epitaxy at the Walter-Schottky-Institute by Dasgupta *et al.*. The relevant part of the heterostructure is shown in fig. 4.2(a). It consists of a a 15 nm wide AlAs layer with AlGaAs barrier layers. On top is a GaAs capping layer. The quantum well forms in the AlAs layer. Due to lattice mismatch in growth direction biaxial strain in the quantum well is induced. The strain results in a drop in energy of the in-plane valleys of approximately 16 meV[vK89]. Thus only a twofold valley degeneracy remains. For additional information on the AlAs quantum well heterostructure see [Das07, Das08b, Das08a].

The specific energy level structure of a 15-nm-wide AlAs quantum well, as can be schematically seen in fig. 4.2(b), was calculated using the

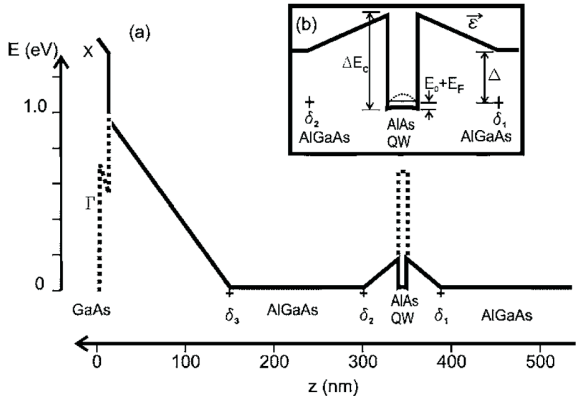

Figure 4.2: Heterostructure of the samples. In our case $d = 15$ nm. The figure was taken from [Das07]

simulation code nextnano^3 [nex]. We obtain a level spacing of 16.4 and 17.5 meV to the next higher subband in the out-of-plane and in-plane valley, respectively. Under the assumption of two occupied in-plane valleys the Fermi energy can be calculated from the carrier density n_S to be $E_F = 0.6$ meV. The difference of 15.8 meV is a strong indication that coupling to higher subbands has only minor impact on the level sequence in this case.

4.1.1 Sample Preparation for flip-chip technique

To account for the geometry of the in-plane valleys different samples were prepared with respect to the valley axis. This is shown in fig. 4.3(a). We used sample 1 to intentionally avoid recently reported in-plane magnetic field induced asymmetry between the two valleys[Gok08]. Both of the other samples are not symmetric with respect to the valley axis.

The sample preparation steps are schematically shown in fig. 4.3(b). In step one the mesa of the electronic system is defined by optical

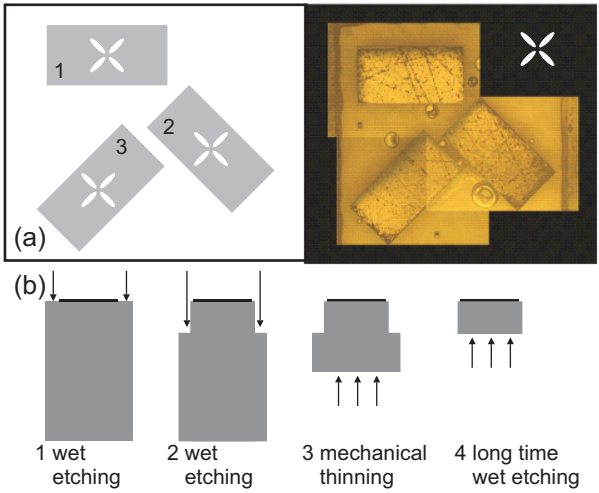

Figure 4.3: (a) Orientation of the sample with respect to the valley axis. Right: combined photographs taken from [Hua08]; left: schematic view of the samples. The in-plane valleys are sketched. (b) Preparation steps. 1) Mesa etching, 2) contour deep etching, 3) mechanical thinning from the back side, 4) long time wet etching until only the sample mesas are left.

lithography. We used a wet etching process to define the mesa. In step two the contour of the sample is defined by optical lithography. The wet etching of the contour defines the thickness of the sample.

In step three the sample is placed up-side-down on a glass substrate and is mechanically thinned down from the backside to roughly 50 μm. Step four is a long-time etching process from the backside that is stopped when the contour of the sample mesas are freed.

Afterwards the samples are cleaned and dried and placed on a cantilever by flip-chip technique. Additional information on the sample preparation can be found in [Hua08].

4.2 Nanomechanical Bridges

The determine the properties of nanomechanical bridges we use broadband VNA measurements. These are performed using coplanar-waveguides (CPWs) which have been specially designed to be impedance matched to 50 Ω. This is necessary to perform measurements up to 30 GHz. For further information on CPW design see [Gie05, Dür09]. The CPWs are prepared using optical lithography and an e-beam evaporator for metal thin films.

The nanomechanical bridges were processed by a focused ion beam (FIB) machine setup. The FIB is incorporated in a scanning electron microscope (SEM) which enables us to observe the preparation process on the micron scale *in situ*. A schematic cross section of a CPW is shown in fig. 4.4. The microwave is applied to the inner conductor and results in high frequency magnetic fields h_{rf} around the inner conductor. Note, that this magnetic field is almost in-plane especially directly under the inner conductor.

As both outer conductors are grounded the electrical fields e_{rf} are straight between the inner and the outer conductors. In the middle right above and below of the inner conductor the electrical fields are dominated by strayfields.

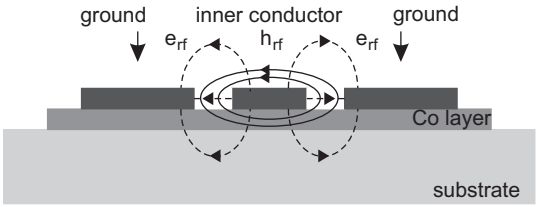

Figure 4.4: Schematic cross section of the CPW. A microwave running through the inner conductor creates a magnetic rf field

CPW preparation with optical lithography

The CPWs used in the course on this work were prepared by optical lithography. The substrate pieces are cleaved from a commercially available GaAs(001) wafer. The CPW design we used exhibits a 2 μm wide inner conductor that is 400 μm long. The distance to the ground lines on both sides is 1 μm. We used a two layer photo resist system for every lithography step to ensure homogenously straight and steep edges of all metal layers.

In the first lithography step a ferromagnetic Co-layer with a thickness of 21 nm is deposited. The Co-layer has the dimensions of 120×300 μm^2. The layer is deposited by e-beam evaporation. In fig. 4.5 the Co layer can be seen under the completely processed CPW. The marker than can be seen are also produced in this step and are used to align the next lithography step to the first one.

After the Co layer is deposited a thin layer of silicon dioxide is deposited over the whole sample to prevent a short-circuit of the ground line and the inner conductor of the CPW via the Co layer. The silicon dioxide layer is deposited by sputtering and is roughly 5 nm thick. This layer can not be seen on the micrograph. In the next step the CPW is processed on top of the Co layer. The CPW consists of a 4.5 nm thick chromium layer, a 100 nm thick silver layer, and a 21 nm thick gold cap. These were deposited subsequently without removing the sample

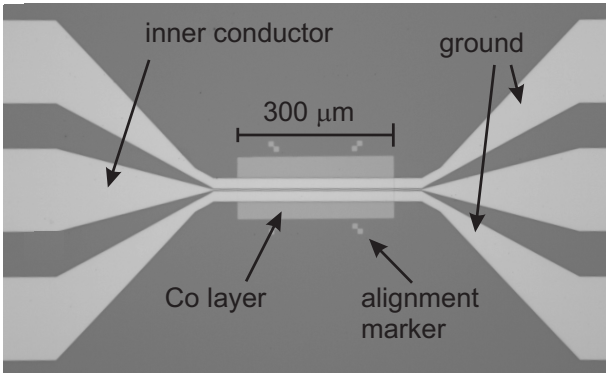

Figure 4.5: Optical micrograph of a CPW used in this work.

from the deposition chamber.

Focused Ion Beam processing of nanobridges

The preparation of the nanomechanical bridges is done completely by FIB milling. While the preparation of CPWs by optical lithography enables us to produce several CPW on one sample simultaneously the preparation of nanomechanical bridges needs to be optimized for each bridge individually.

We used a Zeiss "NVision 40" crossbeam setup that combines FIB and SEM as a shared facility at the Technical University of Munich and the Walter-Schottky-Institute. A crucial process during the preparation is the alignment between the electron beam of the SEM part and the ion beam of the FIB part. This alignment has to be optimized for every processed nanobridge separately.

The alignment is necessary to be able to define the area that is going to be milled by the FIB while operating in SEM mode. Although it is possible to observe the surface with the ion beam itself this is not the recommended operation mode, because the ion beam, even when in the

imaging mode, significantly damages the surface of the sample.

As milling parameters a milling current $I_M = 10$ pA was used. The overall milling time was distributed to 5 milling processes that were performed subsequently on the area to mill. These parameters are optimized to provide as little milling as possible outside of the designated area. Also the roughness of the nanobridge edges is reduced by this choice of parameters.

Another process that needs to be taken into account is the redeposition of the milled material. The first milling step is performed to confine the inner conductor of the CPW. Thereby the width of the nanobridge is defined. We mill two deep trenches symmetrically in the inner conductor. The trenches are 2 μm long 1 μm wide and roughly 1 μm deep. The FIB mills under an incident angle of 0°. This can be seen in fig.4.6 in the upper image. Around each trench a small ridge can be seen. This is due to redeposition of the milled material. The edges of the trenches are smooth and apart from some little peaks the ground is even.

After milling the trenches the sample is tiled to 54° around the inner conductor axis. A second milling process with the same parameters is used to cut under the remained part of the inner conductor. To obtain a symmetrical nanobridge this process is repeated while the sample is tilted to $-54°$. The area to mill is in both cases located directly under the deposited metal layers where the GaAs substrate begins. The GaAs can be easily recognized in the SEM image due to the significantly lower surface roughness.

The bottom image in fig. 4.6 shows the nanobridge after the completed production cycle. The black trench under the bridge is the milled area. The effects of redeposition can be clearly seen in this image.

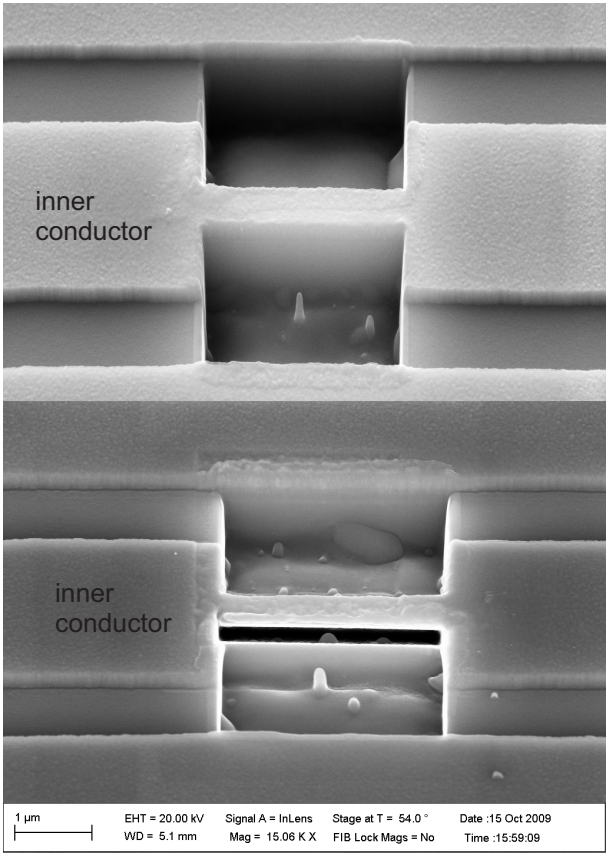

Figure 4.6: SEM images the two steps process of the preparation of a nanomechanical bridge. Top: Confining of the inner conductor of the CPW by FIB under incident angle of 0°. Bottom: Undercutting the confined inner conductor with FIB under an incident angle of 54° to get a free standing nanobrdige.

Chapter 5

Magnetization measurements on AlAs quantum wells

Magnetization measurements on aluminum-arsenide (AlAs) quantum wells are presented in this chapter. In this system two anisotropic conduction band valley are occupied and the effective cyclotron mass is large. This makes a 2DES in an AlAs quantum well an interesting, strongly interacting, electron system with an additional pseudo-spin degree of freedom.

The data presented in this chapter are divided in two main sections. The experiments were performed using micromechanical cantilever magnetometry with a capacitive readout. This is a powerful and well established measurement technique. We shown angular dependent measurements in sec. 5.1 as well as temperature dependent measurements in sec. 5.2.

A part of the results presented in following section has been published in [Win09]. The measurements were taken on an 15 nm wide AlAs quantum well embedded in $Al_{0.45}Ga_{0.55}As$ barrier layers. The

heterostructure was grown on a (001) GaAs substrate using molecular beam epitaxy. Details on the AlAs system can be found in chap. 4.1.

Due to different lattice constants of the layers biaxial strain induces an energy drop of approximately 16 meV in both in-plane valleys whereas the out-of-plane valley remains unaffected. Electrons in the in-plane valleys show an anisotropic effective electron mass of $m_l = 1.1\ m_e$ and $m_t = 0.2\ m_e$ [Ada85] and therefore a cyclotron mass of $m_c^* = \sqrt{m_l m_t} = 0.47\ m_e$ which is the relevant mass for dHvA measurements. Since the dHvA oscillation amplitude scales inversely with the effective mass magnetization measurements on this system present an experimental challenge.

The mass of $m_c^* = 0.47\ m_e$ is about 2.5 times larger than in Si/SiGe heterostructures. In SiGe successful magnetization measurements have been reported in Ref. [Wil06]. Thus a very high electron mobility μ is needed to reduce the Landau level broadening to a point where pronounced dHvA oscillations occur.

Towards this end the modulation doping structure was optimized and reached an electron mobility of $\mu_e = 4.2{\times}10^5$ cm^2/Vs. This exceeds the previously values reported on samples with similar electron density n_s by a factor of seven [Das08b].

Prior to the magnetization measurements the sample was illuminated using a blue light emitting diode (LED) following a specific illumination protocol [Das07, Das08b, Das08a]. The protocol includes post illumination annealing to 30 K and a slow cool-down afterwards. In contrast to the protocol our sample was heated during the illumination process due to power dissipation in the LED, reaching the required temperature of 30 K. Thus no heating after the illumination was performed. The band-structure g factor was determined on a reference sample to be $g = 2$ by transport measurements in van-der-Pauw geometry at 300 mK [vK90].

For the magnetization measurements the sample without contacts was placed on a micromechanical cantilever magnetometer (MCM) using a flip-chip technique. The sample was thinned from the backside to about 20 μm thickness in order to reduce the additional weight on the cantilever to a minimum. Still, the weight of the sample leads to

low resonance frequency of the MCM of about 70 Hz.

In the following we distinguish between the fraction of the external magnetic field perpendicular to the sample surface $\mathbf{B}_\perp$, the in-plane fraction $\mathbf{B}_{||}$, and the total field $\mathbf{B}$. In this experiment we intentionally avoided a possible asymmetry induced between the two in-plane valleys due to $\mathbf{B}_\parallel$ by ensuring that $\mathbf{B}_\parallel$ point symmetrically to the principal axes of the conduction-band valleys [Gok08]. This can be seen in fig. 5.1(d)

The measurements were taken in a ^{3}He- cryostat using a micromechanical cantilever magnetometer with a capacitive readout. The MCM is mounted on a swedish rotator which enabled us to rotate the sample with respect to the external magnetic field by up to $\alpha = 90°$. The temperature can be varied from 300 mK up to 30 K.

5.1 Angular dependence

All angular dependent measurements were taken at the nominal base temperature of 300 mK. The extracted oscillatory part of the magnetization is shown in fig 5.1(a) as a function of $B_\perp$. The sawtooth like signal corresponds to the dHvA effect and the sharply dropping slopes coincide with the integer filling factors as noted on the upper-axis in the figure. The data was processed using the method described in chap. 3.1.2. In this work we optimized the polynomial fit that is used to subtract the background for each sweep individually. For all measurements it is between 4th and 6th order. Due to the signal-to-noise ratio of the dHvA oscillations we averaged the data over a field window of 0.01 Tesla.

Fig.5.1(b) shows the evolution of the magnetization over $B_\perp$ for different angles. The magnetization for different angles are offset for clarity. Slight variations in the dHvA oscillations amplitudes for different angles can be observed.

For further investigations we extracted the peak-to-peak oscillation amplitude as indicated in fig. 5.1(c) by the dashed red lines. For filling factor $\nu = 2$ we find $\Delta M_{\nu=2} = 3.6 \times 10^{-14}$ J/T. The peak-to-peak amplitude per electron is $\Delta M_{e,\nu=2} = 0.76\ \mu_B^*$. The spike in fig 5.1(b)

at filling factor $\nu = 1$ is a well known nonequilibrium effect called eddy current. These effects occur when the longitudinal resistivity of a 2DES vanishes due to quantization effects in a continuously ramping magnetic field. Although they are large in comparison with the dHvA effect they do not interfere with our measurements and will not be discussed further. For additional information on eddy currents see [Ush09].

The evolution of the extracted peak-to-peak amplitudes ΔM_ν with the angle is shown in fig 5.2. The value of $\Delta M_{\nu=1}$ (filled squares) increases significantly from $\alpha = 15°$ to $30°$, becoming larger than $\Delta M_{\nu=2}$ (open squares).

The energy gaps $\Delta E_\nu = \Delta M_{e,\nu} B_{\perp,\nu}$ at integer filler factors are depicted in fig. 5.2. In the following they are called thermodynamic energy gaps to distinguish them from energy gaps obtained by excitation spectroscopy where selection rules have to be considered. In this case $B_{\perp,\nu}$ is the magnetic-field position of the corresponding filling factor ν. In contrast to the spectroscopy energy gaps where selection rules such as the generalized Kohn's theorem might obscure electron-electron interaction effects, the amplitude in the dHvA effect reflects all many-body effects. Additionally the dHvA effect monitors the energy gaps in the ground-state electronic spectrum.

In fig. 5.2(b) $\Delta E_{\nu=1}$ is by far the largest and constant after a strong initial increase at small tilt angles. The energy gaps ΔE for $\nu = 2$ to $\nu = 4$ are also shown over a broad angular regime in fig. 5.2. It is unexpected that these gaps are always non zero which means the expected coincidence signature with $\Delta M = 0$ is not observed. Instead small variations in ΔE_ν as a function of the tilt angle are visible in fig. 5.2(b). Local minima are marked by arrows.

The error bar shown in fig. 5.2(a) is due to the reading accuracy of the oscillation amplitudes. The signal-to-noise ratio can not be increased by choosing a wider averaging window because a) the remaining noise has a non-white part and b) excessive averaging smoothes out the steep sawtooth-like dHvA oscillations.

Both of the above findings are in contrast to earlier results from AlAs QW or Si/SiGe QW [Wil05]. We will interpret our findings in terms of interaction effects in the high-mobility 2DES below.

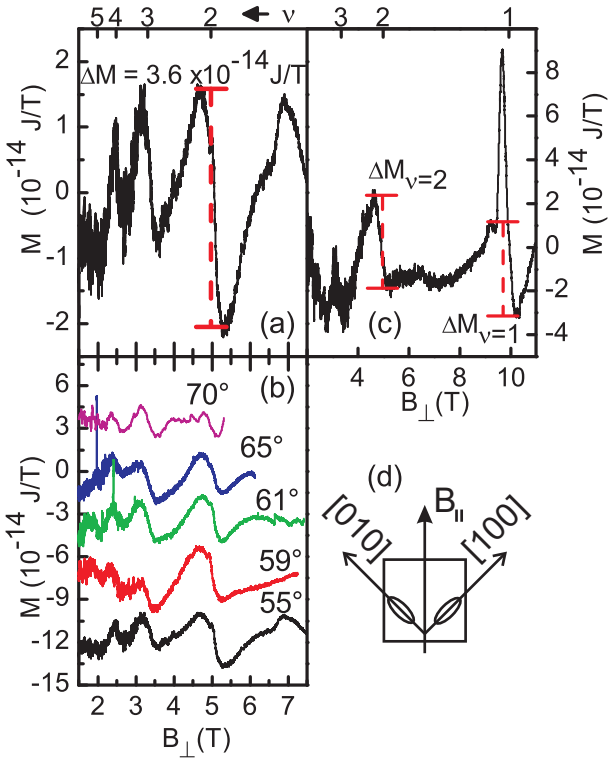

Figure 5.1: (a) Oscillatory part of the magnetic signal at $\alpha = 55°$. The dashed line highlights the peak-to-peak amplitude of the dHVA effect. (c)Magnetization at $\alpha = 40°$. The spike at $\nu = 1$ is due the an eddy current. (b) Further magnetization measurements at different tilt angles α. Curves are offset for clarity. (d) Orientation of $\mathbf{B}_{\parallel}$ with respect to the occupied in-plane valleys.

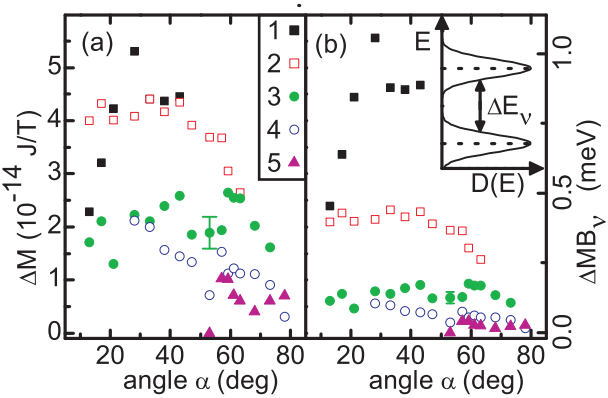

Figure 5.2: (a) Angular dependence of the dHvA amplitudes ΔM_ν for different filling factors ν. $\Delta M_{\nu=1}$ increases by a factor of two between 15° and 30°, whereas ΔM at $\nu = 2$ stays roughly constant. (b) Energy gaps ΔE_ν calculated from the data in (a). The arrows indicates local minima. The inset visualizes that the energy gaps are reduced due to level broadening.

The magnetization amplitude at filling factor 2 is $\Delta M_{\nu=2} = 3.6 \times 210^{-14}$ J/T at $\alpha = 55°$ and therefore one order of magnitude smaller than in Si/SiGe quantum wells [Wil06] which have similar spin and pseudpo-spin degree of freedom but a smaller in-plane effective mass. However, the amplitude per electron $\Delta M_{e,\nu=2} = 0.76\mu_B^*$ is 25% larger than the corresponding value in Si/SiGe. We attribute this to the small broadening of the Landau levels as well as the high quality of the AlAs electron system.

The behavior of filling factor $\nu = 1$ is not consistent with preliminary magnetotransport data taken from an AlAs QW of the same width and density n_s but smaller mobility μ [Pap99]. Those data show a monotonically decreasing of the gap when increasing the angle α from 0° to 50°. We attribute this to the higher mobility of our 2DES which enables a more prominent electron-electron interaction than previously measured.

In the transport data the expected coincidence point is indeed observed as a maximum in the longitudinal resistance R_XX where a minimum is expected. A coincidence, i.e., a vanishing of oscillation amplitudes at a certain tilt angle is also expected in our magnetization measurements. Because our measured data are in strong contrast to this expectation we will discuss this in detail in the following.

5.1.1 Level structure

To discuss the findings of sec. 5.1 we introduce two possible scenarios of the energy level sequence with respect to our findings. For this we assume that the energy gaps are induced by Landau quantization, Zeeman spin splitting, and the lifting of the valley degeneracy in the external magnetic field. In the discussion we will describe the level structure using the Landau level index n, spin index $(\uparrow, \downarrow)$, and valley index $(+, -)$. Since it is not clear, *a priori*, which of the gaps is the largest in a high magnetic field B we discuss two different scenarios where the largest gap is the valley and spin gap, respectively. The energy level sequences are shown in fig. 5.3(a) and (b), respectively. To highlight the evolution of the energy gaps ΔE_ν with the angle α we plot them versus $B/B_\perp = 1/\cos\alpha$.

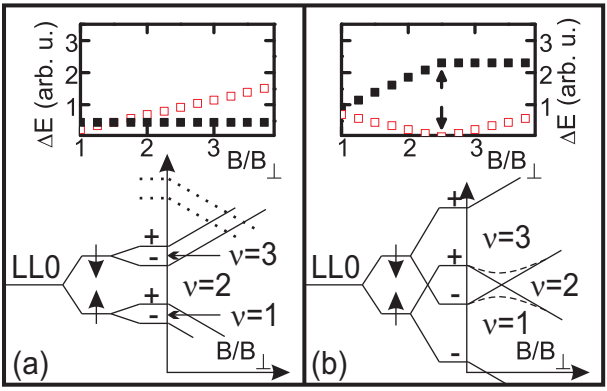

Figure 5.3: Two different scenarios for the splitting of the lowest Landau level (LL0). In both cases the spin quantum number is indicated by $(\uparrow, \downarrow)$ and the valley quantum number is indicated by $(+, -)$: (a) Valley splitting ΔE_V is smaller than spin splitting ΔE_S. The dotted lines are the $\uparrow$-levels of Landau level 1. (b) $\Delta E_V > \Delta E_S$. In both cases the evolution of the energy gaps $\Delta E_\nu = \Delta M_\nu B_{\perp,\nu}$ for $\nu = 1$ and 2 as a function of the angle α is shown in the insets. For the schematics it was assumed that possible exchange enhancement effects are independent of α. Both insets depict the evolution of the energy gaps at filling factor 1 and 2 with the angle corresponding to each scenario.

The spin splitting depends on the total magnetic field B whereas the Landau quantization only depends on the perpendicular component $B_\perp$. Because of this the energetic positions of the energy levels shift with the angle α and the field value B in different ways, depending on their quantum numbers. Energy levels with different spin quantum numbers move in different directions. The valley splitting has also been found to depend linear on $B_\perp$ [Wil05]. Thus energy levels which differ only in their valley quantum numbers are moving parallel with varying angle.

The scenarios depict two very different cases with respect to filling factor $\nu = 1$. In fig. 5.3(a) no level crossing occurs. Due to that the energy gap is expected to stay constant since the two lowest levels move in parallel. For every angle α the gap at $\nu = 1$ is between the energy levels $(0, \uparrow, -)$ and $(0, \uparrow, +)$ which have a different valley but the same spin orientation and therefore are parallel for every angle α. In contrast the energy gap at filling factor $\nu = 2$ would be expected firstly to increase with increasing α as shown in the inset of fig. 5.3(a). After crossing the lowest energy level from Landau level one, indicated by the dotted lines, the gap would stay constant. It changes form a pure spin flip gap where the spin is flipped and the Landau quantum number is changed.

This picture is completely different, if the valley splitting is larger than the spin splitting ($\Delta E_V > \Delta E_S$). In this case the energy gap at filling factor $\nu = 1$ initially increases with increasing α. After a certain point it stays constant. For low angles the gap is between $(0, \uparrow, -)$ and $(0, \downarrow, -)$ whereas at higher angles the $(0, \downarrow, -)$ and the $(0, \uparrow, +)$ levels have crossed. At angles below the crossing point the gap is a pure spin flip gap and later a pure valley flip gap. The gap $\Delta E_{\nu=2}$ is expected to decrease at first reaching $\Delta E_{\nu=2} = 0$ at a specific angle α where the level crossing happens. After this point it increases again.

From the measured dHvA data we suggest a large valley splitting $\Delta E_V > \Delta E_S$ at $\alpha = 0$, in the experiment on the basis of fig. 5.3. The level sequence (b) can especially explain the characteristic increase of $\Delta E_{\nu=1}$ with α, followed by staying constant. For higher filling factors both scenarios predict coincidences, i.e. $\Delta M = 0$, for specific values of α. On the basis of geometrical thoughts the maximum coincidence

angle would be $\alpha = \arccos(gm_c^*/2m_e) = 62°$ if the effective g factor has its bandstructure value.

In our data no $\Delta M = 0$ can be observed for $15° < \alpha < 75°$. This might originate from an effective g-factor in our system that is enhanced by the exchange interaction to a value higher than $g^* = 2$. In this case the coincidence angles are expected to be smaller. For the maximum coincidence angle to be smaller than 15° the condition $g^* \frac{m_c^*}{m_e} = 1,93$ has to be fulfilled. This can not explain the strong increase of filling factor $\nu = 1$. We discuss this in more detail in sec. 5.1.2

The absence of coincidence points could also be explained by strongly coupled energy levels. In this case the energy levels would follow the broken lines in fig. 5.3(b). Consistent with such avoided crossing are slight variations in ΔE which lead to local minima. We indicated points of local minima by arrows in fig. 5.2.

The coupling to higher subbands is unlikely. We showed in sec. 4.1 that the level spacing to the next higher subband in the out-of-plane and in-plane valley was obtained to be 16.4 and 17.5 meV, respectively. The Fermi energy is $E_F = 0.6$ meV. The difference of 15.8 meV is a strong indication that coupling to higher subbands has only minor impact on the level sequence in this case. A coupling to higher subbands would lead to both warping and a smooth decrease of the Landau level energy at large α. This has been discussed in detail for the dHvA effect of a 2DES in Ref. [Wil09]. However, the absence of coincidences and the strong increase of $\Delta E_{\nu=1}$ can not be explained in this scenario. Therefore we exclude coupling to higher subbands from our discussion below.

5.1.2 Energy gap $\Delta E_{\nu=1}$

Because for $\nu = 1$ and small α the Fermi energy is assumed to reside between $(0, \uparrow, -)$ and $(0, \downarrow, -)$ we can calculate the gap due to spin splitting (see chap. 2.1) to be

$$\Delta E_{\nu=1} = \Delta S g \mu_B B + \gamma E_C, \tag{5.1}$$

where $E_C = e^2/4\pi\epsilon\epsilon_0 l_B$ is the Coulomb energy with the magnetic length $l_B^2 = eB_\perp/h$, the dielectric constant ϵ, and the prefactor γ which includes the relevant matrix elements as well as the difference in the population of the spin-up and spin-down levels.

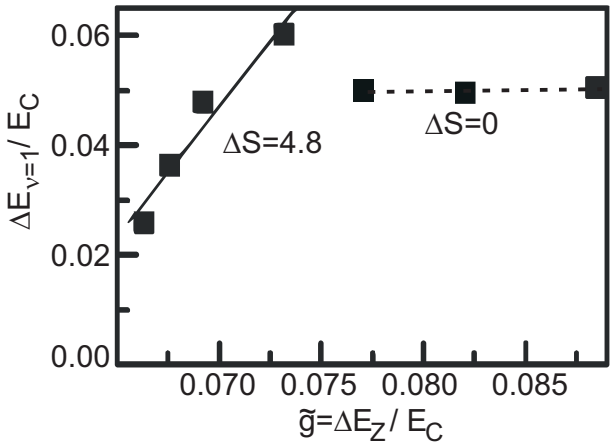

Figure 5.4: Energy gap $\Delta E_{\nu=1}$ (symbols) as a function of the Zeeman energy ΔE_Z both normalized to the Coulomb energy E_C. he steep slope corresponds to the spin-flip number per charge excitation $\Delta S = 4.8 \pm 0.9$ (solid line). At large tilt angle we observe a constant value reflecting $\Delta S = 0 \pm 0.05$.

We used equation 5.1 with ΔS as the fitting parameter. In fig. 5.4 we show the measured energy gap $\Delta E_{\nu=1}$ normalized to the Coulomb energy versus the normalized Zeeman energy $\tilde{g} = g\mu_B B/E_C$ as black squares. Two regimes can be distinguished. At small $\tilde{g}$, i.e. $\alpha < 30°$ a steep slope with $\Delta S = 4.8 \pm 0.9$ can be observed. At larger angles we found $\Delta S = 0 \pm 0.05$. Both values are significantly different form $\Delta S = 1$ which is expected for spin flip excitations of noninteracting electrons with $g = 2$ in a 2DES. Such values of $\Delta S = 1$ were found for comparable two valley systems in Si/SiGe quantum wells at high filling factors[Wil05]. A ΔS significantly larger than one indicates correlated excitation, which were predicted to be the lowest energy excitations at

$\nu = 1$ in single-valley 2DES in GaAs. In this case the physical meaning of ΔS is the so-called skyrmion size, i.e. the number of spins taking part in the excitation.

For the discussion it is necessary to ensure that all the assumptions made are correct. Therefore we discuss the underlying assumptions in detail in the following. The first assumption is that the in-plane magnetic field component only couples through the Zeeman spin splitting. This is strictly valid only for an infinitely thin 2DES. In the experiment the real system exhibits a finite thickness, i.e., the magnetic confinement induced by $B_\parallel$ and the electrostatic confinement of the heterostructure can hybridize. However, the energetic separation between the subbands has been calculated to be large, thus we do not expect a strong effect of this hybridization.

The second assumption is that the prefactor γ depends only on $B_\perp$. It contains matrix elements as well as the relative population difference of the spin-up and spin-down levels, i.e., the degree of spin polarization. At a fixed filling factor, in our case $\nu = 1$, the matrix elements are constant and thus do not vary with $B_\parallel$. The degree of spin polarization at filling factor $\nu = 1$ should be one if the energy levels are well separated because only one energy level is populated.

The spin polarization only varies as a function of $B_\parallel$ if the levels overlap due to disorder induced broadening. Such incomplete spin polarization due to level overlap might lead to a large slope ΔS. However, this mechanism would also lead to even larger slopes at larger spin filling factors because of smaller energy gaps at lower fields. No such slopes are observed in the measured data. Instead fig. 5.1(b) indicates the existence of an eddy current at $\nu = 1$. This feature indicates that the energy levels do not overlap significantly, and thus we assume the spin polarization to be close to one even at small $B_\parallel$. Neither the finite thickness nor level broadening effects contribute in a way which explains the result of $\Delta S = 4.8$.

Instead the experimental results are in agreement with the expected behavior for skyrmionic excitations where $\Delta S = 7$ was found for a single valley 2DES in GaAs and small $\tilde{g}$ [Sch95]. Those skymions are predicted to be extremely sensitive to the electronic structure of the system, and thus the expected range for $\tilde{g}$ in the present system is not

clear. The experimental data are also not explained by quantum Hall valley skyrmions [Shk05]. These were found in an AlAs double valley system at $\nu = 1$. In this experiment the gap $\Delta E_{\nu=1}$ was opened and enlarged due to in-plane strain and did not depend on the angle α.

An other striking feature in the experimental data is the abrupt change from $\Delta S = 4.8$ to $\Delta S = 0$ whereas in [Sch95] a smooth transition to $\Delta S = 1$ was observed. This indicates a change in the underlying electronic structure which could be a change in the nature of the energy gap due to a crossing of energy levels. In scenario (b) for high $B/B_\perp$ filling factor $\nu = 1$ resides between two energy levels with the same spin quantum number but different valley quantum numbers. Therefore spin flips are no longer the lowest lying excitations. This gap does not depend on $B_\parallel$ and thus $\Delta S = 0$ becomes valid. The large value of $\Delta E_{\nu=1} = 0.8$ meV is attributed to exchange enhancement of the valley splitting.

5.1.3 Energy levels at $\nu \geq 2$

The lack of coincidence points for $\nu \geq 2$ could originate from avoided crossings of the involved energy levels. Although single particle effects like spin orbit interaction might lead to avoided crossing of energy levels, those effects are expected to be small in our system. The band gap is large and the band structure g-factor is $g = 2$ similar to a free electron. A many-body effect to couple energy levels strongly would be based on Coulomb interaction. With simulations based on the Hartee-Fock approximation it should be possible to distinguish between direct Coulomb interaction, exchange interaction, and correlation effects. This is beyond the scope of this work. The measurement data suggest avoided crossings to occur not only for $\nu = 2$ but also for higher-indexed Landau levels. This must be considered by a many-body theory for pseudospin systems.

5.2 Temperature dependence

The measurements presented in this section were taken at a fixed angle of $\alpha = 65°$ at different temperatures. The temperature was measured with a calibrated cernox sensor attached to the sample holder. All temperatures were taken prior to the corresponding measurement. The data was handled in the same way as for the angle dependent measurements.

To compare the temperature dependence on different filling factors it is useful to normalize the oscillation amplitudes to their zero temperature saturation value $\Delta M_{\nu,0} = \Delta M_\nu(T = 0)$. In the course of this thesis we improved upon the data analysis used in our group for temperature dependant magnetization measurements. Up to now we associated $\Delta M(T \to 0)$ with the magnetization at base temperature. This is shown in fig. 5.5(b). This is a valid assumption for energy gaps $\Delta E \gg k_B T$. Afterwards a separate Lifshitz-Kosevich fit for every filling factor was obtained. However, this assumption is no longer valid for the energy gaps investigated here. The error of each fit increases strongly with increasing filling factor as can be seen in the fig. 5.5.

Because of the smaller ΔE the method of data analysis by applying the LK fit to the data without normalizing was changed. Form these fits we extracted the $\Delta M \to 0$ which is significantly larger than the measured maximum $\Delta M \to 0.3$ K in fig. 5.5(a). Using this technique the $T \to 0$ value of the oscillation amplitudes is determined. An idealized magnetization curve with these $T \to 0$ values is shown in fig. 5.10(b).

It is important that by this technique we eliminate the influence of the temperature to the oscillation amplitude. However, they are still reduced by the level broadening due to disorder. For filling factor 3 and 4 we determined a $\Delta M(T \to 0) = 3.1 \cdot 10^{-14}$ J/T and $3.4 \cdot 10^{-14}$ J/T for $\nu = 2$. The difference of roughly 10% is within the estimated error of the measurements. In contrast the measured values differ by more than a factor of two, prior to the correction due to the finite temperature.

In fig. 5.6 the data is normalized to the $T \to 0$ values obtained from fig. 5.5(a). For every available filling factor the LK fits reside

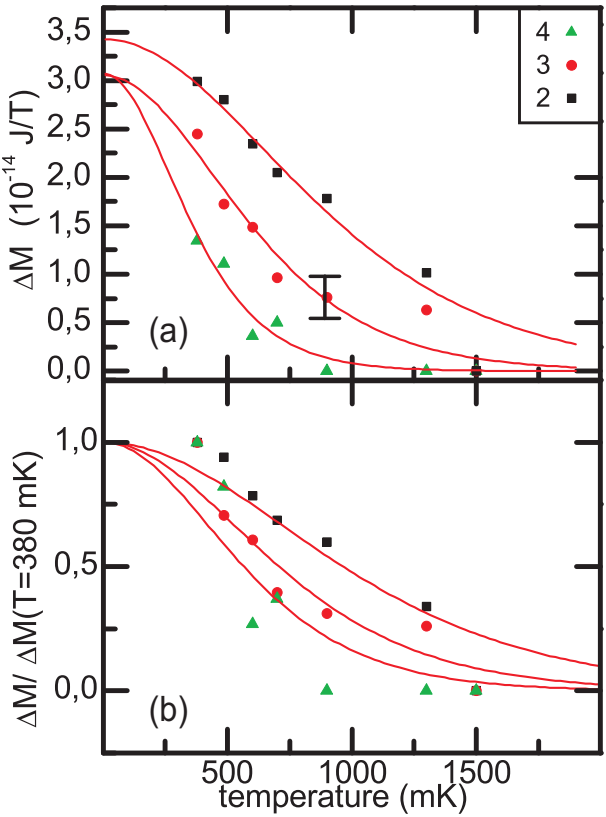

Figure 5.5: (a) Temperature dependence of filling factors $\nu = 2 - 4$ (denoted by numbers). Each filling factor is fitted by a separate Lifshitz-Kosevich fit to determine $\Delta M(T \to 0)$ for every ν. The error bar increases with increasing temperature and filling factor. The error bar for $\nu = 3$ and $T = 0.9$ K is shown exemplarily. (b) Data normalized to their lowest temperature value. Lines show Lifshitz-Kosivich fits for every filling factor.

within the striped area. The upper and lower boundaries of the area are associated with a corresponding energy gap of 0.10 meV/T and 0.18 meV/T, respectively.

It should be noted that the energy gap derived from the Lifshitz-Kosevich fit is not the same as calculated from the oscillation amplitudes. As shown in the inset of fig. 5.2, the energy gap measured via the magnetization amplitude depends on the level broadening whereas the energy gap derived from the Lifshitz-Kosevich fit corresponds to the energetic distance between the centers of the Landau levels denoted by the broken lines in the inset. For further discussion we refer to the energy gap calculated from the Lifshitz-Kosevich fit as LK-gap and to the energy gap calculated from the magnetization oscillations as amplitude gap.

For comparison we plotted the expected single particle temperature dependence for two different energy gaps. Firstly we assume that the valley degeneracy is not lifted and the spin splitting is slightly larger than the Landau gap which is expected for this specific angle. We also assume no enhancement effects to take place and that the splitting is the same for all filling factors. In fig. 5.7(a) this scenario is shown. Energy gaps at filling factor 1 and 3 missing completely. The gap at filling factor 2 is expected to be large. It temperature dependence would follow the broken line in fig. 5.6.

The gap of filling factor 4 is small and it temperature dependence would thus follow the dotted line. Both cases are not consistent with experimental data. Secondly in fig. 5.7(b) we assume the valley splitting to be equal to the Landau level splitting which is reported in recent publications on similar samples [Shk02]. The energy gaps at $\nu = 2$ and $\nu = 3$ are both small and their temperature dependance would follow the dotted line. The energy gap at filling factor 4 is expected to be large and its temperature dependence would thus follow the broken line. In both scenarios at least one gap is expected to be small and therefore exhibits a stronger temperature dependence.

While the LK-gap is the same for all three filling factors the amplitude gap normalized to the corresponding perpendicular magnetic field $B_{\perp,\nu}$ is only for filling factor $\nu = 2$ and 3 almost equal whereas $\nu = 4$ shows only about half the amplitude gap. This can be seen in fig.

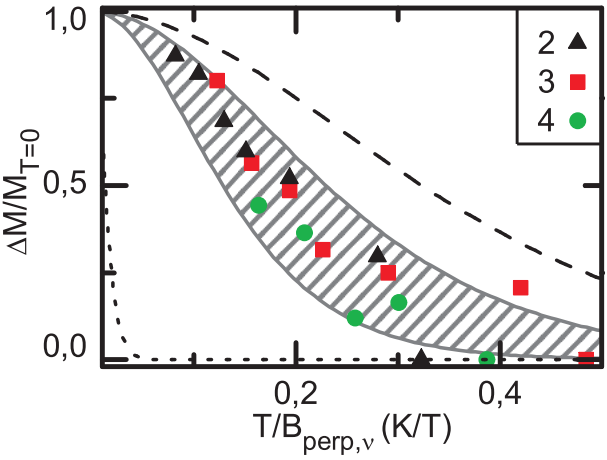

Figure 5.6: Temperature dependence of filling factors $\nu = 2 - 4$ (denoted by numbers). The magnetization amplitudes are normalized to their $T \to 0$ value. The temperature is normalized to the corresponding $B_{\perp,\nu}$ for each ν separately. The grey hatched area is the range of possible Lifshitz-Kosevich fits with a corresponding energy gap ranging from 0.1 meV/T to 0.17 meV/T. The broken and dotted lines indicate expected single particle energy gaps (see text).

5.2(a) because the normalized amplitude energy gap is proportional to the magnetization amplitude ΔM. This effect originates from the fact that filling factor $\nu = 4$ is located at a smaller magnetic field and thus finite temperature has a stronger relative influence on the oscillation amplitude.

5.2.1 Polarization

To discuss our findings in more detail it is instructive to revisit the energy level sequences commonly used and their origin. We start with a single-particle picture which leads to an energy level sequence as shown

in fig. 5.7(a). In the experiment the expected degeneracy of levels with different valley quantum number was shown to be lifted. Thus we have taken into account a valley splitting driven by many-body interactions.

We take the lifting of the valley degeneracy into account by assuming that the valley splitting depends linearly on $B_\perp$ as observed in other experiments[Lay93, Shk02]. This leads to the model we used to explain the angular dependent measurements. The degeneracy is lifted and energy levels which differ only in the valley quantum numbers are moving in parallel with respect to $B_{||}$. Keep in mind that this behavior is a phenomenological observation on different samples. A model by Ando [And82] predicts a $\sqrt{B_\perp}$ dependence.

We further improve our model by incorporating enhancement of spin and valley splitting that includes explicitly corresponding spin- and valley-polarizations. As described in chap. 2.1 the spin and valley splitting is enhanced whenever an occupation imbalance of the corresponding quantum number occurs. We call this dynamic enhancement for further discussion. The expected polarizations for both scenarios are shown in fig. 5.9. Because of the dependence on the actual occupation it is expected that this effect strongly depends on the temperature. Therefore we analyze the influence of the temperature in more detail.

An increase in temperature results in a broadening of the Fermi distribution, and thus in the excitation of some electrons from the highest Landau level occupied at $T \to 0$ to the next higher Landau level. By changing the energy level the electrons change their quantum numbers. If this change includes spin or valley quantum number the corresponding polarization changes as well.

For a qualitative discussion we assume that at higher temperature half of the electrons from the lower level are thermally excited to the higher level. Further we assume no other energy levels are involved in this effect. By this the effect of temperature on the polarization is overestimated but especially for low temperatures the trend is correct. We calculate the spin and valley polarization by just adding up the polarizations of the occupied energy levels. In the high temperature limit both levels involved in the transition are counted as half filled.

In the scenario of small valley splitting the spin polarization for $T \to$

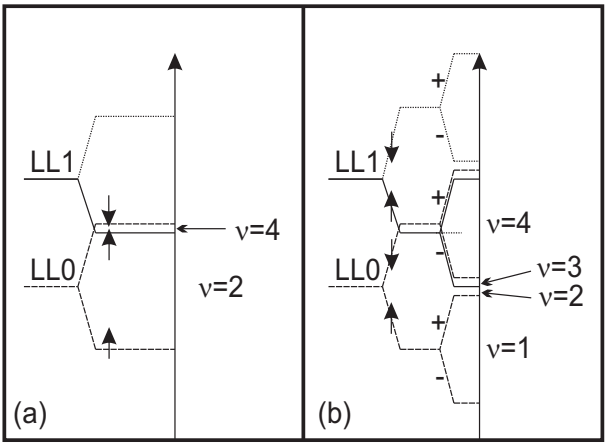

Figure 5.7: Two scenarios for the energy level sequence at $\alpha = 65°$. (a) Spin splitting is larger than Landau level splitting, valley degeneracy is not lifted. (b) Spin splitting is larger than Landau level splitting. Valley spitting equals Landau level splitting.

0 stays at 100% for all filling factors up to 4. The valley polarization goes rapidly down in a zig-zag shape. The maxima are at odd filling factors whereas even filling factors provide zero valley polarization. In the second scenario the polarization is different for filling factor 4. The spin polarization drops down to 50% and at the same time the valley polarization goes up to 50%.

In most cases a finite temperature leads to a reduction of polarization and thus results in a decrease of the enhancement. In the scenarios displayed in fig. 5.7 the polarization of both spin and valley can in some cases increase with increasing temperature. This peculiar effect originates from a crossing of the involved energy levels, and results in an increase of the dynamic enhancement of the corresponding splitting.

But although the enhancement increases the observed energy gap at the Fermi energy still always decreases. This is based on the crossing of the corresponding energy levels and is only valid for the actually observed filling factor. If level crossing occurs the order of the involved energy levels changes. This is the origin for both effects.

We illustrate the counterintuitive effect with a simple example in fig. 5.8. Here the energy gap at filling factor 3 becomes smaller although the spin polarization increases. We assume this can be expanded for multiple level crossings.

For all filling factors that were investigated here the polarizations do not stay constant with increasing temperature in this picture. Thus we would assume a strong temperature dependence as well as a line shape different from the Lifshitz-Kosevich behavior. The model predicts a difference in the temperature dependence of the energy gaps at filling factors 2 to 4, when we take into account whether one or both polarizations change with increasing temperature. At filling factor 4 and 3 both polarizations change significantly.

At filling factor 2 only the valley polarization changes with increasing temperature. Additionally at filling factor 2 the increase in the valley polarization is most over estimated by this simple model. The valley splitting is expected to be very small in the case of zero valley polarization. Therefore, electrons are thermally excited from nearly degenerate energy levels, with respect to valley quantum number, to

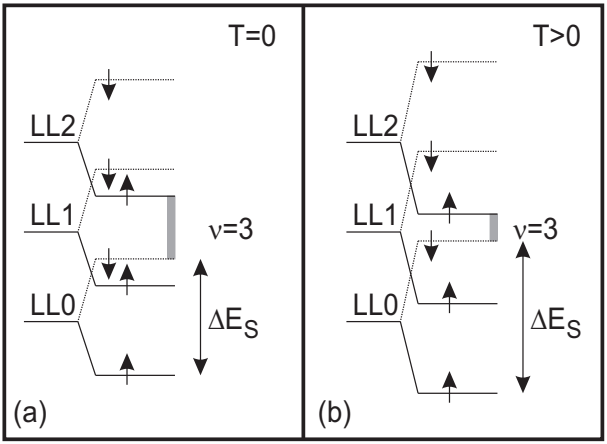

Figure 5.8: Two scenarios of an energy level sequence at different temperatures. (a) At filling factor 3 the spin polarization is 1/3 at $T = 0$. The spin splitting is enhanced and the energy gap at filling factor 3 is large. (b) With increasing temperature the spin polarization increases if electrons are excited over the grey area. Although the spin splitting is even more enhanced than in (a) the energy gap a filling factor 3 is smaller.

another set of nearly degenerate energy levels. In this case the approximation of only the two energy levels next to the Fermi energy taking part in the thermal activation is not a good assumption. In this case we expect only a very small or no valley polarization due to an increase in temperature.

We therefore expect from the model at least filling factor 2 should show a significantly weaker temperature dependence as well as a larger energy gap than we have measured. Especially it should be larger than the values for filling factor 3 and 4. Both higher filling factors should depend strongly on polarization enhancement and therefore should exhibit a strong temperature dependence.

The Lifshitz-Kosevich approximation for the temperature dependence of dHvA amplitudes is *a priori* only valid for energy gaps that are not dynamically enhanced by electron-electron interaction effects. Therefore it is not expected to be valid for all investigated filling factors, which at least partly consist of enhanced valley and/or spin gaps. Single particle energy spectra are not consistent with our measured data as shown in fig. 5.6. Even static enhancement leads to energy gaps different than those derived from our measurements. Nevertheless, the shape of the measured temperature dependence shows no significant deviation from a Lifshitz-Kosevich form. Thus we use Lifshitz-Kosevich fits to the experimental data for further discussion.

5.2.2 Level sequence at $\alpha = 65°$

An idealized magnetization curve for $T \to 0$ and $\alpha = 65°$ is shown in fig. 5.10(b). The displayed oscillation amplitudes are the zero temperature values extracted using LK fits to the experimental data. For every filling factor an energy level sequence is shown which would lead to the measured amplitude. Because all splittings are assumed to depend linearly on the external magnetic field the level spacing increase at smaller filling factors.

To reproduce the experimental energy gaps we have to assume different spin splittings and valley splittings for every filling factor. We assume that the Landau level depend linearly on $B_\perp$. This implies that

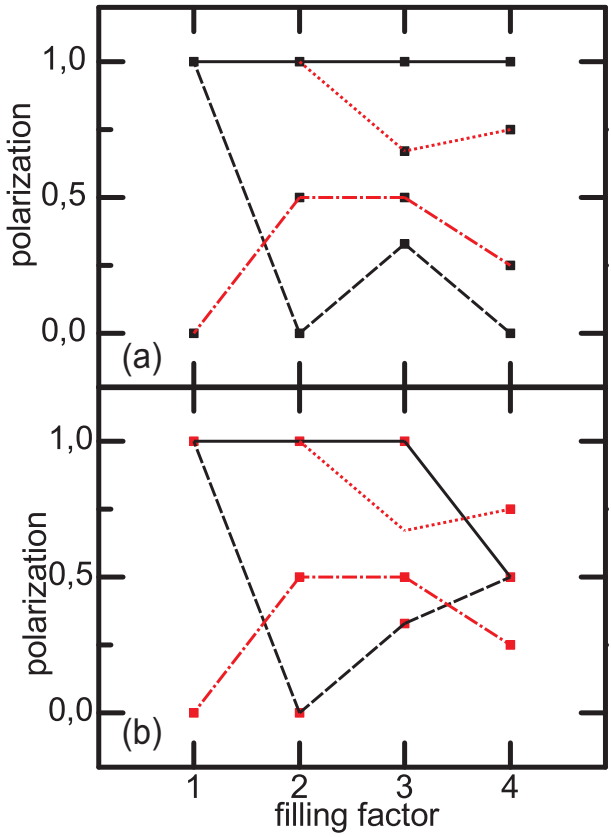

Figure 5.9: Spin polarization (solid line) and valley polarization (broken line) for the corresponding scenario in fig. 5.7. The red lines show the estimated change with increasing temperature.

the effective mass is constant. At filling factor 2 the valley splitting is about half of Landau level splitting. The spin splitting is larger than the Landau splitting due to the high angle of 65°. The actual value of the spin splitting would not influence the value of the energy gap at filling factor 2 in a picture where the size of the spin splitting does not depend on the Landau level index.

At this point it is necessary to give a plausible argument why the valley splitting is assumed to be smaller than the Landau level splitting. Because filling factor 2 could be of the same size with an even larger valley and spin splitting. In this case the energy levels forming filling factor 2 would cross. With such a large valley splitting filling factor 1 is at least as large as a Landau gap. Even though we did not measure filling factor 1 at 65° we expect filling factor 1 not to change its nature between $\alpha = 45°$ and 65°. At 45° filling factor 1 is about half of the Landau splitting, thus we expected it to be a valley gap as discussed in sec. 5.1.1 above. Since we expect the valley splitting in the quantum limes to be roughly half of the Landau splitting we assume that it is not larger at higher filling factors.

At filling factor 3 the spin splitting has to be even larger. The valley splitting is again about half of the Landau level splitting. Again the actual value of the spin spitting would not influence the measurement. Filling factor 4 includes a large valley splitting and also a large spin splitting. The presented level sequences explain the measured data. But they are not consistent with the expected behavior of splittings due to external field and polarizations.

For comparison in part (a) of the fig. 5.10 the expected level sequences are shown. These are based on the model described earlier including single-particle energies, $B_\perp$-dependent lifting of the valley degeneracy as well as an enhancement due to spin and valley polarization. Especially we would expect the valley splitting to depend mostly on the dynamic enhancement due to occupation imbalance. This is in contrast to the level sequences in fig. 5.10(b) which model the gaps observed in the experiment.

One possible explanation for the experimental observations could be an additional interaction effect. In the discussion of the angular dependence of the energy gaps in sec. 5.1 we already proposed an anti-

crossing of energy levels as a possible reason for the observed absence of field induced level coincidences. Such an effect based on strong interaction of the electrons in different levels could lead to a modification of the energy level sequence. A strong repulsion of adjacent energy levels could lead to roughly equally spaced levels, with exemption of the lowest energy gap.

This has to example been predicted for energy levels coupled by the Rashba spin-orbit interaction in tilted magnetic field in Ref. [Byc84]. In AlAs, however, the spin-orbit interaction is expected to be small and the corresponding mechanism that could lead to a strong anti-crossing effect is not jet clear.

If the repulsion dominates the energy level sequence the temperature dependence of all energy gaps would be influenced as well. Due to a renormalization at every temperature a stronger dependence could be suppressed. This would lead to a more or less equal temperature dependence of all filling factors regardless of polarization based enhancement effects of some energy gaps. It would also lead to avoided crossings and therefore to a absence of coincidence points.

5.3 Conclusion

Based on our experimental data we suggest a system of strongly interacting electrons. We found multiple experimental indications for a large valley splitting which is not expected for non-interacting electrons. Even commonly used phenomenological formulas for valley splitting like linear on $B_\perp$ dependent lifting of the valley degeneracy do not fit to our measurements. We conclude that additional interaction effects are necessary to explain our experimental data.

The energy gap of filling factor 1 shows a strong increase with increasing tilt angle α. After a certain angle it stay constant. This could be explained by a strong valley splitting on the order of the Landau level splitting. This leads to a change in the nature of the energy gap that is observed by the abrupt change from a steep increase to a constant value.

The energy levels around higher filling factors show no coincidence points and not the expected behavior with the tilt angle. Instead they show no angular dependence except for some slight variations at specific angles. The observed behavior can be explained by assumed avoided crossings.

The temperature dependence does not show the characteristic of dynamically enhanced energy gaps. Instead, surprisingly, all observed gaps follow roughly a Lifshitz-Kosevich shape. The difference in the value of the energy gaps is much lower than expected even if dynamic enhancement is taken into account. Although is is not clear exactly which value for each energy gap is expected our model still suggests at least one larger and one smaller gap.

We conclude that additional electron-electron interaction effects alter the underlying electronic structure of our sample fundamentally. A repulsion of the energy levels could explain the unexpected behavior we found in different measurements. It could lead to avoided crossings and change the temperature dependence.

Further measurements on this system should investigate the temperature dependence of different filling factors specially filling factor 1. We expect filling factor 1 to exhibit a completely different temperature dependence below and above $\alpha = 30°$ due to the different nature of the gap. Investigations of higher filling factors are necessary to confirm our assumption of a repulsion of energy levels.

The temperature dependence revealed that lower temperatures are necessary to avoid the need of excessive temperature dependent measurements to gain significant insight from the data. This should be considered for further measurements.

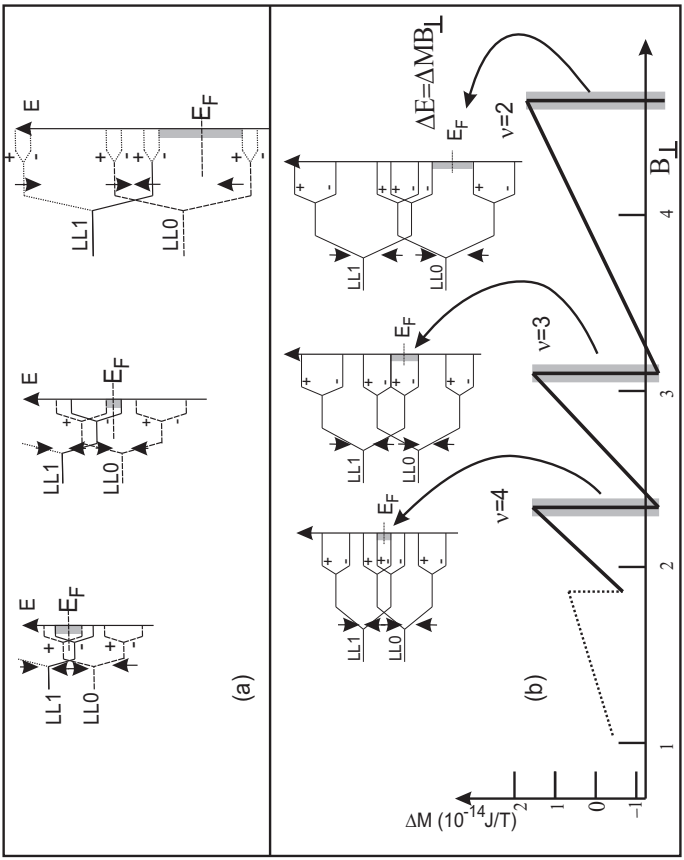

Figure 5.10: (a) Possible scenarios for the energy level sequences at $\nu = 2, 3$ and 4. At each filling factor an enhanced splitting is assumed dependent on the corresponding spin and valley polarizations. (b) The ideal magnetization curve is shown and the correspondence between $\Delta E = \Delta M B_\perp$ is highlighted by gray areas. For each oscillation amplitude a possible corresponding energy level sequence in shown. Especially at filling factor 2 both presented energy level sequences diverge significantly.

Chapter 6

Properties of nanomechanical bridges

The data presented in this chapter are divided in two main sections. In both sections we investigate the properties of nanomechanical bridges in the inner conductor of a coplanar waveguide (CPW)structure. We focus on the magnetic and mechanical properties of the bridge as well as a possible coupling between both properties.

In sec. 6.1 the electro-magnetic wave response of the structure to voltage step pulses is shown. We use a Time Domain Reflectometer (TDR) to measure the reflected voltage signal as well as the part transmitted through the structure. Due to the steep slope of the step pulse a broad frequency spectrum can be excited at once by this technique. The high frequencies up to 30 GHz can excite ferromagnetic resonances (FMR) in an included ferromagnetic cobalt (Co) layer. Another important possibility of the technique is that we can investigate the microwave impedance of the device with spatial resolution.

The second measurement technique is performed on the same samples but with a vector network analyzer (VNA). Data are shown in sec. 6.2. Continuous wave excitation is performed with stepwise increasing frequency between 10 MHz and 26.5 GHz. Spectra are taken for differ-

ent external magnetic fields. Additionally to the magnet field sweeps we also performed power dependent measurements. In each case we gathered the reflection and transmission coefficients. This technique enables us to gain significant insight in the mechanic and magnetic properties of the investigated structures at high frequencies. We can measure if energy is transferred to mechanical or magnetic oscillations regardless of the origin of the oscillations as long as there is a coupling mechanism to the electro-magnetic wave.

All samples consist of a GaAs substrate covered with a Co layer which is between 14 and 21 nm thick. On top is a CPW fabricated from 4.5 nm thick chromium followed by 100 nm thick silver and a 21 nm thick gold cap. All metal layers have been deposited with an e-beam evaporator. The nanomechanical bridges were fabricated by focused ion beam preparation. For details on this process see chap. 4.2. All CPWs had an inner conductor width of 2 μm at a length of 400 μm. The magnetically active Co-layer had an area of 300×120 μm^2. The nanomechanical bridges had typically a length of 2 μm and a width of 120 nm.

6.1 TDR measurements

We took the measurements presented in this section using a digital sampling oscilloscope (DSO) with a TDR module. A 500 mV step pulse is applied by the module. The pulse has a rise time of 11.7 picoseconds. Most measurements were taken at room temperature and at zero external magnetic field. We measured on three different types of sample.

In the following we refer to the CPW with a freestanding nanomechanical bridge in the signal line as sample 1. In addition we made measurements on CPWs with deep-submicron wide inner conductors. For these samples we stopped the preparation process after the deep etching step. We refer to all of them as sample 2. The inner conductor is already narrowed but we have no free standing bridge because the inner conductor is still connected to the substrate. We also made measurements on CPWs with a 2 μm wide inner conductor prior to

nanofabrication. These types of samples are referred to as sample 3.

sample 1	fully processed freestanding bridge
sample 2	only inner conductor narrowed
sample 3	CPW without nanobridge

To separate the signal of the CPW from the signal of the feed line, we measured the reflection of the feed line with and without contact to our sample. The dotted (red) line in fig. 6.1 shows time dependent voltage signal of the feed line without contact to the CPW over the time. The strong increase indicates reflection of the voltage step at the the end of the feed line. The continuous (black) curve is measured with the same set up where the feed line is connected to a CPW. Instead of the strong increase a dip can be observed. After the dip the resistance increases again.

We transform the length of the CPW to a time scale using the running speed of the voltage step pulse within our sample. This yields

$$\Delta t = \frac{\Delta s}{c \cdot n_{eff}} \sim 0.01 \cdot 10^{-9}\text{sec}, \tag{6.1}$$

with the CPW lengh $s = 400\ \mu$m, the speed of light c, and the effective refractive index $n_{eff} = 13/2$ as the microwave resides at the interface between vacuum (air) and GaAs. Δs can be inferred from fig. 6.1 the runtime of the pulse on the CPW corresponds to the initial negative slope of the dip.

In this sections we compare measurements on the different samples 1-3. In fig. 6.2 time-dependent voltage traces are shown of different CPWs. We limit the time scale to the relevant part of the dip. The strongest and the weakest dip (solid lines) are two different samples of type 3. The dotted line is a measurement on a sample of type 1.

The depth of the dip goes down to 24 Ω which is in the middle between the two CPWs of sample type 3. Two curves of CPWs of sample type 2 (dashed lines) are also shown in this figure. These dips go down to 21 Ω and 24.5 Ω, respectively. This is in the middle between the both sample of type 3. The slope after the dip is steeper for the sample type 3. But there is a significant variance between CPWs that were equally processed. All the sample type 3 exhibit a stronger increase than any

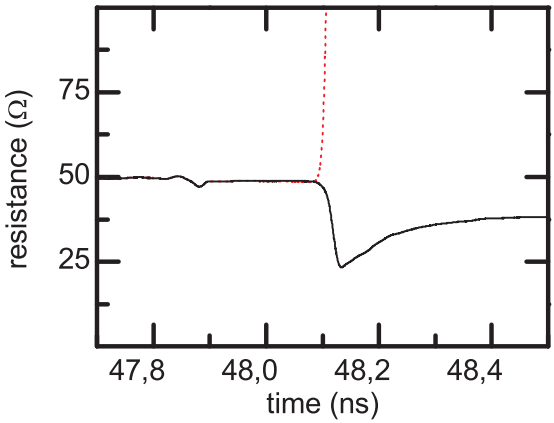

Figure 6.1: Time Domain Reflectometry of CPW (solid black) and without CPW (dotted red). After a run time of 48.1 ns the step pulse reaches the the connection point of the feed line and the CPW.

of the other sample types. The sample type 2 show one steeper slope and one less steep slope if compared to the sample type 1.

The transmission of the voltage pulse through the CPWs is shown in fig. 6.3. The horizontal solid line near to zero shows a measurement without connected feed line. As expected it stays close to zero. However, around 48,1 ns a small peak can be observed. At the same time all of the connected measurements show a similar but larger peak.

Sample 3 (dotted line) shows a roughly linear voltage increase with slight variations around 48.2 ns. Sample 1 and 2 show a much steeper increase.

We performed TDR measurements at liquid helium temperature. Using a superconducting coil a perpendicular magnetic field up to 2.5 T was applied. The sample was located above the coil and positioned slightly off the magnet axis which led to a slightly miss-aligned magnetic field.

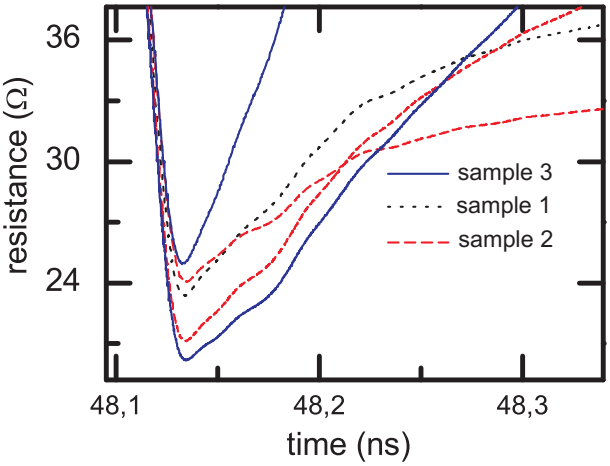

Figure 6.2: Reflection data of several CPWs. Comparison of sample 1 (dotted line) with sample 3 (solid line) and sample 2 (dashed line). All measurements were taken at room temperature and zero external magnetic field.

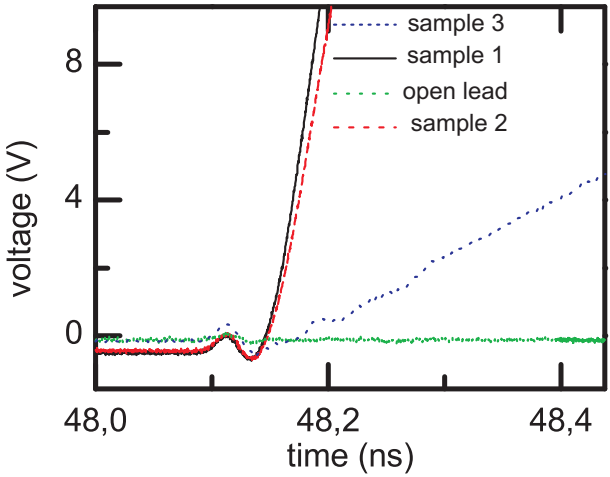

Figure 6.3: Transmission data of several CPWs. Sample 1 (dotted line), sample 3 (solid line) and sample 2 (dashed line). For Comparison a measurement with open lead is shown (solid horizontal line near zero). All measurements were taken at room temperature and zero external magnetic field.

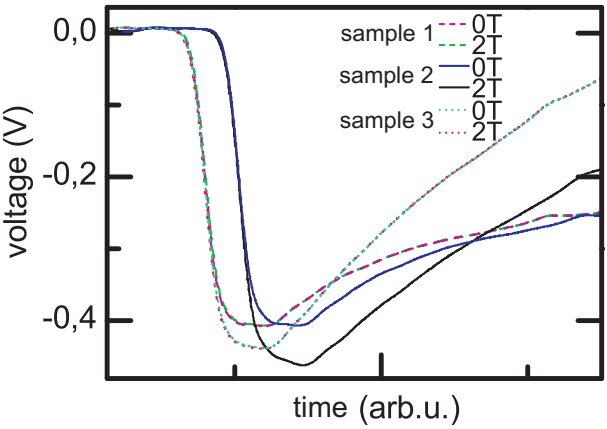

Figure 6.4: Reflection measurements on different CPWs. All measurements were taken in a liquid He-cryostat at 4.2 K. For each CPW measurements were taken at 0 T and 2 T perpendicular external magnetic field. For comparison all three sample types of CPWs are shown.

Measurements on the same samples were performed at 0 T and at 2 T. All measurements at a single magnetic field value were performed in one sequence by *in-situ* changing the contacted CPW. Thus the measurements on the same CPW but different magnetic fields were performed after remaking the contacts to the CPW. We show measurements on three different samples at different magnetic fields in fig. 6.4. The traces for different magnetic fields of sample 1 and 3 are almost identical. Instead for sample 2 the depth of the dip as well as the consecutive increase are different.

6.1.1 Microwave conductance

Following fig. 6.2 the depth of the dip can not be attributed to the preparation process of a nanobridge.

Sample 3 shows the deepest and the flatest dip whereas all CPWs of type 1 and 2 reside in between. In contrast the increase after the dip is steeper for both CPWs of type 3 and reach a saturation value (not shown). A steeper slope indicates that the microwave has less resistance while running through the processed CPWs.

This is also extracted from the transmission signals in fig. 6.3. In this figure the transmitted voltage is shown and thus a steeper slope indicates that the microwave has less resistance while traveling through.

The transmission signal has a single small peak at 48.1 ns even if the probe tip is not connected to a CPW and is thus isolated from the port used for measurements. We attribute this peak to electromagnetic crosstalk. Some parts of the entering rf wave are transmitted to the vacuum and picked up by the CPW and the second probe tip, respectively. The crosstalk is more intense if the probe tip is connected to the CPW because the distance between both probe tips is smaller in this case. The peak can clearly be distinguished from other signals and has no influence on our measurements.

To extract the signal of the nanomechanical bridge we subtracted a reflection trace of sample 3 from the data of sample 1 and another CPW of type 3, respectively. Both data are shown in fig. 6.5. The difference in the shape originates from different CPWs being measured. Apparently, both show a significant increase in the noise level in a range we attribute to the CPW. Because both curves show the same signature it is not dependent on the nanomechanical bridge.

The difference of the same CPW at 0 T and 2 T is shown in fig. 6.4. To extract the effects of the external magnetic field on the nanomechanical bridge we subtracted the trace at 0 T from the trace at 2 T and compare an sample type 3 with sample 1. The results are shown in fig. 6.6.

The trace we subtracted is shown as a dotted line to give a feeling of the scales. Both show the same signature in the time regime we associate with the CPW itself. Except that a minor offset after the CPW both curves show the same characteristics. Therefore none of the visible signatures originates from the nanomechanical bridge.

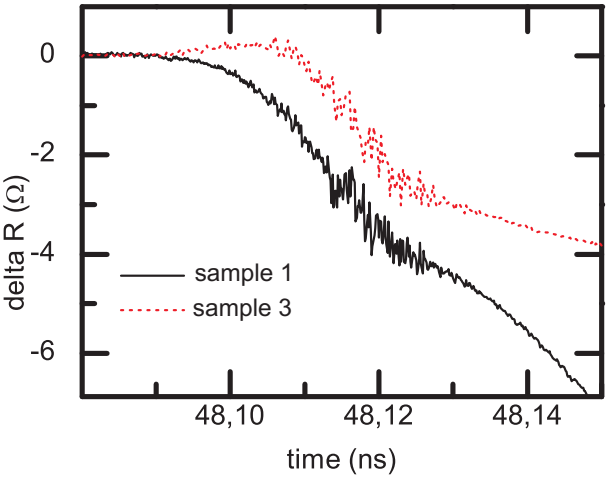

Figure 6.5: Difference of reflection measurements on sample 3 and sample 1 type CPWs (different CPWs). The noise increases within runtime regime that corresponds to the CPW.

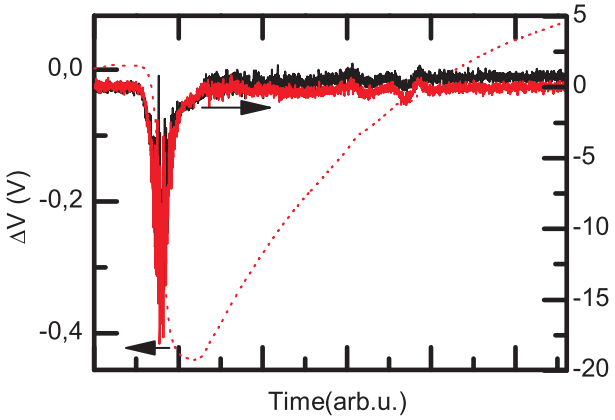

Figure 6.6: Measurement on CPWs with nanomechanical bridge at 0 T (solid black) and 2 T (dashed red). The reference measurement we subtracted from both curves is shown (dotted line).

6.1.2 Discussion

Fig. 6.2 shows that reflection signals strongly depend on the microscopic structure of the CPW as well as the quality of the connection between the feed line and the CPW which can change for each measurement.

The difference in the traces of different CPWs originates from two main sources. First, and most important is the microscopic roughness of the CPW. This can be observed form the various measurements on different CPWs. Each of this shows a different depth of the dip whereas the slope of the increase afterwards only sightly varies between the different CPWs of type 3.

The second is the connection between the CPW and the feed line. As described in chap. 3.2 the connection is made by pressing GHz optimized probe tips to the CPW. This technique does not always lead to connections of equal quality. Especially connecting the same CPW multiple time leads to a decrease in the connection quality.

In fig. 6.4 the difference in the connection quality can clearly be observed. Two of three different CPWs show the same trace for both connections. The last CPW shows a clear difference between the two connections. We attribute this to an unreproducible connection process.

Besides the difference of the connection process which is in the same range as the difference based on the microscopic structure of the CPW no conceptual change can be observed based on the process of the nanobridge preparation. Sample 1 and 2 are both in the same range. This can also be observed from fig. 6.5. Again no specific difference can be observed between sample 3 and sample 1.

We conclude that nanobridge processing does not significantly reduce the ability of CPWs to conduct microwaves. The variations in the reflection signal indicates that no significant amount of the step pulse is additionally reflected after we processed the nanobridge to the inner conductor. Unexpectedly our measurements show that the voltage step pulse runs through the CPW more easily after a preparation process. We, therefore, expect no difficulties with rf-excitations of nanomechanical structures within the frameset of CPWs currently used in our group.

The high perpendicular magnetic field provides a mechanism for coupling to the mechanical motion of the bridge. The current corresponding to the voltage pulse is subject to the Lorentz force due to the external magnetic field.

Although the theoretically reachable current is in the same range for TDR as well as VNA measurements we do not observe any oscillations in the TDR signals. We attribute this to the non-continuous excitation of the TDR measurements. The mechanical oscillations of the bridge would have a period much longer than the presented measurement data. But even with much longer measuring times no oscillation signature of the nanomechanical bridge was observed.

We also do not observe changes of the impedance due to high external magnetic field acting on the nanobridge. The bridges do neither show a significant signal in reflection nor in transmission. The difference method reveals an increased noise level within the range of the CPW but this does not depend on the nanobridge. It shows up also

for unprocessed CPWs.

6.2 VNA measurements

The measurements in this section were taken with a vector network analyzer (VNA) in a liquid helium cryostat at 4.2 K. The external magnetic field is perpendicular to the sample surface but with a slight misalignment because the sample is positioned slightly off the magnet axis and a few centimeters above the superconducting coil.

The VNA applies a continuous electronmagnetic wave with a frequency between 10 MHz and 26.5 GHz. The excitation power is 10 dBm unless otherwise stated. The VNA determines the scattering parameters S11, S12, S21, and S22 as described in chap. 3.2. To extract the part of the signal that depends on the magnetic field from the background we subtract a reference dataset from each frequency spectrum. We use a calibrated measurement method which means that the influence of feed lines and connectors are already calculated out by the VNA itself. The samples we used are similar to the ones we used for the TDR measurements.

With the known excitation power P and the impedance Z of the feed line we calculate the maximaum current running through the CPW in one half cycle to

$$I_{VNA,max} = \sqrt{\frac{P}{Z}} = 14\text{mA}. \tag{6.2}$$

This is in the same range as the current during the TDR measurements. However, the TDR applies only a step pulse whereas the VNA applies a continuous microwave signal through the structure. This leads to resonant excitations.

6.2.1 Magnet field sweeps

In fig. 6.7 we show a typical frequency spectra as a function of the external magnetic field of a nanomechanical bridge comparable with

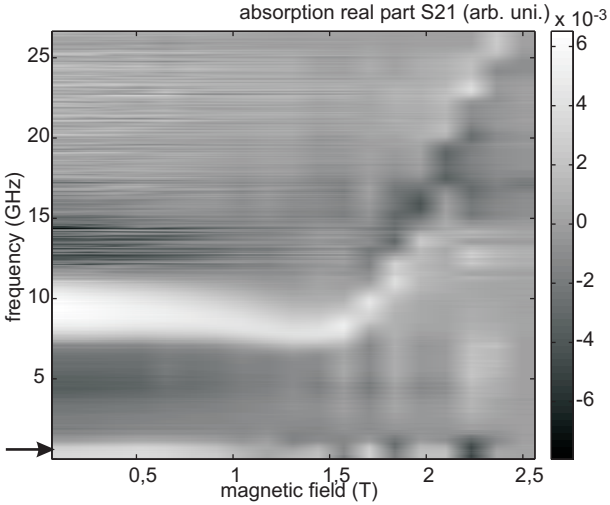

Figure 6.7: S21 frequency spectra of CPW with a nanomechanical bridge versus perpendicular magnetic field. The typical FMR signature of the Co layer can be observed. In addition a signature at the lower boundary of the frequency range is visible.

sample 1. At 0 T and around 10 GHz the FMR of the Co-layer can be observed. The FMR frequency slightly decreases from 0 T to 1.5 T and than increases with a steep slope. At the strongly increasing branch the contrast changes from a pure white (positive) to an interchanging black and white contrast. For high magnetic fields ($B > 2$ T) a weak second branch at lower frequencies is observed.

At the lower end of the frequency spectra an additional resonance like signature is observed. It does not shift in frequency over the whole magnetic field range. It becomes lower in intensity and almost vanishes at 1.5 T. In the range above 1.5. T the contrast changes from black to white several times.

In fig. 6.8 the real and imaginary part of the S21 spectrum at 0.25 T is shown. The FMR of the Co-layer can clearly be observed in both

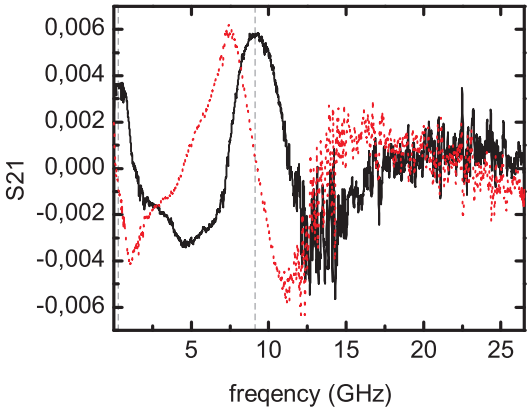

Figure 6.8: Real (black solid line) and imaginary (dotted red line) part of a spectrum at 0.25 T. At 0.5 GHz and 10 GHz two qualitatively similar resonances are observable. The vertical dashed lines indicate the peak positions in the real part and the zero crossing in the imaginary part.

curves indicated by the vertical dashed line at 9 GHz. In addition at 530 MHz a peak in the real part with a height compared to roughly half of the FRM can be observed also indicated by a vertical dashed line. The lower end of this peak is outside the available frequency range of the VNA.

The peak in the real part corresponds to a peak followed by a dip in the imaginary part. The peak position in the real part is equal to the zero-crossing in the imaginary part which can clearly be seen in fig. 6.8 for the FMR. This is the FMR signal expected from the theory discussed in chap. 2.2.

Qualitatively the same signature occurs at 530 MHz. The real part exhibits a peak and the imaginary part shows a dip on the high frequency side. The zero-crossing corresponds to the peak position. However, the low frequency side peak in the imaginary part is not observed due to the cutoff of the frequency measurement at $f = 10$ MHz.

In fig. 6.9 (a) the evolution of the peak height in the real part at 530 MHz with respect to the external magnetic field is shown. Starting from zero magnetic field the intensity decreases and crosses zero at 1.1 T. For higher fields it increases again but some points in between are negative. In fig. 6.9(b) we show the full B-field sweep again for reference. In the range above 1.3 T significatively more noise than in the lower regime can be observed. Especially at some particular field values indicated by arrows a contrast change take place. We, therefore, focus our analysis on the range below 1.5 T and neglect the hatched grey area in further discussions.

The behavior of the Co FMR in fig. 6.7 is as expected, although the FMR line width is quite high. For a homogeneous plain film the theoretical FMR is expected to go down to zero frequency with increasing external field. This is not the case in our measurements. We attribute this to surface roughness of the Co-layer and a not perfectly perpendicular external magnetic field.

Resonance at 500 MHz

From our measurements and the analysis of the real- and imaginary parts we assume that the signature at 530 MHz is an additional resonance. The peak height is half of the FMR peak and real as well as imaginary part show the same characteristics as for the FMR. By comparing both resonances we identify the resonance at 530 MHz to be an absorption. The peak at 530 MHz has the same sign as the FMR and thus both correspond to absorbtion of microwave power.

FMR is expected to show a significant dependence on the external magnetic field. This is the case for the Co FMR. In strong contrast the resonance at 530 Mhz does not shift in frequency over the whole magnetic field range. However, it does vary significantly in intensity.

To ensure that the resonance at 530 MHz is not an artifact of the measurement setup we show additionally the S22 parameter in fig.6.10. An actual resonance should show up in all S-parameters. In both parts the same signatures can clearly be observed at 10 GHz as well as at 530 MHz. Although the background on the signal makes a quantitative

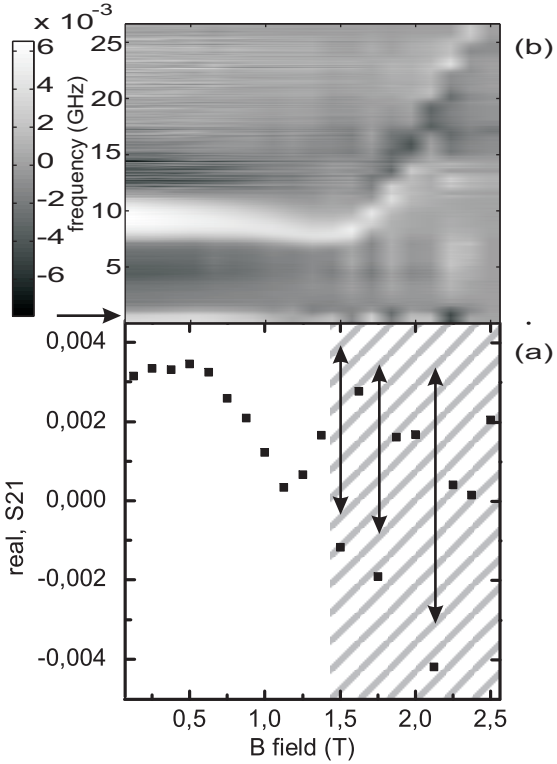

Figure 6.9: (a) Peak height of the resonance peak a 530 MHz for different external magnetic fields. (b) For reference the same fig. as 6.7. At some values of the external field the measurements show extraordinary high noise leading to negative values of the peak hight. The field values are marked by arrows.

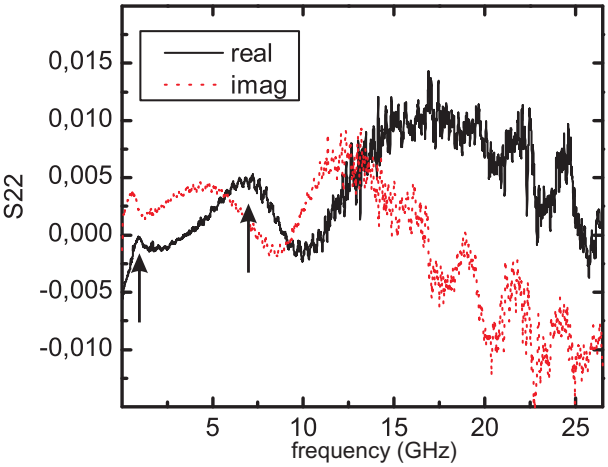

Figure 6.10: Real (solid) and imaginary (dotted) part of S22 (reflection). At 0.5 and 10 GHz a similar resonance structure can be observed. Peaks in the real part are marked by arrows.

analysis difficult the similarity is easy to recognize.

6.2.2 Power dependent measurements

In the literature a well established method to identify mechanical resonance is to increase the excitation power because for high power excitations the mechanical oscillations exhibit the characteristic frequency dependence of a Duffing oscillator as described in chap 2.3. While an increase of the excitation power is often done by increasing the external magnetic field to provide a higher Lorentz force to the nanomechanical device [Hua05] we are varying the excitation power of the VNA [XLF07] and therefore the voltage and current running through our nanomechanical device. We did measurements starting at -24 dBm up to +12 dBm. A constant perpendicular external magnetic field of $B = 2$ T was applied and the measurements were performed at 4.2 K.

To extract phenomena that depend on the excitation power we subtracted the spectrum with minimum power from each measurement. The obtained data are shown in fig. 6.11(a). With increasing power the relative absorption increases indicated by lower values. The absorption change is not constant over the whole frequency range but oscillates. Each subsequent measurement is offset for clarity.

We firstly focus on the evolution of both resonances that we observed in the B-field sweeps in fig.6.7. At an external field of $B = 2$ T the resonances are located at ~ 20 GHz and 0.5 GHz. A magnification of the area round 20 GHz is shown in fig. 6.11(b). The vertical dashed line indicates the position of the FMR. Apart from the patterned overall evolution of the spectrum we observe no deviation in the higher power spectra that we attribute to a change in the resonance structure of the FMR.

In fig. 6.11(c) a magnification of the area around 500 MHz is shown. In this case the vertical dashed lines highlight the position of the minimum and maximum adjacent to the observed resonance at 530 MHz. For the highest power spectrum a shift of the maximum at 630 MHz towards lower frequencies can be observed. This is highlighted by a circle. In contrast the minimum at 420 MHz does not shift.

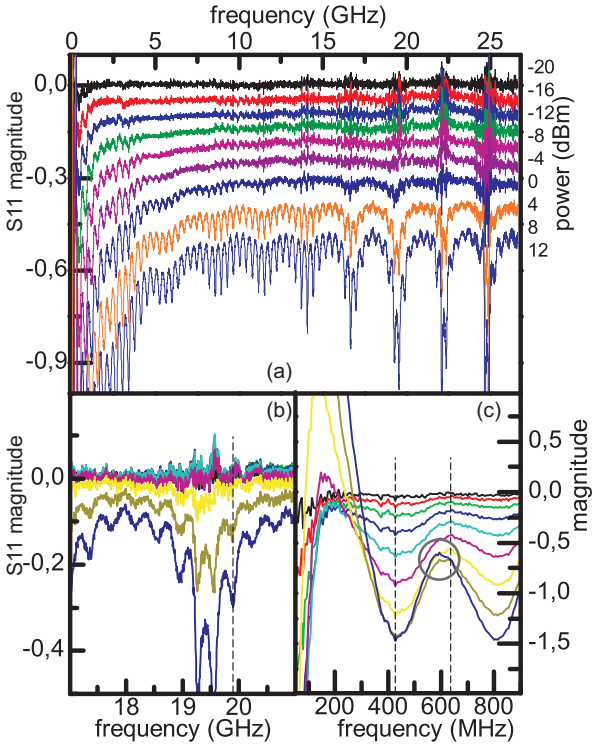

Figure 6.11: (a) Magnitude of S11 in logarithmic scale measured on a CPW with nanomechanical bridge at different excitation powers from -20 dBm up to +12 dBm. From each spectrum we subtracted a reference spectrum at -24 dBm. Each subsequent curve is offset by -0.05 for better visibility. (b) Detail of (a) around 20 GHz without the curves being offset. The vertical dashed line indicates the position of the FMR of the Co layer. (c) Detail of (a) around 500 MHz without the curves being offset The vertical dashed lines mark the extremal points adjacent to the second resonance. A shift of the maximum at 630 MHz for highest excitation power is highlighted by circle.

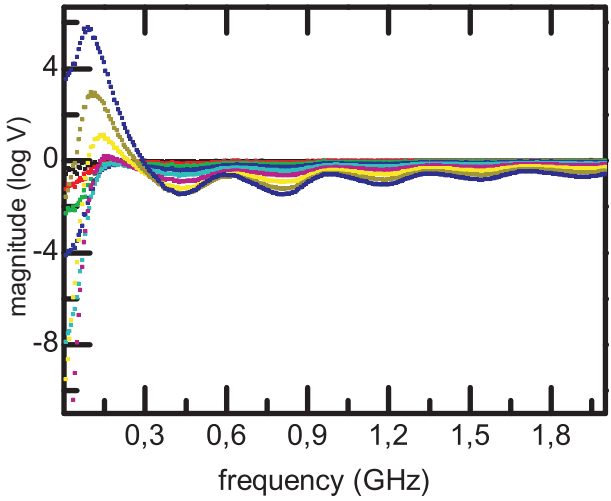

Figure 6.12: Detail of power dependence measurements. Magnitude of S11 in logarithmic scale over frequency, focussing on the frequency range form 10 MHz to 2 GHz.

In addition a signature at roughly 120 MHz can be observed. For high powers (>0 dBm) a peak evolves from the otherwise lowering ground. This is shown in detail in fig. 6.12. Towards the lower end of the available frequency range the spectra tend to drop steeply for increasing excitation powers. When the power exceeds 0 dBm this behavior changes drastically and a peak evolves within 12 dBm increase of the excitation power. At +12 dBm this peak is by far the highest over the whole frequency range. The position of the peak shifts form 120 MHz at 0 dBm towards 80 MHz at +12 dBm.

Mechanical oscillations

To discuss our findings with respect to mechanical oscillations of the nanomechanical bridge it is instructive to revisit the expected mechanical properties of the particular nanobridge in the measured CPW.

	GaAs	Co	Cr	Ag	Au
ρ (g/cm^3)	5.32	8.90	7.19	10.49	19.3
E (GPa)	83	209	279	83	79
t (nm)	up to 100	21	4.5	100	21

Table 6.1: Table with material parameters necessary to determine the eigenfrequency of the nanobridge. t is the thickness of the layer.

Thus we calculate the expected lowest eigenfrequency of the nanobridge. As presented in chap. 2.3 we follow the Euler-Bernoulli theory which yields the mechanical eigenfrequencies

$$2\pi f = \sqrt{\frac{EI}{\rho A}} q_n^2, \tag{6.3}$$

with the material parameters Young's modulus E and density ρ and the geometrical parameters cross-sectional area A and bending moment of inertia I. The eigenvector q_n is determined by the boundary conditions. For a doubly clamped beam the lowest eigenvector is

$$q_1 L = 4.73 \tag{6.4}$$

with the length L of the bridge.

We use averaged effective material parameters for the calculations. This is a valid assumption for oscillations perpendicular to the growth direction. Following the parallel axis theorem by Huygens and Steiner only the distance in the direction of movement of the center of mass of each layer to the neutral fibre of the bridge has to be taken into account for calculations of the bending moment of inertia.

The parameters of the materials used in the bridge are shown in Tab. 6.1 where t is the thickness of the layer. The GaAs layer has roughly a triangular shape and varies in thickness depending on each particular preparation process. Because we did not determine the actual dimensions of each nanobridge we calculate the eigenfrequency by assuming a rectangular shaped GaAs layer with a thickness of (a) 0 nm

and (b) 100 nm. This provides a decent range of the eigenfrequency of the nanobridge.

Assuming a rectangular cross-sectional area $A = wt$ with a moment of inertia of $I = \frac{w^3 t}{12}$ for oscillation parallel to the sample surface we obtain the lowest eigenfrequency to

$$f_0 = \sqrt{\frac{12E}{\rho}} \frac{w}{2\pi L^2} q_1. \tag{6.5}$$

We average the density and Young's modulus weighted by the layer thickness. With the length of the bridge $L = 2$ μm and the width $w = 120$ nm we get

$$f_0 = 240 \text{ MHz}, \quad t_{\text{GaAs}} = \quad 0 \text{ nm},$$
$$f_0 = 260 \text{ MHz}, \quad t_{\text{GaAs}} = 100 \text{ nm}.$$

For oscillations in out-of-plane direction we use the same averaged material parameters but the moment of inertia in the other direction $I = wt^3/12$ we get:

$$f_0 = 290 \text{ MHz}, \quad t_{\text{GaAs}} = \quad 0 \text{ nm}$$
$$f_0 = 530 \text{ MHz}, \quad t_{\text{GaAs}} = 100 \text{ nm}.$$

The calculated oscillation frequencies are in the range of 240 MHz up to 530 MHz which corresponds roughly with the measured resonance. From our measurements we can not distinguish between in-plane and out-of-plane oscillation.

Using the power dependent measurements it is possible to distinguish between FMR and mechanical resonances. While for the FMR only a small decrease of the peak height is expected with increasing excitation power, a mechanical resonance should exhibit the characteristic power dependent lineshape and center frequency described by the Duffing equation in sec. 2.3. At the frequency of the Co-FMR indeed no irregularity can be observed. Around 530 MHz we observe a shift of the maximum at 630 MHz in fig. 6.11(c). The curve with highest excitation power intersects the curve with the next lower excitation power. This is in contrast to the overall monotonic evolution of the power dependent frequency spectra.

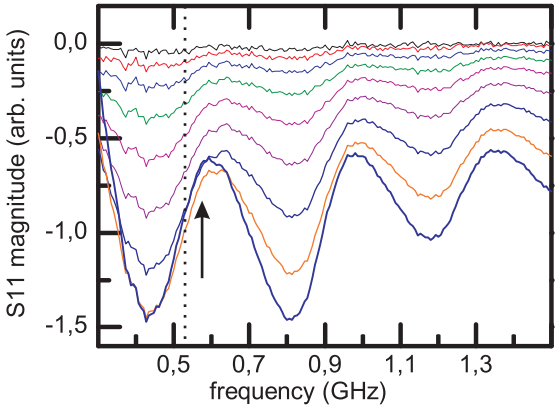

Figure 6.13: Detail of the power dependent evolution of the resonance at 530 MHz. Position of the resonance is marked by vertical dotted line.

We speculate that this shift is due to an evolving peak within the low frequency side of the maximum at 630 MHz. In the case of a highly excited mechanical oscillation we expect the resonance frequency to shift towards higher frequencies as described in chap. 2.3. Because of the difference method we used in the data presentation this would result in an evolving peak on the high frequency side of the resonance. In fig. 6.14 the difference method is qualitatively shown. The difference peak is on the high frequency side of the resonance peak.

At the position marked by an arrow in fig. 6.13 the curve with the highest excitation power intersects the curve with the next lower excitation power. This intersection does not origin from on the strong increase of the signal towards zero frequency discussed in fig. 6.12. This can be seen by comparing the minima of both curves around 430 MHz. At these minima the curve with the highest excitation power is still the lowest curve and the position of the minima has not changed significantly. In contrast, the position of the maximum on the right hand side of the vertical dotted line has shifted towards lower frequency. We attribute this to an evolving peak within the rising edge of the signal

for the highest excitation power.

The additional peak at 120 MHz shown in fig. 6.12 that evolves for excitation powers above 0 dBm does not match the calculated mechanical resonance frequency. The shift of the peak towards lower frequencies for increasing excitation powers is due to the slope in the background. While the background is lowering for increasing excitation powers the peak is superimposed on this trend. In the following discussion we focus on the peak at 530 MHz.

6.2.3 Discussion

In the discussion we focus on mechanical properties of the nanomechanical bridge. First, we revisit the measured data and match the expected FMR to them. The FMR of the plain Co layer can be clearly identified in fig. 6.7 and follows the expected behavior. The FMR frequency starts at 9 GHz and 0 T external perpendicular field and stays more or less constant up to 1.5 T. Afterwards it increases strongly with increasing external magnetic field.

During the preparation process of the nanobridge we confined this layer directly under the bridge. The dimensions of the confined nanobridge are width $w = 120$ nm, length $l = 2$ μm, and thickness $t \sim 150$ nm. Such a confined Co layer is expected to show a significantly different FMR behavior than a plain film [Gie05]. Qualitatively the frequency of confined nanowires should go up in frequency and still depend on the external magnetic field. Because the intensity of the FMR absorption peak depends on the amount of magnetic material in resonance we expect the confined Co layer on the bridge to exhibit a significantly lower FMR peak. The whole Co layer is 300 μm in length while the bridge is 2 μm in length. Thus we expected the signal to be in the order of factor 150 lower than the FMR of the plain film. For these reasons we do not expect to observe a separate FMR of the confined Co layer on the nanobridge.

We observed an additional resonance at 530 MHz. This resonance is not part of the FMR of the Co plain film. It is also not due to a FMR of the confined part of the Co layer on the nanobridge. We

can also exclude that the resonance at 530 MHz is due to the setup or the specific CPW design. Measurements on the same setup with comparable samples but without nanobridge (not shown in this work) do not exhibit a resonance in this frequency regime.

Therefore we speculate that the observed resonant absorption is due to an excitation of the nanomechanical bridge. As described in chap. 2.3 the microwave is able to couple to the mechanical motion of the nanomechanical bridge. In contrast to a FMR the frequency of a mechanical resonance is not expected to depend significantly on the external magnetic field.

We showed in chap. 2.3 that with increasing excitation power the absorption peak of a mechanical resonance is expected to become more saw-tooth like with a steeper slope on the high frequency side. In addition, the amplitude of the mechanical oscillation in resonance is expected to become higher with increasing power. To visualize the peak shift expected in the experiment due to the difference method in the data evaluation is shown in fig. 6.14. In the difference spectrum the peak is significantly shifted towards higher frequency with respect to the resonance peak at 530 MHz. The calculated lowest eigenfrequency of the bridge is in the same frequency regime as the resonance we measured.

The resonance frequency does not shift with increasing external magnetic field. We expect this from a mechanical oscillation. In the power dependent measurements in fig 6.11 an evolving peak at ~ 600 MHz can be seen for the highest excitation power. This is not exactly where the observed resonance peak is located but shift slightly to higher frequency. Because the resonance peak of a mechanical oscillation shifts slightly to higher frequency for increasing excitation power, we expect in the difference spectra an evolving peak on the high frequency side of the mechanical resonance. This is what we observe experimentally as displayed in fig. 6.13. Thus, the power dependent experimental data are consistent with a mechanical resonance at 530 MHz.

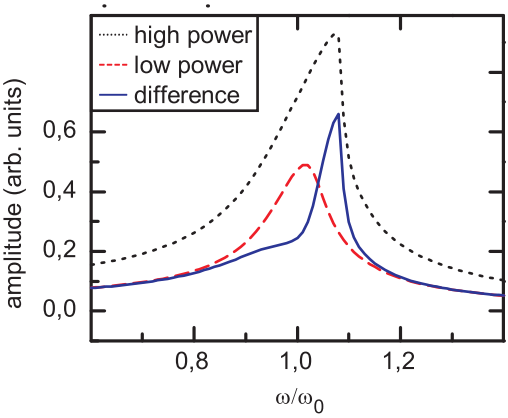

Figure 6.14: Two resonance curves of the Duffing oscillator with different excitation power. From the resonance curve of the high power excitation (dotted line) we subtracted the low power excitation curve (dashed line) to highlight the expected frequency shift in the difference resonance curve (solid line).

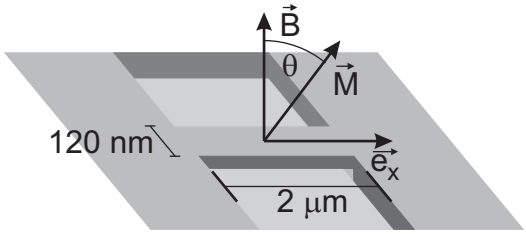

Figure 6.15: Schematic view of the nanomechanical bridge

Coupling mechanisms

The next step is to determine by which coupling mechanism the bridge is excited. We will revisit the coupling mechanisms presented in chap. 2.3.1 with respect to our experimental findings.

The magnetostrictive coupling mechanism depends strongly on the direction of the magnetization $\vec{M}$. We discuss the orientation of $\vec{M}$ as a function of the external magnetic field in the following. A schematic view of the directions with respect to the nanomechanical bridge can be seen in fig. 6.15. The magnetization is perpendicular to the sample as long as the external magnetic field is larger than the saturation magnetization field $B_{sat} \sim 1.6$ T. The magnetization starts to tilt into the in-plane direction if the external magnetic field is lower than B_{sat}. At an external magnetic field of $B \to 0$ the magnetization in completely in-plane.

To determine the direction of the magnetization we assume that the magnitude of the magnetization is in saturation independent of the direction. As a first step, we need to determine the demagnetization tensor $\hat{N}$. Here, we follow [Aha98] to calculate $\hat{N}$ for a rectangular element with the dimension of the Co layer on the nanobridge, which are width $w = 120$ nm, length $l = 2$ μm, and thickness $t = 21$ nm. Note, that the demagnetizing factor is also influenced by the surrounding ferromagnetic material. We neglect this influence for now. With the

demagnetization tensor

$$\hat{N} = \begin{pmatrix} 0.0099 & 0 & 0 \\ 0 & 0.1777 & 0 \\ 0 & 0 & 0.8124 \end{pmatrix} \tag{6.6}$$

we can calculate the part of the free energy

$$F = -MH_{ex}(\cos\theta) + \frac{1}{2}N_z M^2 \sin^2\theta \tag{6.7}$$

of the system that depends on the angle θ between the surface normal and the magnetization for decreasing external magnetic fields $H_{ex} = B/\mu_0$ starting at $B = B_{sat}$. Within this ansatz we assumed the in-plane component of the magnetization to always be in x direction. This is a valid assumption because of the shape anisotropy of the nanobridge. Measurements on similar Co plain films produced in our group exhibited a crystalline anisotropy constant in the order of $K_1 = 10^{+3}$ J/m^3 while the shape anisotropy has a value in the order of 10^5 J/m^3.

The out-of-plane component of the magnetization has a value such that its demagnetization field $H_{dm,z} = N_z M_z$ compensates the external magnetic field. The out-of-plane component of the internal field is therefore zero. We have to take into account that the actual magnetic field near the Co layer is influenced by the demagnetization field that depends on the magnetization of the Co layer. Because the Co layer is separated from the conducting layers only by a roughly 4 nm thick silicon dioxide layer we assume as an approximation that the demagnetization field acts within the conducting layer and reduces the actual magnetic field. Note, that the actual magnetic field in the conductor is reduced by the demagnetization field. At $B_{ex} = 0$ it is still zero.

Armed with this knowledge we can discuss different coupling mechanisms in the following. We focus on the expected dependence of the oscillation amplitude with respect to the external magnetic field for each mechanism. For further details on different excitation mechanisms for nanomechanical devices see [Eki05].

magnetomotive coupling

The bridge is deflected by the Lorentz force

$$F_L = q\vec{v} \times \vec{B}, \tag{6.8}$$

acting on the charge carrier with charge q and velocity $\vec{v}$ in an external magnetic field $\vec{B}$. While we do not exactly know the current I we do know the time dependence $I(t) = I_0 \cos \omega t$ which is given by the VNA incident microwave. For small deflections we can assume that I and B are always perpendicular. The exciting force is then

$$F_L = I_0 \cos(\omega t) Bl. \tag{6.9}$$

when a current I is passed through the bridge. Here, l is the length of the bridge. In particular the exciting force is zero at $B = 0$ T and should linearly increase in the experiment with increasing B. We do not observe such a dependence. Instead in fig. 6.9 the peak height goes down till it reaches zero at roughly 1.1 T. Although the field B is influenced by the demagnetization field of the Co layer at $B_{ex} = 0$ the actual field in the conductor is still zero. At $B_{ex} = 0$ the magnetization of the Co layer is completely in-plane and therefore the z component of the demagnetization field is also zero. Thus magnetomotive coupling can not explain the experimentally observed resonance at 530 MHz.

magnetostriction

The magnetostrictive coupling, in contrast to the magnetomotive coupling mechanism, does not depend directly on the external magnetic field but on the magnetization of the magnetic material. Only the magnetization in x direction would lead to a deflection of the bridge. In y direction the bridge is symmetrically elongated with respect to the principal axis of the bridge and in z direction only the thickness of the bridge changes in a sub-Å regime.

From determining the demagnetization field we know the magnetization vector for a given external magnetic field. While $B > B_{sat}$ the magnetization is 90° out-of-plane. If the external field decreases the magnetization tilts towards the in-plane direction along the bridge. At

$B = 0$ is magnetization is completely in-plane along the principal axis of the bridge.

At high external magnetic fields the magnetization of the Co layer is out-of-plane. In this case the precession due to an exciting microwave results in a small periodic component along the bridge axis. If the external magnetic field is not strong enough to saturate the magnetization in z direction, the actual magnetization is tilted towards the in-plane direction.

Our measurements are performed by first ramping the external magnetic field to 2.5 T and take a reference measurement. Thus we assume to always have saturated the magnetization. If the magnetization vector points in-plane but is still at its saturation value a precession due to an exciting microwave would lead to no change in the magnetization component along the bridge axis at all.

At $B = 0$ we expect no excitation due to magnetostriction. A precession of the magnetization due to a gigahertz excitation with frequency ω would not lead to a change in the x component of the magnetization with frequency ω. Instead both other components do oscillate with this frequency. The opening angle of the magnetization is extremely small in the non resonant case. Thus we expect the magnetostrictive coupling to lead to zero oscillation amplitude at low external magnetic fields, especially at $B_{ex} = 0$. Hence, magnetostrictive coupling cannot explain the experimentally observed resonance at 530 MHz.

Because both mechanisms are not able to explain the experimental observed evolution with the external magnetic field of the resonance at 530 MHz, we discuss in the following additional excitation mechanisms of nanomechanical devices. The are

- electrostatic and dielectric force,
- external mechanical vibrations,
- and damping of non resonant ferromagnetic precession.

This list is not necessarily complete but a decent overview over possible coupling mechanisms.

electrostatic and dielectric force

For our experimental geometry the electrostatic coupling can be assumed to be negligible because of the symmetric design of the CPW and the bridge leading to no net forces on the bridge. However, if one of the ground lines has not been connected sufficiently, this would lead to a net electrostatic force on the bridge.

The electro static force is given by

$$F = \frac{dW}{d(\Delta y)}, \tag{6.10}$$

with the energy stored in the electric field W and the deflection of the bridge in y-direction Δy. In the case of a plate capacitor the energy is $W = \frac{1}{2}CU^2$ with $C = \epsilon_0 A/d$. The incident microwave results in a voltage $U = U_0 \cos \omega t$ between the bridge and the ground line. Because the force is always attractive it exhibits a time dependence of $F(t) \propto \cos 2\omega t$. Additionally, there is no explicit dependence on the external magnetic field. Therefore we would expect an oscillation amplitude that does not depend on the external magnetic field.

Recent experiments showed a novel technique to excite nanomechanical resonators on the basis of polarized dielectrics in non uniform electric fields [Unt09]. This should also be negligible because in our case the bridge carries a conductor. Therefore we expect the electro static force to be significantly stronger than the dielectric force.

external mechanical excitation

As another possibility, the excitation of the nanobridge could be independent of the incident microwave. Mechanical vibrations of the setup due to liquid helium flow or the vibration of external pumps could excite mechanical oscillations. All these mechanical oscillations have significantly lower frequencies in contrast to the measured resonance. Therefore no harmonic excitation of the bridge by external vibrations is expected.

For transient excitations to excite 500 MHz oscillations extremely short rise time would be necessary. Additionally we expect the Q fac-

tor of the nanobridge to be low < 100. This can be seen from our measurements where the center frequency f_0 and the full-width at half maximum Δf are of the same order of magnitude. Thus $Q = f_0/\Delta f$ is small. A transient excitation capable of driving the nanomechanical bridge would have to be extremely periodic over the whole measurement time (several hours) and also at different measurements (several days between each). Therefore we do not expect external mechanical excitations to be the origin of the measured resonance.

damping of non resonant ferromagnetic precession

During the excitation of the magnetization due to the microwave in the non resonant case, parts of the excitation energy is not re-emitted into the conductor but transferred to phonons due to a corresponding relaxation process. In a straight forward picture these phonons have the same frequency as the incident microwave. The wavelength of such phonon would be

$$\lambda = \frac{2\pi v_{sound}}{\omega} = 19\ \mu\text{m}. \tag{6.11}$$

The lowest eigenfrequency of the bridge corresponds to a wavelength of

$$\lambda = 2L = 4\ \mu\text{m} \tag{6.12}$$

with the length of the bridge L. Both lengthes are in the same order of magnitude thus a excitation via this mechanism seems reasonable. On the other hand this mechanism does not depend on the external magnetic field. Thus the measured B field dependence of the oscillation amplitude of the mechanical oscillation can not be explained.

6.3 Conclusion

Based on our measurements we conclude that the preparation process of nanomechanical bridges does not influence the GHz spectroscopy measurements in the frequency domain. Although the overall microwave conductance properties of the CPWs are changed slightly by the preparation process no significant influence is observed.

From the VNA measurements we conclude that we observe an additional resonance signature at 530 MHz that does not show the expected behavior of a FMR. Instead some of the characteristics can be explained by a mechanical oscillation of the nanobridge. The frequency is in the same range as the calculated lowest eigenfrequency of the nanobridge.

The power dependent measurements indicate a shift of the resonance frequency for increased excitation power. We attribute this to the expected behavior of mechanical oscillations following the model of a Duffing oscillator. To determine the coupling mechanism by which the nanobridge is excited via the incident microwave we compared the measured B-field dependence of the resonance absorption with the expected behavior for several different mechanisms. None of these are able to explain the experimental findings. Especially we were able to exclude the most commonly used mechanisms to excite mechanical oscillations of nanoscopic devices. The mechanism that drives the nanomechanical bridge into resonance remains unclear.

Chapter 7

Outlook

In this thesis a new setup for optical detection of sub-Å deflection detection was designed with a focus on a piezo based nano positioning system. We presented magnetization measurements on AlAs quantum wells under arbitrary angles and different temperatures. In a second part we presented measurements to determine the mechanical and magnetic properties of nanomechanical bridges. This included GHz spectroscopy with TDR and VNA devices at 4 K and room temperature.

In the following we summarize the results for each part of the work and give an outlook to further experiments.

Setup for optical cantilever readout

Magnetization measurements on AlAs require enhanced sensitivity thus the optical setup designed in the course of this work is necessary to gain in depth information on the energy structure of AlAs quantum wells. Especially due to the requirements on sample positioning with respect to the glassfibre additional affords has to be made to determine the exact position and movement of the sample. This is even more important for magnetization measurements on further reduced samples sizes.

In the course of this work we were able to gain fundamental understanding of the limitations of interferometric scanning, with respect to a position detection of the samples with respect to the glass fiber. Simulation revealed that especially the gold circuits provides problems if the scanning is done in the constant distance modus. Thus it is necessary to either quit using Au circuits and replacing them with a material that has more or less the same reflectivity as the GaAs surface, or quit using the constant distance mode. Because in the end our self made positioning system did not worked as intended and taking recent developments in the nanopositioning area into account commercially available modular piezo walker with position detection setups are a serious alternative to our self made piezo walkers.

Within the scope of the ^{3}He cryostat used in our group it is a challenging task to incorporate a rotatable sample stage in addition to the nanopositioning system. Thus we distinguish between additional experiments to be done with a optical setup with improved sensitivity and experiments that require the possibility to vary the angle α between the external magnetic field and the sample surface to values between $0°$ and $90°$. These are presented in the next section.

AlAs quantum wells

The angular dependence of the measurements on AlAs quantum wells presented in chap. 5.1 indicate a strongly interacting electron system.

We observed a change of the nature of the energy gap at filling factor $\nu = 1$ from a spin gap to a valley gap. This spin gap exhibits characteristics of skyrmion like behavior with a skyrmion size of ~ 5. In contrast we did not observe the expected coincidence points, which we attribute to an anticrossing of the relevant energy levels due to strong electron-electron interactions.

The temperature dependent measurements indicate strongly enhanced energy gaps and unexpected temperature dependence. While the exact level sequence is still unclear, at least on of the energy gaps is expected to depend significantly stronger on the temperature. A speculative attempt to explain our experimental findings is to assume

a strong repulsion between the energy levels. In this case they would from an almost equidistant energy level ladder.

Additional experiments should especially include temperature dependent measurements at angle below $\alpha = 30°$ where filling factor one is measurable. Within our speculative explaining attempt we expect filling factor one to show a significantly different temperature dependence than the other. In this course it would also be interesting to compare the temperature dependence of the filling factors before and after the energy level crossing. Additionally greater insight would be able if the measurements are repeated with improved sensitivity especially with a focus on filling factors ≥ 5.

Nanomechanical bridges

Our measurements on nanomechanical bridges indicate that the preparation process does not interfere with GHz spectroscopy measurements. Our bridge exhibited an ultra high resonance frequency in the regime of 0.5 GHz that could be measured using broadband VNA spectroscopy. In our discussion we focussed on the mechanism by which the bridge is excited. We were able to exclude all mechanisms commonly used to excite nanomechanical devices by comparing the B field dependence of the resonance amplitude with the expectations.

Additional investigations should focus on the fundamental interactions between ferromagnetic excitations and mechanical motion. Therefore we recommend especially to design devices where the FMR and the mechanical resonances are at the same frequency. To achieve this more afford has to be made to lower the FMR frequency at least under certain external fields. Because our data indicate an unusual mechanism is the origin of the oscillation of the nanobridge this should be investigated in more detail.

To improve GHz spectroscopy measurements on nanomechanical devices we recommend that from power dependent measurements not only the spectrum with the lowest excitation power is subtracted but to take reference measurements at a different magnetic field (e.g. 2.5 T) for each excitation power separately. Thereby the evolution of the

actual resonance peaks can be extracted.

Beside the possibility to change the geometrical dimensions of the bridge to verify the expected dependence of the frequency, we recommend to continue GHz spectroscopy measurements with high excitation powers but to vary the detection frequency while keeping the excitation frequency constant. Therewith it should be possible to gain a better understanding of the interactions between the incident microwave and the mechanical oscillations.

Another interesting goal is to detect the mechanical motions with the optical setup presented in this work while the bridge is excited by magneto-mechanical interactions. This would provide the unique ability to detect the motion of the bridge independently of the excitation mechanism.

Overall we conclude that in the field of magneto mechanical interactions and transducers still a huge amount of research has to be done. The field provides great possibilities in the fundamental physics as well as in possible applications. On the one hand the physics of the device itself but on the other hand detectors or novel measurement techniques in the field of magneto-mechanical nanotransducer should be investigated further.

Bibliography

[Ada85] S. Adachi. *Gaas, alas, and $al_x ga_{1-x} as$ material parameters for use in research and device applications.* J. Appl. Phys. **58**, R1 (1985).

[Aha98] Amikam Aharoni. *Demagnetizating factors for rectangular ferromagnetic prisms.* JAP **83**, 3432 (1998).

[All98] W. Allers. *Tieftemperatur-Rasterkraftmikrosopie im Ultrahoch-Vakuum auf Van-der-Waals-Oberflächen.* Dissertation, Universität Hamburg, 1998.

[And74] T. Ando and Y. Uemura. *Theory of oscillatory g-factor in an MOS inversion layer under strong magnetic fields.* J. Phys. Soc. Jpn. **37**, 1044 (1974).

[And82] T. Ando, A. B. Fowler and F. Stern. *Electronic properties of two-dimensional systems.* Rev. Mod. Phys. **54**, 437 (1982).

[Bog34] N. Bogoliubov. *The application of methods of non-linear mechanics to the theory of stationary oscillations*, Vol. 8. Publications of the Ukranian Academy of science, Kiev, 1934.

[Bor08] M. Borowski. *Entwicklung und Aufbau eines faseroptischen Cantilever-Magnetometers.* Dissertation, Technische Universität München, 2008.

[Bra07] Francesco Braghin, Ferruccio Resta, Elisabetta Leoa and Guido Spinola. *Nonlinear dynamics of vibrating mems.* Sensors and Actuators A **134**, 98–108 (2007).

[Byc84] Y. A. Bychkov and E. I. Rashba. *Oscillatory effects and the magnetic susceptibility of carriers in inversion layers.* J. Phys. C **17**, 6039 (1984).

[Chi07] K. K. Chin. *Interference of fiber-coupled gaussian beam multiply reflected between two planar interfaces.* Photonics Technology Letters **IEEE 19**, 1643–1645 (2007).

[Chi09] Soshin Chikazumi. *Phyisc of Ferromagnetism.* Oxford Science Publications, 2009.

[Cou04] G. Counil, J.-V. Kim, T. Devolder, C. Chappert, K. Shigeto and Y. Otani. *Spin wave contributions to the high-frequency magnetic response of thin films obtained with inductive methods.* Journal of Applied Physics **95**, 5646–5652 (2004).

[Das07] S. Dasgupta, C. Knaak, J. Moser, M. Bichler, S. F. Roth, A. Fontcuberta i Morral, G. Abstreiter and M. Grayson. *Donor binding energy and thermally activated persistent photoconductivity in high mobility (001) alas quantum wells.* Appl. Phys. Lett. **91**, 142120 (2007).

[Das08a] S. Dasgupta. *Shivaji Thesis.* Dissertation, Walter Schottky Institut, Technische Universität München, 2008.

[Das08b] S. Dasgupta, S. Birner, C. Knaak, M. Bichler, A. Fontcuberta i Morral, G. Abstreiter and M. Grayson. *Single-valley high-mobility (110) alas quantum wells with anisotropic mass.* Appl. Phys. Lett. **93**, 132102 (2008).

[Duf18] G. Duffing. *Erzwungene Schwingungen bei Veränderlicher Eigenfrequenz.* F. Vieweg u. Sohn, Braunschweig, 1918.

[Dür09] Georg Dürr. *Spin Dynamics in Permalloy Antidot Lattices: from Standing to Propagating Spin Waves.* Diplomarbeit, Technische Universität München, 2009.

[Eis85a] J. P. Eisenstein. *High-precision torsional magnetometer: Application to two-dimensional electron systems.* Appl. Phys. Lett. **46**, 695 (1985).

[Eis85b] J. P. Eisenstein, H. L. Stormer, V. Narayanamurti, A. Y. Cho, A. C. Gossard and C. W. Tu. *Density of states and de Haas-van Alphen effect in two-dimensional electron systems.* Phys. Rev. Lett. **55**, 875 (1985).

[Eki05] K. L. Ekinci and M. L. Roukes. *Nanoelectromechanical systems.* Review of Scientific Instruments **76**, 061101 (2005).

[Eng82] T. Englert, D. C. Tsui, A. C. Gossard and C. Uihlein. *g-factor enhancement in the 2D electron gas in GaAs/AlGaAs heterojunctions.* Surf. Sci. **113**, 295 (1982).

[Flü56] S. Flügge. *Handbuch der Physik*, Vol. 24. Springer, 1956.

[Gie05] Fabian Giesen. *Magnetization Dynamics of Nanostructured Ferromagnetic Rings and Rectangular Elements.* Dissertation, Universität Hamburg, 2005.

[Gil55] T. L. Gilbert. *A lagrangian formulation of the gyromagnetic equation of the magnetization field.* Phys. Rev. **100**, 1243 (1955).

[Gok08] T. Gokmen, Medini Padmanabhan, O. Gunawan, Y. P. Shkolnikov, K. Vakili, E. P. De Poortere and M. Shayegan. *Parallel magnetic-field tuning of valley splitting in alas two-dimensional electrons.* Phys. Rev. B **78**, 233306 (2008).

[Har99] J. G. E. Harris, F. Matsukura, H. Ohno, K. D. Maranowski and A. C. Gossard. *Integrated micromechanical cantilever magnetometry of $Ga_{1-x}Mn_xAs$.* Appl. Phys. Lett. **75**, 1140 (1999).

[Har00] J. G. E. Harris, D. D. Awschalom, K. D. Maranowski and A. C. Gossard. *Magnetization and dissipation measurement in the quantum hall regime using an integrated micromechanical magnetometer.* J. Appl. Phys. **87**, 5102 (2000).

[Har01] J. G. E. Harris, R. Knobel, K. D. Maranowski, A. C. Gossard, N. Samarth and D. D. Awschalom. *Magnetization measurements of magnetic two-dimensional electron gases.* Phys. Rev. Lett. **86**, 4644 (2001).

[Hol49] J. Holden. *Multiple-beam interferometry: Intensity distribution in the reflected system.* Proc. Phys. Soc. **62** (1949).

[Hol76] P. Holmes and D.A. Rand. *The bifurcations of duffing's equation: An application of catastrophe theory.* Journal of Soudn and Vibration **44**, 237–253 (1976).

[Höp01] Th. Höpfl, D. Sander, H. Höche and J. Kirschner. *Ultrahigh vacuum cantilever magnetometry with standard size single crystal substrates.* Rev. Sci. Instrum. **72**, 1495 (2001).

[Hua05] X. M. H. Huang, X. L. Feng, C. A. Zorman, M. Mehregany, and M. L. Roukes. *Vhf, uhf and microwave frequency nanomechanical resonators.* New Journal of Physics **7**, 247 (2005).

[Hua08] X. Huang. *De Haas-van Alphen-Effekt eines zweidimensionalen Elektronensystems mit Valley-Pseudospin.* Dissertation, Technische Universität München, 2008.

[Hub09] R. Huber. *Interaction of surface acoustic waves with magnetization dynamics.* Diplomarbeit, Tech. Univ. Muenich, 2009.

[Ihm92] G. Ihm, M. L. Falk, S. K. Noh, J. I. Lee and S. J. Lee. *Oscillating magnetization of quantum wells and wires in tilted magnetic fields.* Phys. Rev. B **46**, 15530 (1992).

[Jan69] J. F. Janak. *g-factor of the two-dimensional interacting electron gas.* Phys. Rev. **178**, 1416 (1969).

[Kac09] N. Kacem, S. Hentz, D. Pinto, B. Reig and V. Nguyen. *Nonlinear dynamics of nanomechanical beam resonators: improving the performance of nems-based sensors.* Nanotechnology **20**, 275501 (2009).

[Kit48] Ch. Kittel. *On the theory of ferromagnetic resonance absorption.* Phys. Rev. **73**, 155 (1948).

[Lay93] T. S. Lay, J. J. Heremans, Y. W. Suen, M. B. Santos, K. Hirakawa, A. Zrenner, and M. Shayegan. *High-quality two-dimensional electron system confined in an alas quantum well.* Applied Physics Letters **62**, 3120–3122 (1993).

[Lyd88] J. W. Lyding, S. Skala, J. S. Hubacek, R. Brockenbrough, and G. Gammie. *Variable-temperature scanning tunneling microscope*. Rev. Sci. Instrum. **59**, 1897 (1988).

[Maa84] J. C. Maan. In: G. Bauer, F. Kuchar and H. Heinrich, Hrsg., *Two Dimensional Systems, Heterostructures, and Superlattices*, S. 183. Springer-Verlag, Berlin, 1984.

[Mac86] A. H. MacDonald, H. C. A. Oji and K. L. Liu. *Thermodynamic properties of an interacting two-dimensional electron gas in a strong magnetic field*. Phys. Rev. B **34**, 2681 (1986).

[Man95] A. Manolescu and R. R. Gerhardts. *Exchange-enhanced spin splitting in a two-dimensional electron system with lateral modulation*. Phys. Rev. B **51**, 1703 (1995).

[Mer87] R. Merlin. *Subband-Landau-level coupling in tilted magnetic fields: exact results for parabolic wells*. Solid State Commun. **64**, 99 (1987).

[Mey05] C. Meyer, O. Sqalli, H. Lorenz and K. Karrai. *Slip-stick step-scanner for scanning probe microscopy*. Review of Scientific Instruments **76**, 063706 (2005).

[Mul91] P. J. Mulhern, T. Hubbard, C.S. Arnold, B.L. Blackford, and M. H. Jericho. *A scanning force microscope with fiber-optic-interferometer displacement sensor*. Review of Scientific Instruments **62**, 1280–1284 (1991).

[Nau98] M. J. Naughton, J. P. Ulmet, A. Narjis, S. Askenazy, M. V. Chaparala and R. Richter. *Demonstration of cantilever magnetometry in pulsed magnetic fields*. Physica B **246-247**, 125 (1998).

[Neu08] Sebastian Neusser. *Spin-Dynamics in Antidot Lattices*. Diplomarbeit, Technische Universität München, 2008.

[nex] nextnano. *The simulator software nextnano*^{3} *can be obtained from http://www.wsi.tum.de/nextnano3*.

[Nic88] R. J. Nicholas, R. J. Haug, K. v. Klitzing and G. Weimann. *Exchange enhancement of the spin splitting in a GaAs-$Ga_xAl_{1-x}As$ heterojunction.* Phys. Rev. B **37**, 1294 (1988).

[Pap99] S. J. Papadakis, E. P. De Poortere and M. Shayegan. *Anomalous spin splitting of two-dimensional electrons in an alas quantum well.* Phys. Rev. B **59**, R12743 (1999).

[Pic07] Dr. Lutz Pickelmann. *Piezomechanische Stapel- und Ringaktoren: Produktpalette und technische Daten.* Piezomechanik GmbH, 2007.

[Poh87] D. W. Pohl. *Dynamic piezoelectric translation devices.* Rev. Sci. Instrum. **58**, 54 (1987).

[Pot96] A. Potts, R. Shepherd, W. G. Herrenden-Harker, M. Elliott, C. L. Jones, A. Usher, G. A. Jones, D. A. Ritchie, E. H. Linfield and M. Grimshaw. *Magnetization studies of Landau level broadening in two-dimensional electron systems.* J. Phys. C **8**, 5189 (1996).

[Ruh08] N. Ruhe. *Magnetisierungsmessung zur Untersuchung von Quantisierungs-Effekten in zweidimensionalen Elektronensystemen.* Dissertation, Universität Hamburg, 2008.

[Sch95] A. Schmeller, J. P. Eisenstein, L. N. Pfeiffer and K. W. West. *Evidence for skyrmions and single spin flips in the integer quantized Hall effect.* Phys. Rev. Lett. **75**, 4290 (1995).

[Sch00] M. P. Schwarz, D. Grundler, I. Meinel, Ch. Heyn and D. Heitmann. *Micromechanical cantilever-magnetometer with an integrated two-dimensional electron system.* Appl. Phys. Lett. **76**, 3564 (2000).

[Sch02a] M. R. Schaapman, P. C. M. Christianen, J. C. Maan, D. Reuter and A. D. Wieck. *A multipurpose torsional magnetometer with optical detection.* Appl. Phys. Lett. **81**, 1041 (2002).

[Sch02b] M. P. Schwarz, M. A. Wilde, S. Groth, D. Grundler, Ch. Heyn and D. Heitmann. *Sawtooth-like de Haas-van Alphen*

oscillations of a two-dimensional electron system. Phys. Rev. B **65**, 245315 (2002).

[Sha06] M. Shayegan, E. P. De Poortere, O. Gunawan, Y. P. Shkolnikov, E. Tutuc and K. Vakili. Phys. Stat. Solidii (b) **243**, 3629 (2006).

[Shk02] Y. P. Shkolnikov, E. P. De Poortere, E. Tutuc and M. Shayegan. *Valley splitting of alas two-dimensional electrons in a perpendicular magnetic field*. Phys. Rev. Lett. (**89**, 2268052002).

[Shk05] Y. P. Shkolnikov, S. Misra, N. C. Bishop, E. P. De Poortere and M. Shayegan. *Observation of quantum hall "valley skyrmions"*. Phys. Rev. Lett. **95**, 066809 (2005).

[Sho84] D. Shoenberg. *Magnetization of a two-dimensional electron gas*. Journal of Low Temperatur Physics **56**, 417 (1984).

[Spr07] Jan-Ivo Springborn. *Magnetometrie an Halbleiter-Nanostrukturen mit wenigen Elektronen*. Dissertation, Unversität Hamburg, 2007.

[Sti01] B. C. Stipe, H. J. Mamin, C. S. Yannoni, T. D. Stowe, T. W. Kenny and D. Rugar. *Electron spin relaxation near a micron-size ferromagnet*. Phys. Rev. Lett. **87**, 277602 (2001).

[Tem88] I. M. Templeton. *A high-sensitivity torsional magnetometer for two-dimensional electron systems*. J. Appl. Phys. **64**, 3570 (1988).

[Tim74] S. Timoshenko, D. Young and J. W. Weaver. *Vibration Problems in Engineering*. Wiley, New York, 1974.

[Tsu82] D. C. Tsui, H. L. Stormer and A. C. Gossard. *Two-dimensional magnetotransport in the extreme quantum limit*. Phys. Rev. Lett. **48**, 1559 (1982).

[Unt09] Quirin P. Unterreitheimer, Eva M. Weig and Jörg P. Kotthaus. *Universal transduction scheme for nanomechanical systems base on dielectric force*. nature **458** (2009).

[Ush09] A. Usher and M. Elliott. *Magnetometry of low-dimensional electron and hole systems.* J. Phys.: Condens. Matter **21**, 103202 (2009).

[Vak04] K. Vakili, Y. P. Shkolnikov, E. Tutuc, E. P. De Poortere and M. Shayegan. *Spin susceptibility of two-dimensional electrons in narrow alas quantum wells.* Phys. Rev. Lett. (**92**, 2264012004).

[Vau89] J. M. Vaughan. *The Fabry-Perot Interferometer.* Adam Hilger, 1989.

[vdP34] B. van der Pol. *The nonlinear theory of electric oscillations.* Proceedings of the Institute of Radio Engineers **22**, 1051–1086 (1934).

[vK80] K. v. Klitzing, G. Dorda and M. Pepper. *New method for high-accuracy determination of the fine-structure constant based on quantized Hall resistance.* Phys. Rev. Lett. **45**, 494 (1980).

[vK89] H. W. van Kesteren, E. C. Cosman, P. Dawson, K. J. Moore and C. T. Foxon. *Order of the x conduction-band valleys in type-ii gaas/alas quantum wells.* PRB **39**, 13426 (1989).

[vK90] H. W. van Kesteren, E. C. Cosman, W. A. J. A. van der Poel and C. T. Foxon. *Fine structure of excitons in type-ii gaas/alas quantum wells.* Phys. Rev. B (**41**, 52831990).

[Web25] W. L. Webster. *Magneto-striction in iron crystals.* Proc. Roy. Soc. A (London) **A109**, 570–584 (1925).

[Wie97] S. A. J. Wiegers, M. Specht, L. P. Lévy, M. Y. Simmons, D. A. Ritchie, A. Cavanna, B. Etienne, G. Martinez and P. Wyder. *Magnetization and energy gaps of a high-mobility 2D electron gas in the quantum limit.* Phys. Rev. Lett. **79**, 3238 (1997).

[Wil04] M. A. Wilde, J. I.Springborn, Ch. Heyn, D. Heitmann and D. Grundler. *Magnetization of gaas quantum wires with quasi one-dimensional electron systems.* Physica E **22**, 729–732 (2004).

[Wil05] M. A. Wilde, M. Rhode, Ch. Heyn, D. Heitmann, D. Grundler, U. Zeitler, F. Schaffler and R. J. Haug. *Direct measurements of the spin and valley splittings in the magnetization of a si/sige quantum well in tilted magnetic fields.* Phys. Rev. B **72**, 165429 (2005).

[Wil06] M. A. Wilde, M. P. Schwarz, Ch. Heyn, D. Heitmann, D. Grundler, D. Reuter and A. D. Wieck. *Experimental evidence of the ideal de haasŰvan alphen effect in a two-dimensional system.* Phys. Rev. B **73**, 125325 (2006).

[Wil09] M. A. Wilde, D. Reuter, C. Heyn, A. D. Wieck and D. Grundler. *Inversion-asymmetry-induced spin splitting observed in the quantum oscillatory magnetization of a two-dimensional electron system.* PRB **79**, 125330 (2009).

[Win09] T. Windisch, X. Huang, S. Dasgupta, B. Rupprecht, Ch. Heyn, M. Bichler, A. Fontcuberta i Morral, M. Grayson, G. Abstreiter, M. A. Wilde and D. Grundler. *De haas-van alphen effect and energy gaps of a correlated two-dimensional electron system in an alas two-valley pseudospin system.* PRB **80**, 205306 (2009).

[XLF07] Peidong Yang X. L. Feng, Rongrui He and M. L. Roukes. *Very high frequency silicon nanowire.* Nano Letters **7**, 1953–1959 (2007).

[Zha97] C. Zhang and Y. Takahashi. *Magnetotransport of a two-dimensional electronic system in a tilted magnetic field.* Semicond. Sci. Technol. **12**, 835 (1997).

[Zhu03] M. Zhu, A. Usher, A. J. Matthews, A. Potts, M. Elliott, W. G. Herrenden-Harker, D. A. Ritchie and M. Y. Simmons. *Magnetization measurements of high-mobility two-dimensional electron gases.* Phys. Rev. B **67**, 155329 (2003).

Publications

- T. Windisch, X. Huang, S. Dasgupta, B. Rupprecht, Ch. Heyn, M. Bichler, A. Fontcuberta i Morral, M. Grayson, G. Abstreiter, M. A. Wilde, and D. Grundler: *De Haas-van Alphen effect and energy gaps of a correlated two-dimensional electron system in an AlAs two-valley pseudospin system*, Phys. Rev. B **80**, 205306 (2009)
- B. Rupprecht, W. Krenner, U. Wurstbauer, Ch. Heyn, T. Windisch, M. A. Wilde, W. Wegscheider, and D. Grundler: *Magnetism in a Mn modulation-doped InAs/InGaAs heterostructure with a two-dimensional hole system*, J. Appl. Phys. **107**, 093711 (2010)

Acknowledgements

I would like to thank all the people who helped to make this work a success. Special thanks to

- Prof. Dr. D. Grundler for the opportunity to work in his group here in Munich,
- Prof. A. Holleitner for being the referee for this thesis,
- Dr. Marc A. Wilde for scientific guidance,
- Nanosystems Initiative Munich (NIM) especially area A and D,
- P. Weiser for keeping an eye on the FIB,
- my collaborators and colleagues at E10: B. Rupprecht, A. Wittmann, B. Botters, S. Neusser, G. Dürr, M. Brasse, R. Huber, F. Brandl, K. Thurner, M. Borowski, W. Krenner, X. Huang, P. Klemm,
- S. Dasgupta and the whole MBE team at the WSI as well as C. Heyn and the whole MBE team in Hamburg for various samples,
- the technical staff at E10: H. Hetzl, J. Seitz, T. Rapp, S. Lichtenauer, T. Neukel,
- my family: Claudia, Ralf, Malte, Tasja, Gisela, Ariane, Klaus and Sybille,
- and to everyone I forgot who had impact on my work.